GEOWISSENSCHAFTLICHE MITTEILUNGEN

No. 70, 2004

Amalthea's Gravity Field and its Impact on a Spacecraft Trajectory

by
Gudrun Weinwurm

Publication of the Institute for Geodesy and Geophysics

ISSN 1811-8380

Schriftenreihe der Studienrichtung VERMESSUNG UND GEOINFORMATION
TECHNISCHE UNIVERSITÄT WIEN

2004
Published by the Institutes
of the Course on ‘Geodesy and Geoinformation’
Vienna University of Technology
Gusshausstrasse 27-29
A-1040 Vienna

Responsible for this issue: ao. Prof. Dr. Robert Weber
Printed by: Grafisches Zentrum HTU GmbH
Expenses for printing and binding: Department of Advanced Geodesy

Diese Arbeit wurde an der Fakultät für Mathematik und Geoinformation der Technischen Universität Wien zur Erlangung des akademischen Grades eines Doktors der technischen Wissenschaften eingereicht.

This work has been carried out at the Faculty of Mathematics and Geo-Information, Vienna University of Technology, in order to obtain the academic degree Doctor of Technical Sciences. It was performed in collaboration with the Radio Science Team at the NASA Jet Propulsion Laboratory, California Institute of Technology, under the supervision of Dr. John D. Anderson.

Examiners:

Prof. Dr. Robert Weber
Institute of Geodesy and Geophysics, Vienna University of Technology
A-1040 Vienna, Gusshausstrasse 27-29, Austria

Prof. Dr. Pascale Ehrenfreund
Leiden Observatory
NL-2300 RA Leiden, PO Box 9513, The Netherlands

Day of oral exam: 6 July 2004

Edition: 70 copies

ISSN 1811-8380

“The universe cannot be read until we have learnt the language and become familiar with the characters in which it is written. It is written in mathematical language, and the letters are triangles, circles and other geometrical figures, which means it is humanly impossible to comprehend a single word.” Galileo Galilei

Jupiter and its four Galilean satellites, recorded with a CCD-camera in the scope of G. Weinwurm’s master thesis (July 1997).

Abstract

Before its final plunge into the planet Jupiter in September 2003, the NASA spacecraft GALILEO made a last 'visit' to one of Jupiter's smaller inner moons – Amalthea. This concluding flyby of the spacecraft's successful mission occurred on November 5, 2002.

Radio tracking of a spacecraft during planetary body encounters in general allows for the characterisation of planetary atmospheres, surfaces, mass, gravity fields, etc. In the case of GALILEO the Amalthea flyby was dedicated to the latter two.

In order to obtain Amalthea's gravity field and its moments of gravitation, based on various interior models of the moon, the method for numerically integrating infinitesimal volume elements has been applied. Latter have been derived from the scale factors of a three-axial ellipsoid (elliptic coordinates) because of Amalthea's non-spherical shape. The computer programme GRASP (Gravity Field of a Planetary Body and its Influence on a Spacecraft Trajectory) has been developed within the frame of the present thesis to facilitate the required calculations. GRASP applies the second method of Neumann to obtain the harmonic coefficients of Amalthea's gravity field which have been derived up to degree and order six, for both homogeneous and reasonable heterogeneous cases. The normalised quadrupole moments of gravitation lie in the order of 0.038 for J_2 and -0.053 for J_{22}.

Based on GALILEO's state vector at closest approach to Amalthea (provided by the Jet Propulsion Laboratory, NASA) and the moon's various gravity field models, a number of spacecraft flybys have been calculated through the numerical integration method of Runge-Kutta. Assessments of the diverse trajectories yield velocity perturbations which have been compared to existing Doppler data from the Amalthea flyby. For the reason of a failure caused by an improper carrier frequency only low accuracy one-way Doppler data from GALILEO tracking was available. It was thus merely possible to obtain Amalthea's mass and mean density (~860 kg/m³), whereas the harmonic coefficients of the moon's gravity field are buried deep in the data noise.

Nevertheless, predictions for future flybys in the scope of the Jovian system exploration can be made. In order to get more valuable information about the gravity field of this tiny rocky moon (mean radius 83.45 km), a much closer flyby than that of GALILEO should be anticipated, preferable in the order of 80 km flyby altitude. Another possibility and option to derive interior structure data of Amalthea would be a space mission dedicated to in-situ seismic and geological measurements.

Zusammenfassung

Die Raumsonde GALILEO der amerikanischen Weltraumorganisation NASA vollbrachte nach fast 13 Jahren erfolgreicher Erkundung des Jupitersystems am 5. November 2002 ihre letzte wissenschaftliche Mission: ein Vorbeiflug am Jupitermond Amalthea. Die Analyse von Radiosignalen der Raumsonde gestattete Aufschluss über Masse und Dichte dieses kleinen Mondes (mittlerer Radius 83,45 km).

Basierend auf unterschiedlichen Modellen des inneren Aufbaus konnten die langwelligen Anteile des Gravitationsfeldes von Amalthea berechnet werden. Die angewandte Methode integriert numerisch infinitesimale Volumenelemente, die aufgrund von Amaltheas unregelmäßiger Form anhand der Geometriefaktoren elliptischer Koordinaten bestimmt wurden. Um die erforderlichen Berechnungen durchzuführen, wurde das Computer Programm GRASP („Gravity Field of a Planetary Body and its Influence on a Spacecraft Trajectory", zu deutsch „Gravitationsfeld eines planetaren Körpers und dessen Einfluss auf die Bahn einer Raumsonde") im Rahmen dieser Arbeit erstellt. Eine Routine in GRASP wendet die zweite Methode von Neumann zur Kalkulation der Massefunktionen an. Letztere wurden bis zum sechsten Grad und Ordnung ermittelt, basierend auf homogenen und realistischen heterogenen Modellen von Amalthea. Die normalisierten Massefunktionen zweiten Grades liegen in der Größenordnung von 0,038 für J_2 und -0,053 für J_{22}.

Die Position und die Geschwindigkeit von GALILEO zum Zeitpunkt der größten Annäherung zu Amalthea wurde vom Jet Propulsion Laboratory, NASA, zur Verfügung gestellt. Anhand dieser Daten und der Gravitationsfeldmodelle des Mondes konnte mit GRASP eine Vielzahl von Bahnen der Raumsonde während des Vorbeifluges berechnet werden. Die hierfür angewandte Methode basiert auf dem numerischen Integrationsverfahren von Runge-Kutta. Die Analyse der Bahnen liefert Geschwindigkeitsänderungen, hervorgerufen durch Amalthea's Form und Massenverteilung, die mit vorhandenen Doppler-Daten des Vorbeifluges verglichen wurden. Aufgrund einer fehlerhaften Trägerfrequenz standen allerdings nur einfache Doppler-Messungen („1-way Doppler data") von der Überwachung der Raumsonde zur Verfügung, die nicht genügend Genauigkeit aufweisen, um das Gravitationsfeld von Amalthea zu bestimmen – die Massefunktionen liegen innerhalb des Rauschens der Daten. Es war lediglich möglich, die Masse des Mondes zu errechnen und daraus folgend die mittlere Dichte (~ 860 kg/m³).

Die in der vorliegenden Arbeit berechneten Modelle von Amalthea können zur Planung von zukünftigen Weltraummissionen zum Jupitersystem herangezogen werden. Um nützliche Informationen über das Gravitationsfeld des Mondes zu erlangen, sollte ein wesentlich näherer Vorbeiflug als bei GALILEO angepeilt werden. Dieser sollte vorzugsweise in einer Höhe von 80 km über der Oberfläche und über einem Pol entlang der größten Achse von Amalthea erfolgen. Eine geringere Höhere würde noch bessere Resultate liefern, wäre aber aufgrund von Navigationsungenauigkeiten der Raumsonde riskant. Eine weitere Möglichkeit, Daten über den inneren Aufbau von Amalthea zu erlangen, wäre eine Mission, die in der Lage wäre, seismische und geologische Experimente vor Ort auszuführen.

CONTENT

0 INTRODUCTION

"To confine our attention to terrestrial matters would be to limit the human spirit." Stephen W. Hawking

It lies in the nature of humans to strive for further evolution and development, to go beyond frontiers and explore unknown shores in any field – including space. It is not only the urge for exploration, its challenge, glory and gratification, which got man to leave the Earth and go to outer space, but also the curiosity to learn about our origin – and fate; to explore new resources, strive for advanced medical development, improve our daily life on Earth, and, in a certain way, make it more comfortable. Space exploration is thus a term including many issues and endeavours.

The present work wants to touch an aspect of space exploration: the improvement of spacecraft navigation by means of enhanced planetary interior model derivation. The better the bodies in our solar system are known and modelled, the more accurately (and safely) a spacecraft can be navigated. In addition, the information about the internal structure of a planet, moon or any other planetary body can be used in arguments for different theories of solar system evolution.

In order to get more insight on the implementation of a spacecraft mission, the author was invited to spend a year as a research fellow at the Jet Propulsion Laboratory (JPL). JPL, a division of the California Institute of Technology in Pasadena, California, manages among other things space science missions for the National Aeronautics and Space Administration's (NASA) Office of Space Science, Washington D.C. The space project in the context of the present work is GALILEO, a mission dedicated to explore the Jovian system in great detail.

After years of successful exploration GALILEO's final experiment was the flyby of Jupiter's small inner moon Amalthea on November 5, 2002. It was anticipated to analyse two-way Doppler data with respect to Amalthea's gravity field, and thus interior structure. Unfortunately, but a considered risk common to space missions, the experiment was only partly successful: it was merely possible to receive one-way Doppler data which does not have sufficient accuracy to serve as input for the gravity field analysis. Nevertheless, information about the mass of Amalthea could be derived and data from the spacecraft closest approach to the moon is available for further analysis.

The focus of this work lies in a new approach for modelling the gravity field of small planetary bodies: the implementation of complex ellipsoidal coordinates for irregularly shaped bodies that cannot be represented well by a straightforward spheroidal approach, as it is the case for Amalthea. Because of the above stated difficulties the gravity field models of Amalthea have not been implemented into the analysis of the Doppler data but serve to a reverse approach of analysing GALILEO's trajectory. In order to carry out the required calculations the computer programme GRASP (**Gra**vity Field of a Planetary Body and its Influence on a **Sp**acecraft Trajectory) has been developed. As the name implies, GRASP furthermore allows deriving the impact of the body's gravity field on a spacecraft trajectory and thus permits predictions for further space mission flybys.

0.1 STRUCTURE OF THE INTRODUCED THESIS

Space exploration is a complex term and involves various issues; as well are the single issues multifaceted. In order to comprehend the interplay of the different aspects of space missions, a basic knowledge of space studies is essential. There are a couple of good space books and a lot of specialised papers on various space topics, but the actual implementation of specific knowledge and experience on the performance of a space mission, especially with regard to

its observations, is seldom written down. In addition to the above mentioned objective the present work tries to summarise and give basics of background information, as well as instructions, which play a part to the scope of the work; especially in thought of readers who are not familiar with space exploration.

The first part ('Discoveries in Space: The Jovian System') of the thesis thus gives an overview of the Jovian system, its origin and exploration, with emphasis on Jupiter's moon Amalthea and its discoveries until November 2002.

The second part ('Space Exploration: GALILEO as a Successful Example') focuses on the mathematical and physical explanations and expressions regarding a spacecraft trajectory and spacecraft tracking. The GALILEO mission and its achievements are described in chapter 5. Chapter 6 supplies the basics of orbital mechanics with respect to the trajectory of a spacecraft. The approximation of the trajectory is considered in GRASP. The field of Radio Science and its application for spacecraft communication and tracking, including Doppler data for planetary gravity field determinations, is explained in chapter 7. Chapter 8 is dedicated to GALILEO's flyby of Amalthea, the problems that occurred and the evaluation of the spacecraft data.

The third part ('Amalthea Models: Preparatory Derivations') deals with the mathematical expressions needed for the derivation of Amalthea's interior structure and gravity field models, and their influence on a spacecraft trajectory. In order to describe the location of points and their variations in space the definition of coordinate systems is necessary – given in chapter 9 for planetary bodies, including ellipsoidal coordinates, and in chapter 10 with respect to an inertial system in our solar system. Based on coordinate systems and Newton's law of gravitation, the gravitational potential of a planetary body can be derived, which is stated in chapter 11 and computed within GRASP. Chapter 12 explains GRASP, the computed expressions (taken over from the previous chapters), input and output options, and the optimisation of the programme.

Finally, the fourth part ('Amalthea Models: Gravity and Trajectory') of the present work deals with the models of Amalthea and their analysis, as well as the impact on a spacecraft trajectory. Various interior and resulting gravity field models of Amalthea, based on the current knowledge of the moon's composition and derived with GRASP, are stated in chapter 13. At last, in chapter 14, the impact of Amalthea's presence on a spacecraft trajectory is analysed and recommendations for future flybys are given. Conclusions, chapter 15, summarise the objective and the results.

Part I
Discoveries in Space:
The Jovian System

1 A Historical Overview

Since the evolution from primitive mammals the human race is interested in its further development, its growing, in getting to know where it came from and where it is going – and in reaching for the stars! Humans not only have been (and are) fascinated about their surrounding, but also about the sky above them.

First, little was known about the Earth, the Moon, the Sun or other planets and the stars – mystery laid upon them and mythology was playing a big part. But soon people started to understand the nature of these objects and astronomy became a renowned science.

1.1 Ancient Times

Historical documents reveal that peoples around the world named the bright stars in the sky, and the constellations played a big role in their myths and their lives, originated as a reaction to social and psychological needs – created to explain natural phenomenon, but also to give reasons for old traditions or to dramatically enrich the life of gods. Especially the old Greek mythology, adopted by the Romans, is a complex structure, involving stories about characters, which found a 'place in the sky'. The naming of extraterrestrial objects (carried out by the International Astronomical Union, IAU) is still based and continued after the old myths, although a mixture of Arabic, Greek, Roman, Indo-Germanic, etc. nomenclature is present*.

Soon it became clear that some of the stars were moving against the background stars and were therefore named after the Greek word 'planitis' for wanderer – planets. Only five of them are visible to the naked eye and named after the Roman gods for trade, love, war, weather and agriculture – Mercury, Venus, Mars, Jupiter, and Saturn.

Figure 1.1: Jupiter (Zeus) – Ceiling at the Frederiksborg Museum in Copenhagen, Denmark.

Jupiter – most of the time the brightest object in the sky, besides our Moon and the Sun, and visible in our night sky for most of the year – was given the name for the lord of the sky. He was the god for weather (responsible for rain, snow, hail and thunderstorm), therefore living on Mount Olympus, and called 'father of all gods and humans'. Every aspect of the universe and world matter was under his trial and he protected cities, foreigners and travellers. But he

* The origin of the individual names is not included and explained throughout the document.

was also a 'womaniser' – married to a couple of goddesses until his lasting marriage to Hera, to whom he nevertheless was unfaithful [12].

The predictability of the planet's cycle and the brilliance relative to nearby stars suggested control and dominance and implies how this planet came to be named for the Roman god Jupiter. As more became known about the physical nature of the planets, Jupiter lived up to its name.

1.2 Galileo Galilei and the 17th Century

Until the 16th century it was believed that the Earth was the centre of the universe – the Ptolemaic model. In the year of his death, Nicolaus Copernicus (1473-1543) published his "De Revolutionibus Orbium Caelestium (On the Revolutions of the Celestial Spheres)", placing the Sun at the centre of the solar system. His work stimulated a series of scientific accomplishments which led to an understanding of gravitational forces and eventually to planetary exploration.

More than 50 years later, after renowned astronomers like Tycho Brahe (1546-1601) and Johannes Kepler (1571-1630) further studied the motions of the planets, the Italian astronomer Galileo Galilei (1564-1642) was the first to use a telescope and observed Jupiter as a disk in January 1610 [35]. Although his telescope was constructed with small, simple lenses made of poor quality glass, he was able to see Jupiter's four largest satellites that now bear his name. The small star-like objects revolved around Jupiter in the equatorial plane at distances 6 to 26 times the planet's radius. Because the periods of revolution ranged from 1.8 to 16.7 days, the shifting positions of the small objects relative to each other and to the centre of the visible disk of the planet made it readily apparent that this was a system where small bodies orbited around a larger body. This discovery demonstrated that orbital motion can take place about a centre other than the Earth!

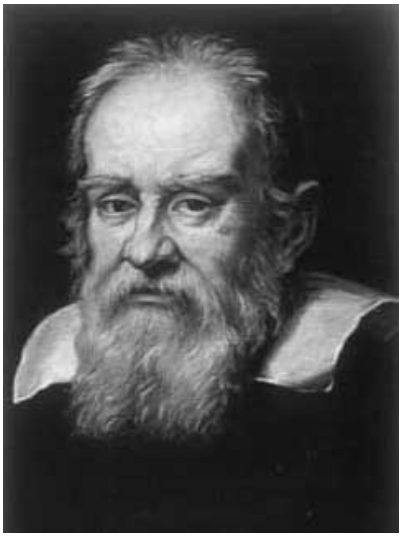

Figure 1.2: Galileo Galilei – Portrait by Justus Sustermans (1636).

The actual discovery was not without controversy, since Galilei's contemporary, the German Simon Marius (1573-1624), claimed precedence. However, Galilei published first and no proof exists of Marius' earliest sightings, so credit is generally assigned to Galilei. Nevertheless, Marius did suggest the names of the satellites now in use: Io, Europa, Ganymede and Callisto – all lovers of Zeus/Jupiter in Greek/Roman mythology. Because of his discoveries and scientific efforts, Galilei was a defender of the Copernican model, which

eventually led to two condemnations through the inquisition where he had to abjure his theories. Nevertheless, he secretly continued his scientific work.

In the second half of the 17th century Sir Isaac Newton (1643-1727) was formulating the theory of gravitation (chapter 6.1.1) and Giovanni Domenico Cassini (1625-1712) measured the distance between Earth and Mars. The timing of eclipses of the Galilean moon Io led to the first measurement of the velocity of light (214,000 km/s), carried out by Olaf Römer (1644-1710) in 1676. The dimensions of the solar system had thus been determined by the end of the 17th century and it was possible to convert the angular measurements within the Jovian system to actual distances. Furthermore, the volume and the mass of Jupiter could be derived and thus his density, revealing that the planet was a giant and that it could not have the same internal constitutions or composition as the Earth but must instead be composed of low-density material.

1.3 Amalthea

In the 18th century larger telescopes were constructed with mirrors in place of lenses that could be used to observe faint objects. In 1781 Sir Friedrich William Herschel (1738-1822) discovered the seventh planet – Uranus, named after the Greek god who was given birth by (and later married to) Gaia, 'mother Earth'. Urbain Jean Joseph Leverrier (1811-1877) and John Couch Adams (1819-1892) determined the eight planet's position independently, based on disturbances in the orbit of Uranus. As a result astronomers Johann Gottfried Galle (1812-1910) and Heinrich Louis D'Arrest (1822-1875) detected Neptune, god of sea and water, in 1846.

Nearly three centuries after the sighting of the Galilean satellites another Jovian satellite was discovered. In the late 19th century Edward Emerson Barnard (1857-1928) used the 36-inch Lick telescope in California, designing a way to cover the bright disk of the planet to detect faint nearby objects. On September 9, 1892, he found a small satellite orbiting Jupiter inside the orbit of Io – Amalthea, named after the nymph or goat that nursed Jupiter. He soon ascertained that the period of revolution of the new satellite was slightly less than 12 hours [3].

By 1951 seven more satellites of Jupiter were discovered, the thirteenth only 24 years later in 1975, just before the first spacecraft would arrive at Jupiter. The IAU has named all of them after lovers of Jupiter.

Figure 1.3: Edward Emerson Barnard.

2 Modern Exploration

As technologies evolved our understanding of the universe has grown. Now, with space exploration and robotic spacecraft coming into its sixth decade an enormous amount of data has been gathered and analysed, revealing fascinating facts about distant 'worlds' and the origin of our universe. Nevertheless, there are still mysteries in this endless wideness of space that want to be discovered.

2.1 Earth Based Observations

E. E. Barnard not only discovered Amalthea, he also utilised the refractors at the Yerkes and Lick observatories to measure the sizes of the Galilean satellites. Although these measurements of mass and diameter had uncertainties about 20 %, they permitted the first estimate of bulk density, revealing that the inner satellites were apparently composed of denser materials than the outer. In the first decades of the 20th century larger telescopes and modern techniques of photometry, polarimetry, and spectrophotometry exposed new information about the Galilean satellites and their properties with respect to colour, albedo, surface composition, atmospheres, etc.

With the beginning of space exploration by means of robotic spacecraft and space based telescopes in the 1970s and its advantage of observing outside the atmosphere's turbulences, Earth based techniques became less important. Nevertheless, the big observatories around the world are still used to observe the planets in our solar system, as they are in general cheaper than space missions and permanently available. A science group at the Planetary Radar at Arecibo Observatory, Puerto Rico, uses delay-Doppler mapping of the Galilean satellites to determine the surface properties and to look for different radar properties of the various terrain types. Another group at the Mauna Kea Observatory, University of Hawaii, is studying the small outer satellites of Jupiter using wide field CCD surveys. Within the last four years they have discovered 45 new irregular satellites of Jupiter and are still looking for new ones [41].

2.2 Robotic Spacecraft

The launch of the Russian satellite Sputnik I on October 4, 1957, marked the beginning of the space age – an era full of fascinating discoveries, which still goes on.

In the 1970s technologies were already so advanced that plans by the United States' National Aeronautics and Space Administration (NASA) were formulated to explore the outer solar system by means of robotic spacecraft, the prime target being Jupiter. Two pairs of spacecraft, Pioneer 10 and 11 and Voyager 1 and 2 have now flown by Jupiter and the other giant planets. The Pioneers operation terminated in 1997 and 1995 respectively, but the Space Projects Division Operations Center continued to track Pioneer 10 on occasion as part of an experiment in chaos theory. The last signal was received on January 23, 2003, as the spacecraft's radioisotope power source has decayed [46].

The Voyagers are still heading away from the Sun, sending weak signals of their position in outer space. Flight controllers believe both spacecraft will continue to operate and send back valuable data until at least the year 2020 [47].

2.2.1 PIONEER AND VOYAGER

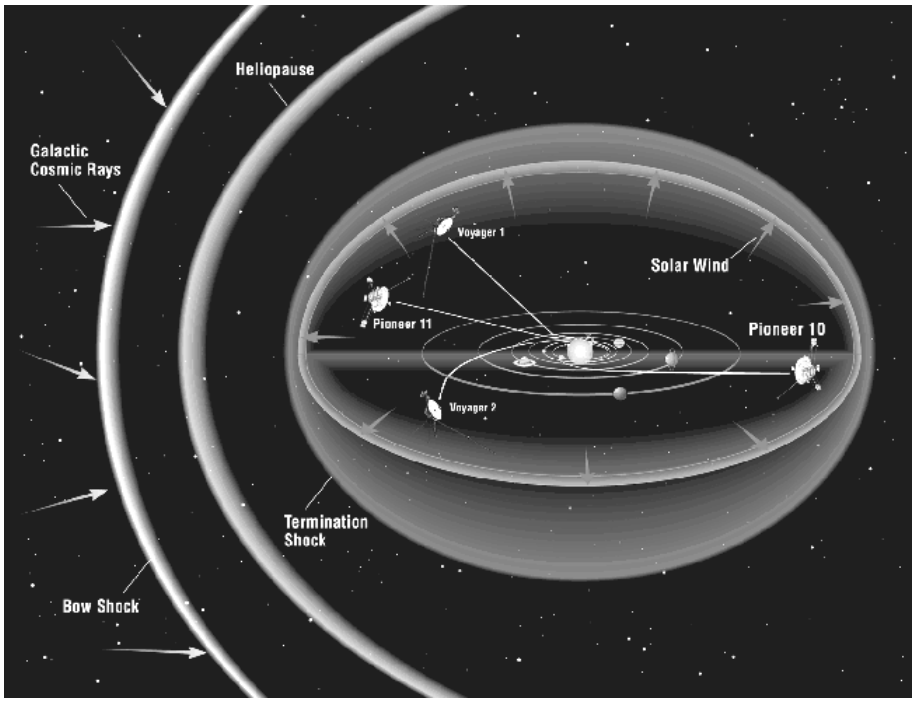

Figure 2.1: Positions of Pioneer 10 & 11 and Voyager 1 & 2 in 2001.

Pioneer and Voyager represent two different types of spacecraft [19]. The primary objectives of the Pioneer project were not so much to investigate the Jovian system as to demonstrate that spacecraft could be sent successfully to the outer solar system. Launched in 1972, and 1973 respectively, the Pioneer spacecraft arrived at the Jovian system in 1973, and 1974, sending back to Earth a few low-resolution images and new information about the temperature and pressure within Jupiter's atmosphere, as well as improved masses for all four Galilean satellites.

The Pioneers served as pathfinders for a more ambitious NASA project: Voyager. Launched in 1977 and arriving at Jupiter in 1979, the two spacecraft began one of the most successful harvests of spatially resolved astronomical information. Because of the more sophisticated designed spacecraft and better communication link, data could be collected more easily and in higher quality. Just to name a few achievements, the Voyagers detected a faint ring about Jupiter's equator, sent back to Earth the first pictures of the small moon Amalthea (Figure 4.2), revealed Io's volcanic activity and the icy structure of Europa. For the first time it was possible to see the Jovian satellites as individuals!

2.2.2 GALILEO AND CASSINI

Encouraged by the success of the Voyager-Jupiter encounters, NASA continued its efforts to carry out the GALILEO Mission (chapter 5) to explore the Jovian system in more detailed. Launched in 1989 and arriving at Jupiter in 1995 the GALILEO spacecraft very successfully gained high-resolution data and revealed detailed information about Jupiter, the Galilean satellites and some smaller satellites in an extended mission which terminated with a spectacular plunge of the spacecraft into Jupiter on September 21, 2003.

On its way to Saturn the Cassini/Huygens spacecraft, a joint mission of NASA and the European Space Agency (ESA), passed by Jupiter in December 2000. Observations and measurements by GALILEO and Cassini were coordinated to examine Jupiter's huge

magnetosphere and other parts of the Jovian system in ways that neither spacecraft could have done alone.

Figure 2.2: Cassini's distant flyby of Jupiter (artist impression) [Courtesy NASA/JPL-Caltech].

2.2.3 Future Exploration

GALILEO discovered new worlds that now raise even more questions; in particular regarding the icy moons Europa, Callisto and Ganymede, which might have subsurface oceans, as current models imply. Life on Earth has been discovered at great ocean depths, beyond the penetration of sunlight, thriving on up-welling chemical nutrients from the interior of the planet. If liquid water were to exist on the Galilean moons, it would not be unreasonable to speculate on the existence of life there, perhaps forming near undersea volcanic vents.

NASA is developing plans for an ambitious mission to orbit these three planet-sized moons of Jupiter. The Jupiter Icy Moons Orbiter (JIMO) would orbit each of the moons for extensive investigations of their makeup, their history and their potential for sustaining life [45]. The mission would be launched sometime in the next decade.

Figure 2.3: Europan life clusters around a hot vent, similar to the 'black smokers' found near Earth's ocean trenches (artist impression by David Hardy).

3 ORIGIN AND STRUCTURE OF THE JOVIAN SYSTEM

The origin of our universe is still under debate but it is assumed that everything started in an out-rushing of material, called the Big Bang, some 12 to 16 billion years ago. After millions of years, enough heavy elements were formed to allow the aggregation of galaxies or huge masses of typically 10^{11} stars. Our own galaxy, the 'Milky Way', formed about 10 to 12 billion years ago.

The stars within those aggregations form in clusters from nebular concentrations of interstellar material – huge clouds of atoms, molecules and dust grains. Extreme rotation of the contracting cloud could lead to the formation of a flat disc: a star emerging from the central part and planet-forming particles from the heavier elements concentrated in the surrounding dust. Our solar system began to form from such a cloud about 4.6 billion years ago [13].

3.1 OUR SOLAR SYSTEM

The solar system is commonly said to have nine planets, as shown in Figure 3.1. All the planets revolve around the Sun in one direction counter clockwise when viewed from north, in just about one plane called the ecliptic plane. In order from the Sun, they are Mercury, Venus, Earth, Mars, Jupiter, Saturn, Uranus, Neptune, and Pluto.

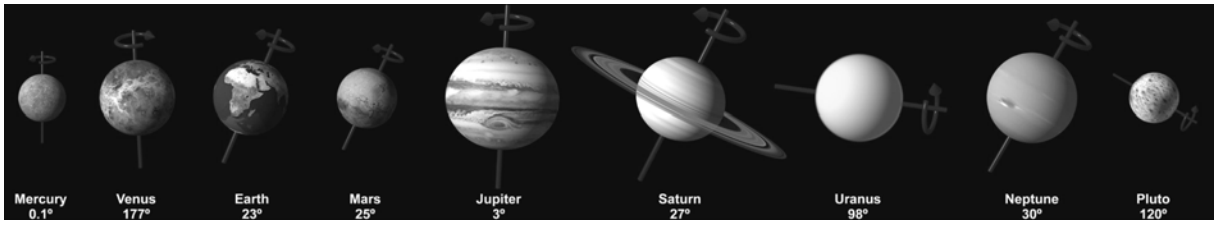

Figure 3.1: The nine planets of our solar system and their obliquity (sizes and distances are not to scale) [Courtesy Calvin J. Hamilton].

The first four planets are sometimes called the terrestrial planets because of their nearness to Earth and the similarity of their rocky, metallic composition. The next four planets are sometimes called the giant or gaseous planets. Today, many astronomers tend to classify Pluto as an asteroid rather than a planet as it is in contrast to the other outer planets a small and rocky body with a very elliptical and inclined orbit around the Sun.

3.1.1 SMALL BODIES

Furthermore, the solar system is populated by a variety of small bodies ranging from microscopic dust particles to meteoroids and asteroids, with masses of up to about 10^{20} kg. Most asteroids, called after their faint star like images, reside in the main asteroid belt between the orbits of Mars and Jupiter. Other asteroid groups populate the inner and outer solar system, e.g. the Trojan asteroids (named after characters in Homer's Trojan War epics) which move in the same orbit as Jupiter but in average 60° ahead or behind the planet, identified as the Lagrangian points [13].

Meteoroids are located in various orbits around the Sun and are mainly the fragments of asteroids that collided.

Comets are low-density icy bodies, which primarily occupy the space at the very periphery of the solar system in the Oort cloud in about 150,000 AU (=astronomical unit, 1 AU equals the distance Sun-Earth) from the Sun, and possibly also in a closer disk-shaped space beyond the orbit of Neptune, called the Kuiper Belt (about 50-500 AU from the Sun).

In recent years, astronomical work has thrown up several big icy objects in the Kuiper Belt region, the latest discovery being Sedna – the most distant object found orbiting the Sun. Observations from the research team at the California Institute of Technology that found the body, show that Sedna is similar in size to Pluto and a mixture of rock and ice. This new discovery will probably reignite the debate about what constitutes a planet [5].

3.1.2 FORMATION

The solution to the mystery of the origin of the solar system is an ongoing detective story. Nevertheless, some theories are well accepted but await confirmation through the actual visit of a planetary system in formation.

In short, our solar system originated the following way: when a cloud of interstellar material acquires a high density of gas, gravity begins to dominate the balance of forces and the gas eventually forms a rotating disk, called the solar nebula, with a central spherical condensation for the proto sun. While the proto sun evolves into a star the rest of the solar nebula, consisting of microscopic grains and gas, aggregates into larger bodies, so called planetesimals. These bodies formed the pool of material from which the planets were accreted. In the final stage of the formation of our solar system, swarms of the planetesimals interact gravitationally and planet-sized bodies grow. Their composition and size depended on their distance from the star and the density and composition of the proto-planetary nebula: in the outer solar system ices complemented the planetesimal mass supply, and still larger bodies formed. Gas was accumulated around the giant planets because of their size and therefore higher gravity. The bodies in the asteroid belt, the Kuiper belt and the Oort cloud are believed to be remnants of the formation process [15].

3.2 JUPITER AND ITS SATELLITES

Figure 3.2: Image composite of parts of the Jovian system [Courtesy Calvin J. Hamilton].

The Jovian system is regarded as a ‘mini-solar system’, with many features in common with the larger system, including a clear change in the composition of the satellites with distance from Jupiter. The discoveries of GALILEO revealed that the Jovian system is remarkably diverse in its physical and chemical structure. The observations have provided valuable clues to the conditions under which this system formed. It is believed that Jupiter, the Galilean satellites and the innermost satellites were formed by a local self-gravitational condensation of the nebular matter analogous to the solar system. All other outer satellites are assumed to

be captured in the very early days of the formation process, and are probably remnants of a larger body [10].

3.2.1 JUPITER

Jupiter is the largest planet of our solar system (71,400 km radius), having more mass than all the other planets put together (1.8986×10^{27} kg). It revolves around the Sun in 11.86 years at a mean distance of 5.203 AU [34]. The planet is a rotating gas-giant, consisting mostly of molecular hydrogen (79 % by mass) and helium (19 %), and trace amounts of water vapour, methane, and ammonia. Below an atmospheric cloud the pressure increases rapidly with depth, compressing the gases more and more until the material behaves more like a liquid (metallic hydrogen). It is believed that Jupiter has a dense liquid or solid core of about 14 Earth masses compressed to 22,000 kg/m³ and a radius of 1.5 Earth radii (Figure 3.3).

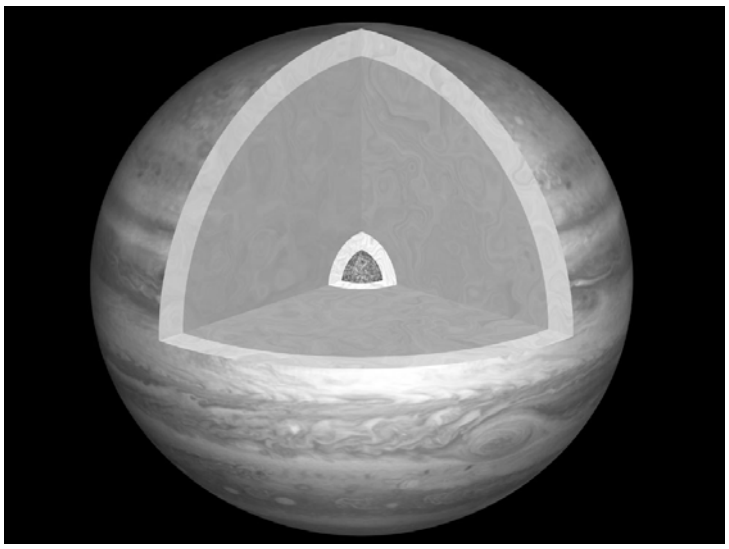

Figure 3.3: Jupiter's interior [Courtesy Calvin J. Hamilton].

Convection of the metallic hydrogen shell causes the strong magnetic field of Jupiter. It is the largest of the planetary magnetospheres – its great expanse could envelope the Sun and much of its corona. This size, the rapid rotation of the planet ($9^h\ 55^m\ 27.3^s$) and the volcanoes of the moon Io conspire to produce the richest array of magnetospheric phenomena in the solar system.

Clouds, arranged in dark belts and bright zones parallel to the equator, cover the planet and numerous thunderstorms concentrate in specific zones above and below the equator. A long-lived feature is the Great Red Spot, probably first seen in 1665 by Giovanni Cassini, a giant whirlpool storm that can reach four Earth diameters.

3.2.2 INNER SATELLITES

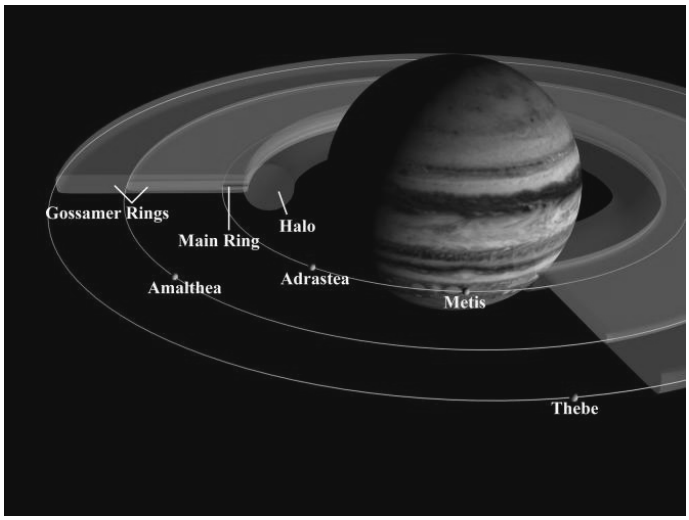

Figure 3.4: Jupiter's ring system and the four inner satellites [Courtesy NASA/JPL-Caltech].

The innermost group of small rocky moons, consisting of Metis, Andrastea, Amalthea, and Thebe, orbit Jupiter within the orbit of Io at distances smaller than 3.5 planetary radii and are part of the planet's faint ring structure. They are irregular shaped fragments possibly from a larger body that was disrupted in the past. As the emphasis of this work is on Amalthea, more details on this moon and its creation are given in chapter 4.

3.2.3 GALILEAN SATELLITES

The Galilean satellites revolve around Jupiter in nearly circular orbits in the equatorial plane of the planet. Their orbits are located within 6 to 26 planetary radii of the centre of the planet and the inner three are locked in resonance. During the process of their formation the Jovian heat led to an almost complete escape of ice from the nearest, Io, and an almost complete retention of ice on the farthest, Callisto [6].

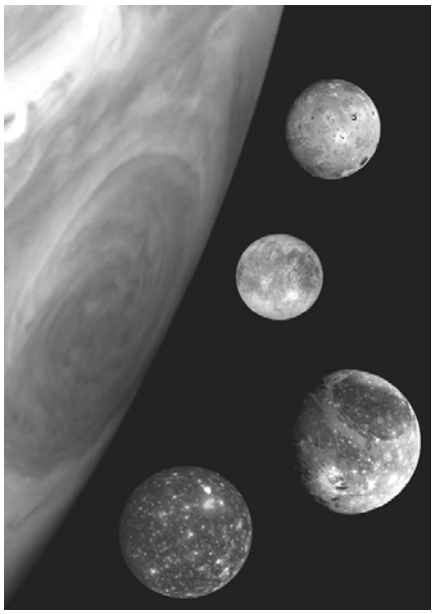

Figure 3.5: Galilean satellites – Io, Europa, Ganymede, Callisto (top to bottom) [Courtesy NASA/JPL-Caltech].

Io (1821 km radius) is the only place in the solar system besides the Earth that has volcanic activity, which is continually modifying the surface. It is caused by tidal interaction through Io's elliptical orbit around Jupiter, and the gravitational influence of the other moons. The composition of the hot lavas may be more similar to a type of volcanism that occurred on the Earth more than three billion years ago. Like Europa (1565 km radius) and Ganymede, Io has a metallic core.

Evidence supports a theory that liquid oceans exist under Europa's icy surface. There are places on the surface where recognizable features that once were whole have been separated from each other by new, smooth ice. Indications also show volcanic ice flows, with liquid water flowing from Europa's volcanoes. These discoveries are particularly intriguing, since liquid water is a key ingredient in the process that may lead to the formation of life! GALILEO's magnetic data provides information that liquid saltwater layers under ice also exist, farther below the surface, on Ganymede and Callisto.

Ganymede, the largest moon in the solar system (with 2634 km radius even bigger than the planet Mercury), generates a magnetic field, just as Earth does, and is the first moon of any planet known to possess an intrinsic magnetic field. The moon has a very thin hydrogen atmosphere and its rock-ice surface shows high tectonic activity, with faulting and fracturing.

The composition of the more distant moon Callisto (2403 km radius) is fairly uniform throughout, indicating it did not follow the same evolutionary path as the other three moons. Callisto's rock-ice surface shows evidence for extensive, though still mysterious, erosion that smoothes out features on the heavily cratered surface.

3.2.4 OUTER SATELLITES

The inner and the Galilean satellites are also called regular satellites. The other outer satellites are irregular satellites as they orbit Jupiter in a retrograde orbit, meaning they revolve about the planet in a direction opposite to the planets rotation [3]. Only one satellite has a prograde orbit with an orbital radius of about 100 Jupiter radii. The other irregular outer satellites form two sets with elliptical and inclined orbits. One group consists of five small satellites that revolve about the planet at average distances of 150 planetary radii, their names ending with the letter a. The other group has names ending with the letter e and orbit Jupiter at distances around 300 planetary radii. In the last four years dozens of these small objects have been discovered mainly by researches at the University of Hawaii, bringing the total of known Jupiter satellites to 63.

4 AMALTHEA: DISCOVERIES UNTIL NOVEMBER 2002

The following chapter contains a collection of the discoveries and properties of Jupiter's moon Amalthea, derived before the GALILEO flyby on November 5, 2002. After a brief Greek myth, emphasis is given on the shape, structure and origin of the moon, with respect to the objective of this work.

4.1 GREEK MYTHOLOGY AND HISTORY

To save the life of her last unborn child Zeus for fear that her husband Kronos would devour it like the other children, Rhea gave birth to it on the Greek island Crete [12]. The nymphs on the island took care of the baby and nursed it with milk from the goat Amalthea, while the priests where dancing and making a lot of noise to distract the father and cover the cries of Zeus (Figure 4.1).

Figure 4.1: The upbringing of Jupiter - Joachim von Sandrart (17th century), National museum Nürnberg, Germany.

Jupiter's moon Amalthea was discovered by Edward E. Barnard on September 9, 1892, using the 0.9 m Lick-refractor in California, USA. Observations by him and others immediately after the discovery established the satellite's orbit to be approximately circular, with a period of 11.92 hours and a semi-major axis of 2.55 Jupiter radii [19].

4.2 OBSERVATIONS

Amalthea is an extremely difficult object to observe from Earth due to scattered light from nearby Jupiter. Consequently little was known about the moon until the Voyager flybys in 1979. Voyager 1 passed within 420,000 km of Amalthea, and Voyager 2 came within 560,000 km, which resulted in images with a spatial resolution of about 10 km [3]. These first pictures revealed an irregular potato-shaped body with a cratered surface (Figure 4.2). Analysis of the Voyager data with respect to shape and surface features of Amalthea are discussed in detail by Stooke [28].

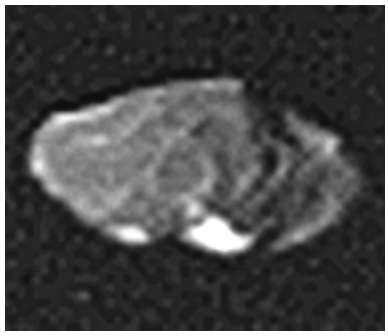

Figure 4.2: First image of Amalthea, taken by Voyager 1 on March 5, 1979 [Courtesy Calvin J. Hamilton].

More than 15 years later, the Solid State Imaging (SSI) camera on board the GALILEO spacecraft has imaged the four small inner Jovian satellites (Figure 4.3) on nearly every orbit of the nominal tour in sufficient detail, regarding shape, colour and photometric information. 75 % of the data on Amalthea were taken through GALILEO's ninth orbit in June 1997, where the best image resolution was 5.4 km/pixel [30]. In total, 23 images of Amalthea were returned.

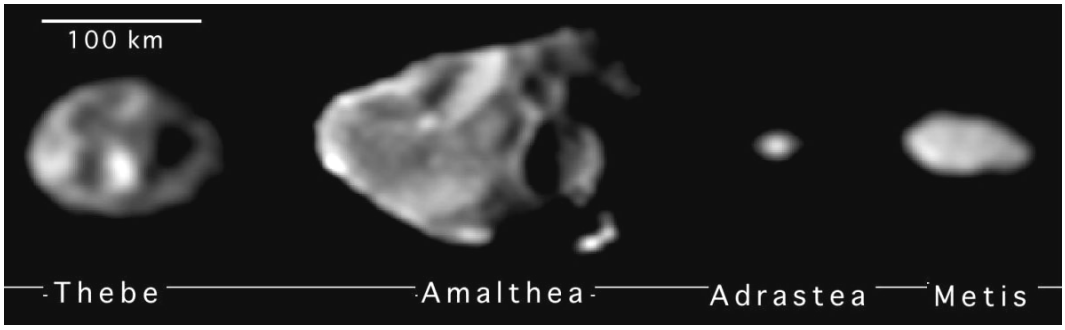

Figure 4.3: The best Galileo images of the four small inner Jovian satellites, north is up [Courtesy NASA/JPL-Caltech].

4.3 GEOMETRY AND SURFACE PROPERTIES

Amalthea's orbital and ellipsoidal parameters are specified in Table 4.1. The definition of the parameters is given in chapter 6.1 (Table 6.1), respectively 9.4; for the local coordinate system parameters refer to chapter 10.2 (10-1).

As already mentioned, Amalthea revolves around Jupiter in about 12 hours. Tidal forces due to the planet's gravitational field have slowed the moon's rotation rate so that it is synchronously locked.

orbital parameters		*ellipsoidal parameters [km]*		*local coordinate system*	
semi-major axis	181.3 x 10^3 km	*a*	125 ± 2	α_0	268.05 – 0.009 x T[°]
orbital period = rotational period	0.498179 days	*b*	73 ± 2	δ_0	64.49 + 0.003 x T[°]
eccentricity	0.003	*c*	64 ± 2	*W*	231.67 + 722.631456 x d
inclination	0.4°	*mean radius*	83.45 ± 2.4		

Table 4.1: Amalthea's orbital, ellipsoidal and coordinate system parameters [34] [30] [8].

Amalthea's irregular shape cannot be represented well by a triaxial ellipsoid. The values given in Table 4.1 describe a best-fit ellipsoid, which is derived from the GALILEO images using specific evaluation techniques (chapter 9.5). The volume estimate from these data amounts to $2.43 \pm 0.22 \times 10^{15}$ m³ [42].

Using the GALILEO images, Peter Thomas and his team from Cornell University have calculated a shape model for Amalthea, giving the surface radius in 5° x 5° steps (latitude, western longitude), which is graphically represented in Figure 4.4.

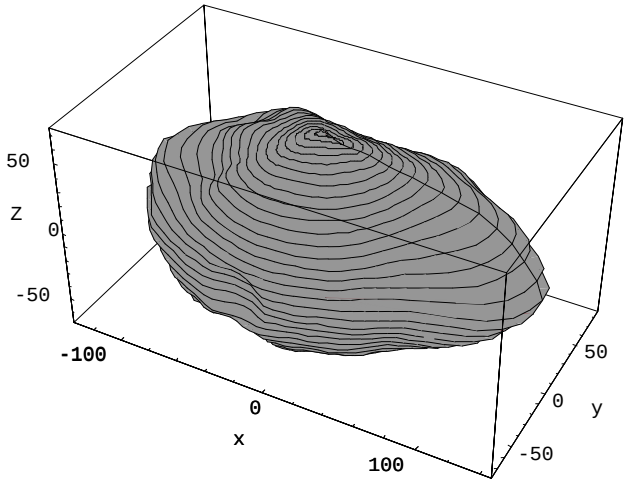

Figure 4.4: Amalthea's shape [data courtesy by P. Thomas, Cornell University]

The moon is heavily cratered and several craters have diameters that approach the satellite's mean radius. The largest crater with a diameter of 90 km and a depth of at least 8 km has been named Pan by the IAU. This intense bombardment that Amalthea has undergone must have produced abundant loose material for a regolith surface, which depths could reach more than one kilometre.

Amalthea is not only deep within the gravity field of Jupiter but also in a very intense part of its magnetosphere. Charged particle bombardments and micro-meteoritic impacts contaminate and alter the surface of the moon [30]. The low reflectivity of its surface and the dark-red colour could be due to sulphur-rich material expelled from nearby Io.

Consequently, the surface composition, the colour and reflectivity do not reveal anything about the nature of Amalthea's interior.

4.4 ORIGIN AND INTERNAL COMPOSITION

Two scenarios exist, which describe the origin of Amalthea. In one scenario the moon would have accreted near its present orbit during the formation of the Jovian system. Immediately after Jupiter's formation, the planet extended far beyond Amalthea's current position and did not become smaller until some hundred thousand years later. Therefore, the formation of Amalthea began much later than the Galilean satellites. Depending on the temperature of the nebula the composition of the moon varies. It could contain highly refractory, rocky materials like refractory oxides, nickel-iron, and possibly pyroxene, which would lead to a mean density of more than 3000 kg/m³ [10].

In the other scenario Amalthea is assumed to be a captured body, with a composition similar to that of the Trojan asteroids in Jupiter's orbit. Such an object would consist of carbonaceous minerals, which probably formed in a reasonably cold part of the solar system and thus retains

high substances of volatile compounds, such as water or gas. It could be compound e.g. of graphite grains, silicon carbide, iron sulphide, and clay minerals and consequently have a low density, probably less than 2000 kg/m³ [13].

Jupiter's strong tides act on Amalthea, elongating it towards Jupiter and compressing it normal to its orbital plane. Nevertheless, tidal distortion did not form an ellipsoid, as can be clearly seen by simply considering the significant asymmetry along the major axis of the moon and the straight-line ridge crests which are obvious in the images. Amalthea's heavily cratered surface and its degree of irregularity are evidence in favour of the argument that the moon is a collisional fragment, left over from the destruction of an older, larger body. In favour of this theory are as well the ratios of the moon's axis *a*/*b* and *a*/*c* [19].

Furthermore, considering the above statements, it can be concluded that Amalthea must have more than zero internal shear strength; otherwise it would have been crushed into a spheroidal shape by its own gravity. This corresponds to the low temperature profile within the interior of small bodies, due to the high surface-volume ratio, and thus internal strength towards extended shear tension. The central pressure of a sphere with Amalthea's size and low density would be only ~10 bars [40].

Two possibilities arise out of that: Amalthea is a single strong object, or it is a relatively weak one reassembled by the agglomeration of smaller objects (Figure 4.5). In the latter case, the form of the satellite is determined by the shape and size distribution of the fragments, not by the satellite's density [6].

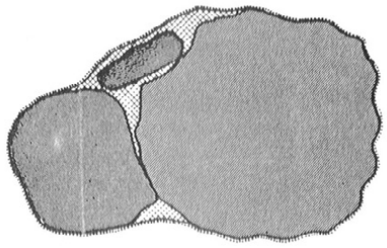

Figure 4.5: Schematic cross section of a heavily cratered satellite with reaccumulated large fragments and some small fragments that slightly smooth the resulting one.

4.4.1 POROSITY

In order to specify the interior of such a fragmented object with pore spaces, which could not be closed due to the low interior pressure, the degree of porosity Φ needs to be defined – considering a body with volume τ and icy, rocky and empty (void) components [17]:

$$\Phi = \frac{\tau_{voids}}{\tau} = 1 - \frac{\rho_m}{\rho_0} = 1 - \rho_m \frac{\rho_{rock}(1-C) + \rho_{ice} C}{\rho_{rock}\rho_{ice}} \qquad 0 \le \Phi \le 1 \qquad (4\text{-}1)$$

with ρ_m being the mean density of the whole body and ρ_0 the density of the material or the rock-ice composition, represented by the rock concentration C:

$$C = \frac{m_{rock}}{m_{rock} + m_{ice}} \qquad (4\text{-}2)$$

A non porous uniform material, or body, would thus be characterised by $\Phi = 0$.

For simplicity it is assumed that density increase towards the centre of the body is only due to the reduction of porosity, neglecting material compression as a result of self-gravitation.

Other planetary bodies in the same general size range like Amalthea (below a volume of about 10^7 km³) appear to have large porosities (e.g. asteroids Mathilde and Eugenia with $\Phi \sim 0.5$ if made of carbonaceous material, Saturn's satellites Janus and Epimetheus with $\Phi \sim 0.3$ if made only of water ice). Smaller bodies may have even larger porosities (e.g. Pandora and Prometheus at Saturn) but the mass determinations for the Saturn satellites are indirect and may contain errors which the observation of the space mission Cassini will hopefully sort out. All in all a porosity of $\Phi = 0.3$ to 0.5, even if regarded as very high a few years ago, seems reasonable in line with recent observations. A porosity of this value would still result in a sample density of only 1500 kg/m³ or less, which leads to the conclusion that there must be some ice content within the body interior even in the presence of high porosities [40].

Part II
Space Exploration: GALILEO as a Successful Example

5 Mission to Jupiter – GALILEO

The GALILEO mission evolved from studies in the early- and mid-seventies designed to develop outer solar system mission concepts to follow the Pioneer and Voyager flybys. As the nearest and largest of the giant planets, Jupiter was regarded as the logical first target of the next stage of exploratory missions. As a Jovian orbiter and probe was approved by NASA, it was fitting that it be named after the first explorer of the Jovian system, the Italian astronomer Galileo Galilei. After years of planning, designing, building, and rebuilding, GALILEO was launched in October 1989 and sent on its voyage via Venus and the Earth (twice) and arrived at Jupiter in December 1995. GALILEO was an international effort, with Germany providing propulsion modules and two major instruments, and science experiments carried out by more than 100 scientists from the United States, Great Britain, Germany, France, Canada and Sweden.

After twelve years of pre-launch development and planning, six years of interplanetary cruise, and nearly eight years in orbit, the exciting quarter-century odyssey of GALILEO came to an end. It circled the solar system's largest planet 35 times, travelled 4,631,778,000 kilometres on 925 kilograms of propellant, returned over 30 gigabytes of data (including 14,000 pictures) and finally disintegrated in Jupiter's dense atmosphere on September 21, 2003, at 6:57 p.m. UTC [39].

5.1 The Role of the Jet Propulsion Laboratory

In 1936, after a couple of small explosions in the rocket test facility at the California Institute of Technology, a group of hobby rocket scientists, supported by Theodore von Kármán (1880-1963), was forced to leave the campus and seek another place for their tests. They moved to the Arroyo Seco, a dry canyon wash a couple of miles northwest of the university, where they leased land from the city of Pasadena. From this modest beginning, the Jet Propulsion Laboratory (JPL) would begin to take form.

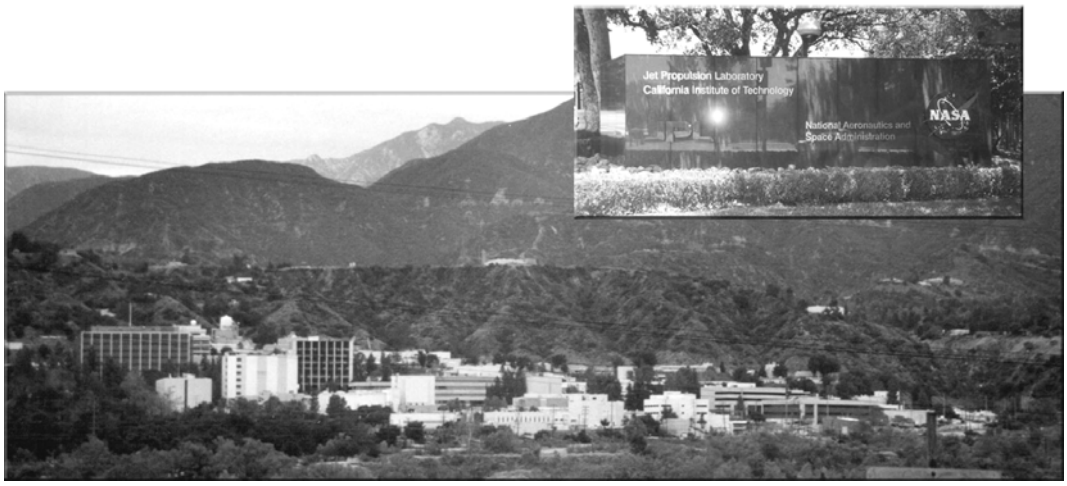

Figure 5.1: Jet Propulsion Laboratory (JPL).

Until the 1950s JPL coordinated the development and manufacturing of missiles and rockets for the military [23]. After the launch of the first orbiting spacecraft, the Russian Sputnik I, JPL quickly built an Earth satellite to go atop an Army-supplied booster rocket – and America joined the Space Age nearly four months later with the successful launch of this so called Explorer I on January 31, 1958. By 1959 the Lab got almost wholly out of the propulsion business when it discontinued missile work in favour of creating robotic probes for NASA.

Since then JPL was, and still is, responsible for the development and implementation of unmanned spacecraft missions to the Moon, Venus, Mars, Jupiter, other planets, and small objects. Furthermore, it is active in the exploration of our home planet, as well as the deeper universe, and manages the Deep Space Network (DSN), a network of antenna stations located in Spain, Australia and Southern California, that tracks spacecraft and captures its data (chapter 7.1.1). GALILEO was one of the most successful but also challenging missions carried out at JPL.

5.2 MISSION OBJECTIVES

GALILEO is not a 'Jupiter mission' in the traditional sense of a focused space mission to a given target. It is rather an integrated project addressing multidisciplinary objectives concerning the entire Jovian system. The system is important both for the insights it gives about conditions in the early solar nebula, 4.5 billion years ago, and for the understanding of the bewildering array of processes and phenomena which have affected the evolution of the planets and which control their environments and futures.

The scientific objectives of the mission are given in detail in Appendix A [25]. A particular interest was the atmosphere of Jupiter, as the planet is essentially a transitional object between terrestrial planets and stars, being composed primarily of hydrogen and helium in approximately solar proportions, with an internal heat source from ancient accretionary heating and gravitational collapse. A second principal interest was the regular satellite and ring system. Not only because it is regarded as a 'mini-solar system', but also because each of the planet-sized Galilean satellites is an unique and fascinating object to explore. Furthermore, the understanding of the structure, composition and dynamics of the huge Jovian magnetospheric environment was a major goal.

5.3 SPACECRAFT AND INSTRUMENTS

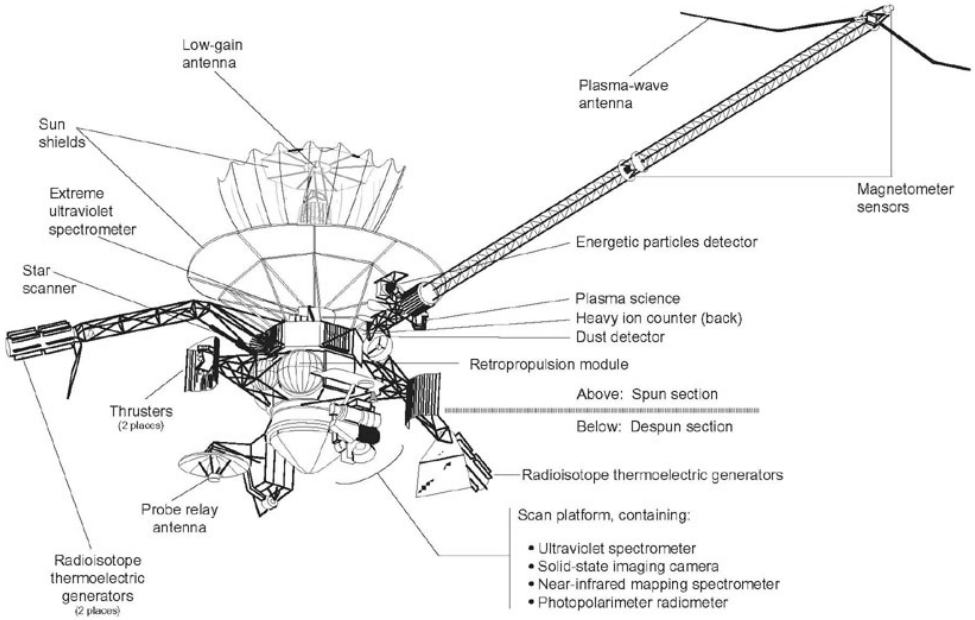

Figure 5.2: View of the GALILEO orbiter.

The GALILEO spacecraft design reflects the very demanding objectives of the mission. It consisted of an orbiter and an atmospheric entry probe, which was carried by the orbiter and deployed 150 days prior to Jupiter encounter. As the first dual-spin planetary spacecraft the

GALILEO orbiter combined in-flight stabilisation by a spinning section around a major axis and a non-spinning section for a fixed orientation for cameras and other remote sensors (Figure 5.2). Its weight was 2,223 kilograms at launch and it measured 5.3 metres from the top of the low-gain antenna to the bottom of the descent probe. The orbiter's spinning section carried instruments to study charged particles and magnetic fields (including magnetometer sensors mounted on an 11-meter-long boom to minimise interference from the spacecraft's electronics).

The orbiter included a telecommunications system, a propulsion system, and an attitude and articulation control subsystem. The scientific payload, consisting of 11 imaging instruments and detectors, was connected to the command and data system. For the gravitational experiments the antennas and the radio system of the telecommunications unit were used (chapter 7).

5.4 Mission Achievements

Before GALILEO arrived at Jupiter, a testing of the high-gain antenna failed – it stuck partway open, rendering it useless. To still achieve the goals of the mission, the less-capable low-gain antenna was used in combination with new data compression software and adaptations to the ground antennas of the DSN. The efforts solving the problem paid off after the spacecraft began orbiting Jupiter. Originally planned for a mission of two years, GALILEO withstood the radiation exposure, generated by Jupiter, much longer than expected and three extension of the primary mission could be carried out, one of them being dedicated to the moon Europa [44].

5.4.1 Asteroid flybys

GALILEO became the first spacecraft ever to encounter an asteroid when it passed close by Gaspra on October 29, 1991. Pictures and other data revealed a cratered, complex, irregular body of about 20 kilometres, with a possible magnetic field. On August 28, 1993, GALILEO flew by a second asteroid, this time a larger, more distant asteroid named Ida. Scientists made a dramatic discovery when they found that Ida has its own moon, Dactyl, making it the first asteroid known to have a natural satellite.

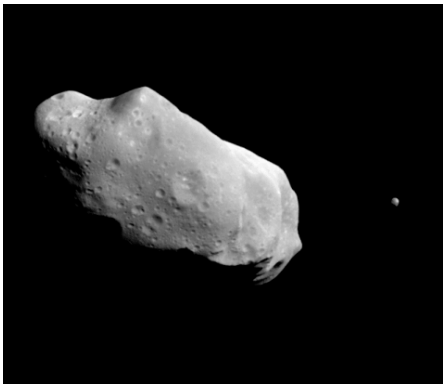

Figure 5.3: Asteroid 243 Ida and moon Dactyl on August 28, 1993 [Courtesy NASA/JPL-Caltech].

5.4.2 Comet event

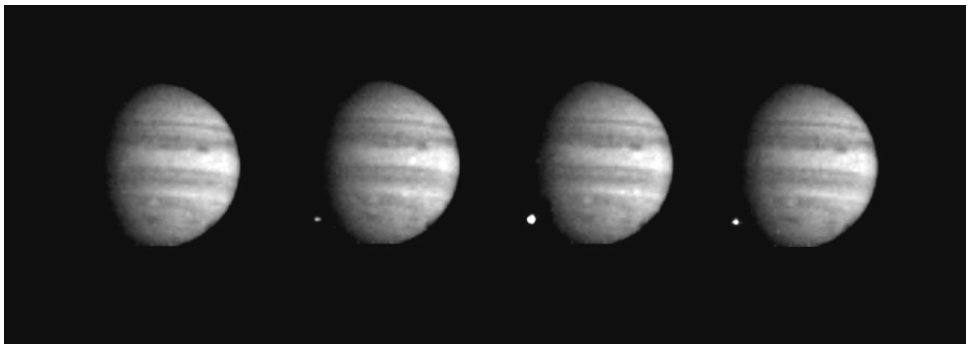

Figure 5.4: Luminous night-side impact of fragment W of Comet Shoemaker-Levy 9 on July 22, 1994 [Courtesy NASA/JPL-Caltech].

The discovery of Comet Shoemaker-Levy 9 in March 1993 provided an exciting opportunity for GALILEO's science teams and other astronomers. The comet was breaking up as it orbited Jupiter and was headed to dive into the giant planet's atmosphere in July 1994. The GALILEO spacecraft, approaching Jupiter, was the only observation platform with a direct view of the impact area on Jupiter's far side and was therefore able to obtain spectacular images of the comet impacts.

5.4.3 Jupiter and its satellites

GALILEO's encounters of Jupiter and its satellites were much closer than those performed by the Voyager spacecraft, extending our knowledge of the Jovian system enormously (chapter 3.2). It was the first spacecraft ever to measure Jupiter's atmosphere directly with a descent probe, and the first to conduct long-term observations of the Jovian system from orbit around Jupiter. A key science finding was the evidence that a liquid ocean has existed and probably still exists beneath Europa's icy surface.

6 Orbits and Interplanetary Travel

In order to exactly describe the motion of a spacecraft or any other body in space, it is necessary to take into consideration the attraction of all bodies in the solar system. But there is no single, general analytical solution that describes multi-body motions, not even a three-body problem, e.g. the Sun-Earth-Moon-System, can be solved uniquely. Therefore simplifications to the problem need to be made. In some cases a solution for a two-body problem is sufficient, e.g. the motion of a planet around the Sun or the Moon around the Earth. If more than two bodies are involved, the prediction of motions is usually derived by numerical integration, where the problem can be solved with any required accuracy.

In addition to the gravitational disturbances, a spacecraft is exposed to other perturbing forces that affect its orbit and its orientation within. It is therefore not possible to describe the motion of a spacecraft with a single orbit or trajectory, but with the summation of small orbital sections. This chapter will give an overview of the above mentioned problematics.

6.1 Orbital Motion and Classical Orbital Elements

6.1.1 Kepler's and Newton's Laws

In 1610, based on planetary observations by Tycho Brahe, Johannes Kepler formulated the empirical rules that describe how the planets move. Kepler's laws can be stated as follows [13]:

- Each planet moves in an ellipse with the Sun at one focus.
- 'Law of areas': the line between the Sun and planet sweeps out equal areas in equal amounts of time.
- 'Harmonic law': the ratio of the cube of the semi-major axis to the square of the period is the same for each planet.

Kepler's laws describe how the planets move, but not why. Isaac Newton realised that if any body is not moving in a straight line, some force must be acting on it to deflect it from a straight-line motion. In the case of the planets, the principal force is gravity, the force by which any mass attracts any other mass. Newton determined that the gravitational attraction between the Sun and a planet must be proportional to the mass of the Sun (m_1) and to the mass of the planet (m_2) – Newton's law of gravitation, 1687:

$$F_{12} = G\frac{m_1 m_2}{r^2} \tag{6-1}$$

with r being the distance between the two bodies and G the gravitational constant ($G = 6.672 \times 10^{-11}$ m³/s²kg).

His work showed that Kepler's laws apply to any situation in which a small body revolves around a much more massive body.

6.1.2 Classical Orbital Elements

Integration of Newton's law of gravitation gives the mathematical formulation of Kepler's laws and the motion of a spherical body around another spherical body, e.g. a spacecraft/satellite around the Earth (Figure 6.1), neglecting all other influences of gravitational forces, non-spherical shape, and the satellite's mass.

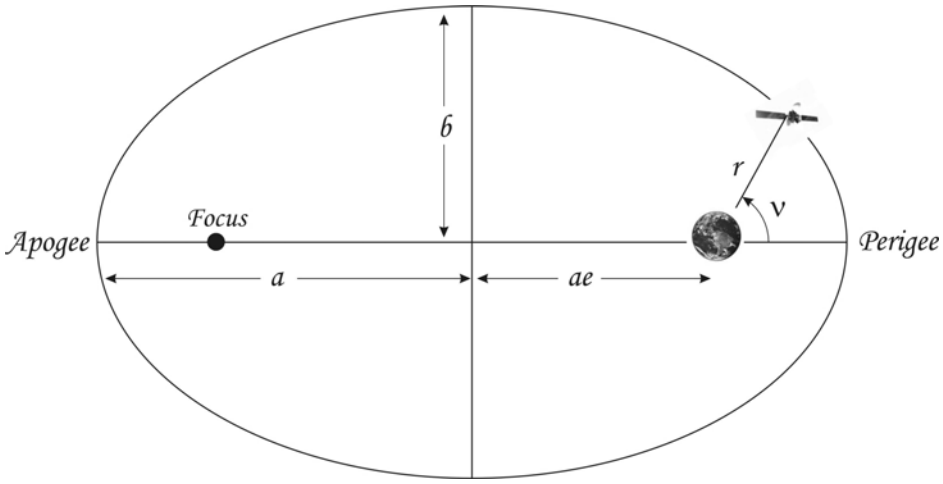

Figure 6.1: Elliptical motion of a satellite.

Kepler's first law can be stated as follows [4]:

$$r = \frac{p}{1 + e\cos\upsilon} \tag{6-2}$$

with ν being the true anomaly, the angle from perigee (closest point to Earth) to the satellite's position and

$$p = a\left(1 - e^2\right) \qquad e^2 = \frac{a^2 - b^2}{a^2} \tag{6-3} \quad (6\text{-}4)$$

with a for the semi-major axis, b for the semi-minor axis and e for the eccentricity of the orbit. Depending on the value of e ($e < 1$, $e = 1$, $e > 1$) the orbit becomes elliptical, parabolic or hyperbolic, respectively.

The velocity v of a satellite can be derived through the energy theorem:

$$v^2 = GM\left(\frac{2}{r} - \frac{1}{a}\right) \tag{6-5}$$

with M being the mass of the gravitating body. The parabolic velocity, also called escape velocity, for a certain body can be calculated by setting a to infinity (the satellite's orbit is not closed anymore and it leaves the body) and r to the body's radius. For the Earth (r = 6371 km, GM = 3.986 x 10^{11} km³/s²) the escape velocity is 11.2 km/s.

The values a and e describe the orbit size and shape; ν determines the body's position within the orbit and is the only orbital element which will change with time as the satellite moves around its orbit. Three more orbital elements are required to define the orientation of the orbit with respect to the central body (Figure 6.2, Table 6.1).

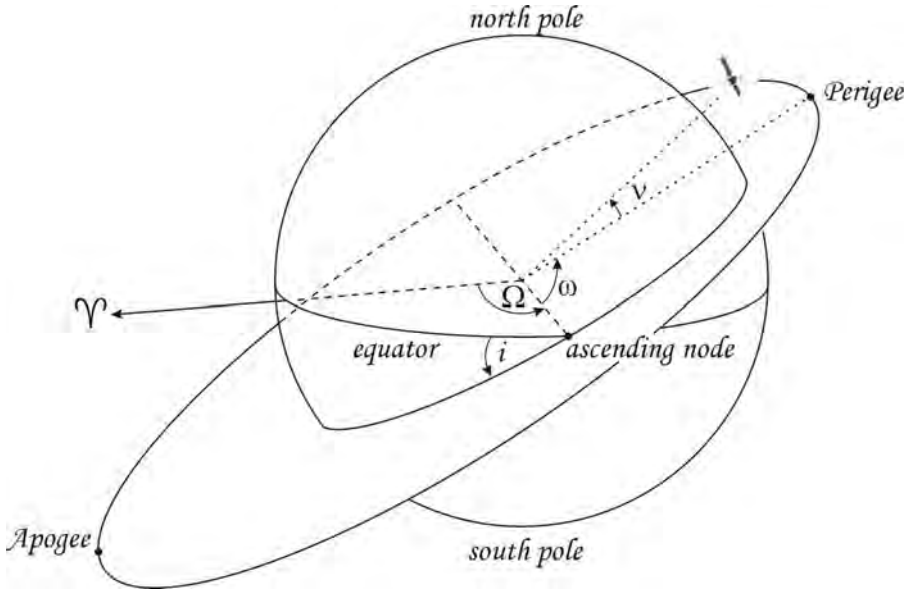

Figure 6.2: Classical orbital elements.

The inclination *i* of a satellite is defined as the angle between its orbital plane and the Earth's equatorial plane. The ascending node is the point where the satellite goes from below the equator (southern hemisphere) to above the equator (northern hemisphere). The longitude of the ascending node Ω describes the angle measured (eastward) in the equatorial plane between the vernal equinox direction and the ascending node. The vernal equinox Υ defines the intersection of the ecliptic plane with the equator where the Sun is located during the spring equinox and is crossing the equator from south to north. The argument of perigee ϖ is the angle measured in the direction of the satellite's motion from the ascending node to perigee [15].

The position vector of a spacecraft $\vec{r}_S$ as seen from the Earth centre can thus be formulated as:

$$\vec{r}_S = r \begin{pmatrix} \cos(\omega+\nu)\cos\Omega - \sin(\omega+\nu)\sin\Omega\cos i \\ \cos(\omega+\nu)\sin\Omega + \sin(\omega+\nu)\cos\Omega\cos i \\ \sin(\omega+\nu)\sin i \end{pmatrix} \tag{6-6}$$

element	*name*	*description*	*range of values*	*definition of …*
a	semi-major axis	orbital size	depends on conic section	form of orbit
e	eccentricity	orbital shape	0 for circle, $0 < e < 1$ for ellipse, $e = 1$ for parabola, $e > 1$ for hyperbola	
i	inclination	tilt, angle between the orbit plane and the equatorial plane	$0 \le i \le 180°$	orbital position
Ω	longitude of ascending node	swivel, angle from vernal equinox to ascending node	$0 \le \Omega \le 360°$	
ω	argument of perigee	angle from ascending node to perigee	$0 \le \omega \le 360°$	orientation of ellipse in orbital plane
ν	true anomaly	angle from perigee to satellite position	$0 \le \nu \le 360°$	

Table 6.1: Classical orbital elements and their description [15].

6.2 PERTURBATIONS

In reality there are no such simple bodies and motions as stated above. Each body in the solar system is non-spherical and is affected not only by the Sun but also by the planets, other smaller bodies and, with respect to an artificial body, by forces acting on the spacecraft itself.

In mathematical terms it is assumed that the body is moving in an elliptic orbit whose elements change at each instant. The variation of elements in time results e.g. in the regression of the nodes about the polar axis, in constantly changing inclinations, in variations in the size and shape of the ellipse [22]. If at a moment, called the instant of osculation, all disturbing forces were removed, the body would travel in an elliptical orbit described by the instantaneous or osculating elements. The perturbations are the differences between the Keplerian elements of the orbit at some starting epoch and those at the instant of osculation. They may be periodic (varying smoothly between limits) or secular (rending to change in a certain direction) and may be divided into two groups: gravitational and non-gravitational effects.

6.2.1 EXAMPLE I: SATELLITE IN EARTH ORBIT

The largest gravitational perturbations for low orbiting satellites are caused by the fact that the Earth is not spherical. These forces alter all orbital elements, specifically they change the longitude of the ascending node Ω and move the argument of perigee ω. By observing the perturbations certain gravitational parameters may be determined which in turn yield information on the shape and mass distribution of the Earth.

Of the non-gravitational perturbations the largest (in the case of low-flying satellites) is caused by the atmospheric drag, which takes energy away from the orbiting body in the form of friction on the satellite, causing a decrease of speed and consequently lowering of altitude [15].

Other perturbing forces are usually much smaller than the above mentioned but, depending on the required accuracy of the orbit predictions and the altitude of the spacecraft, satellite planners may have to anticipate their effects. These forces include third-body effects (due to Moon, Sun, planets, etc. which can perturb orbits at high altitudes), different electromagnetic effects, solar radiation pressure (which can cause long-term orbit perturbations and unwanted rotation of the satellite), and effects caused by the satellite itself (e.g. thrusters firings).

6.2.2 EXAMPLE II: SPACECRAFT WITHIN THE JOVIAN SYSTEM

In other words it could be said that the perturbations cause an acceleration (positive or negative) of the spacecraft and consequently changing its orbit. A programme used at JPL for the determination of GALILEO's and other interplanetary spacecraft's trajectory, called the Double-Precision Orbit Determination Program or DPODP (chapter 7.3.2), takes the following acceleration forces, with respect to the trajectory, into account [21]:

- all bodies of the solar system, treated as point masses
- perturbative general relativity
- oblateness of Jupiter and a nearby moon
- solar radiation pressure
- small forces originating in the spacecraft, such as from operation of the attitude control system and from gas leaks
- firing of thrusters (motor burn)

If the position of a spacecraft is known at any time through e.g. tracking techniques (chapter 7), the extent of the perturbations can be calculated. On the other hand, when using

the information of the gravitational perturbations from a nearby planetary body (chapter 11.4.3), interior models of the gravitating body can be derived as well.

6.3 SPACECRAFT TRAJECTORY APPROXIMATION

As the equations of motion cannot be solved analytically if more than two bodies are involved, and the various perturbations change the orbit of a planetary body or spacecraft at any time, it is necessary to calculate trajectory sections through numerical integration techniques. A very common method of numerically integrating differential equations is the fourth-order Runge-Kutta or midpoint method.

The Runge-Kutta-Method takes a value at a starting point, e.g. $\vec{x}(t_i)$, and calculates an approximation at a brief time later, $\vec{x}(t_{i+1})$. It uses a weighted average of approximated values at several times within the interval (Figure 6.3). In each step the function is evaluated four times – once at the initial point, twice at trial midpoints, and once at a trial endpoint. From these derivatives the final function value (shown as a filled dot) is calculated.

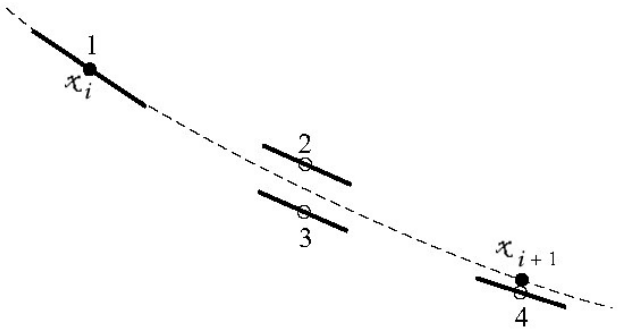

Figure 6.3: Fourth-order Runge-Kutta method.

The formula is given by [18]:

$$\vec{x}(t_{i+1}) = \vec{x}(t_i) + \frac{1}{6}\left(\vec{k}_1 + 2\vec{k}_2 + 2\vec{k}_3 + \vec{k}_4\right) \tag{6-7}$$

with (*h* being the interval and $f(t,x)$ the differential equation)

$$\begin{aligned}
\vec{k}_1 &= h \cdot f\left(t_i, \vec{x}(t_i)\right) \\
\vec{k}_2 &= h \cdot f\left(t_i + \frac{h}{2}, \vec{x}(t_i) + \frac{\vec{k}_1}{2}\right) \\
\vec{k}_3 &= h \cdot f\left(t_i + \frac{h}{2}, \vec{x}(t_i) + \frac{\vec{k}_2}{2}\right) \\
\vec{k}_4 &= h \cdot f\left(t_i + h, \vec{x}(t_i) + \vec{k}_3\right)
\end{aligned} \tag{6-8}$$

This method is reasonable simple and robust and gives good accuracy if a small realistic interval is used. Within the frame of this work the trajectory of GALILEO around closest approach to Amalthea has been calculated by means of the Runge-Kutta-Method based on the equations of motion (chapter 12.3).

6.4 FLYBY GEOMETRIES AND TRAJECTORIES

Each space mission is a unique project. Depending on the objective of the mission, the scientific observations and other constraints (e.g. fuel consumption and data relay back to Earth), not only the structure of the satellites is designed but also the orbit of the spacecraft. To put a spacecraft into an interplanetary transfer trajectory is an extension of the basic orbital transfer problem and much more complicated, because four bodies (the spacecraft, Earth, Sun, and the target planet) are involved. To simplify the problem the trajectory is separated into regions that are solved independently and then put together to get a final solution (Figure 6.4).

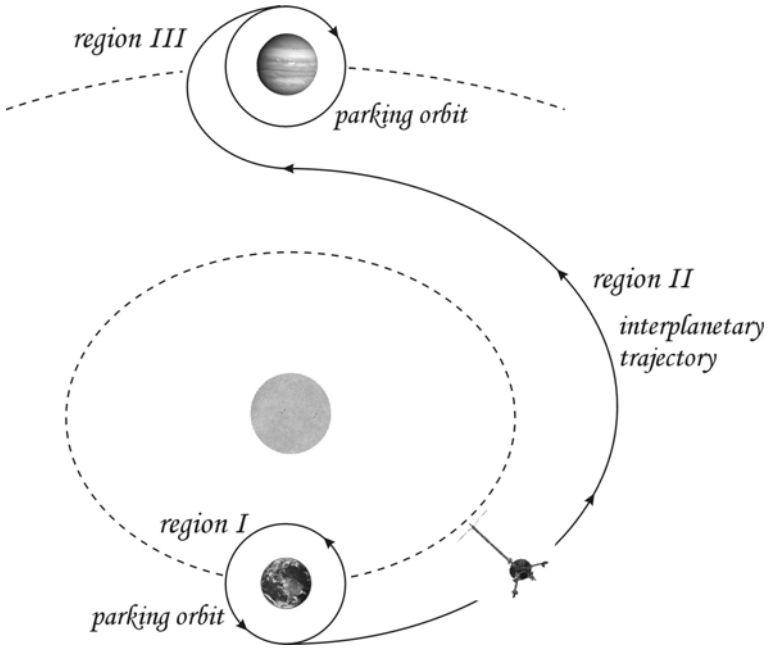

Figure 6.4: Gravitational forces acting on an interplanetary spacecraft.

After the launch of a spacecraft and its release from the rocket it is generally placed into a parking orbit around the Earth. To set the space probe on its trip to another body in the solar system, or any other point, its velocity and thus energy needs to be changed, usually through impulsive burns of rocket thrusters. Before further actions are taken for the spacecraft's scientific operation, it is placed into another parking orbit at the target planet [15].

6.4.1 GRAVITY ASSIST

To reach other bodies in the solar system using this so called 'Hohmann Transfer manoeuvres', a tremendous amount of rocket propellant is required, which significantly increases the mission's cost. 'Free' velocity changes can be obtained through gravity assist techniques where the planet's gravitational field and orbital velocity are used to catapult the spacecraft, changing its velocity (in magnitude and direction) and its plane if necessary.

After leaving the Earth's gravity field the space probe is sent into an elliptical orbit around the Sun heading toward the destination planet. The planet does not interact with the spacecraft until it approaches close enough for the planet's gravity to be stronger than that of the Sun's. This region is called the 'sphere of influence' (Figure 6.5).

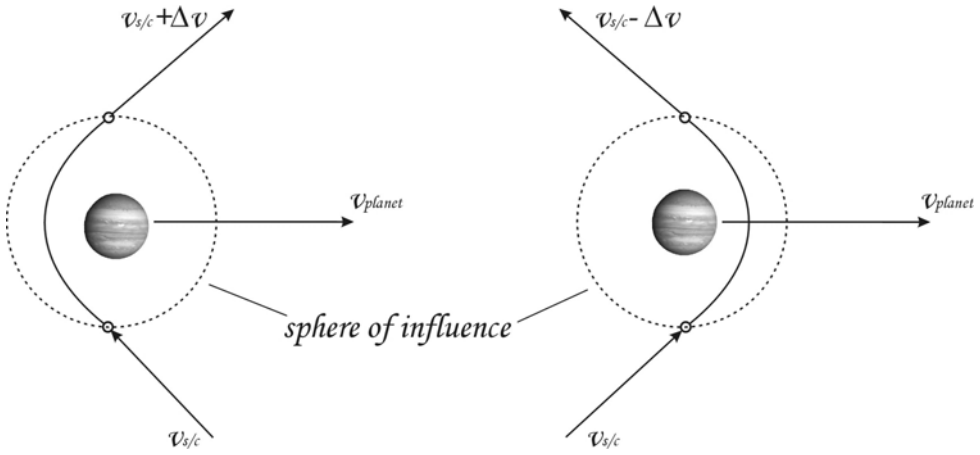

Figure 6.5: Planet's sphere of influence and spacecraft (s/c) velocity change.

Near the planet the path of the spacecraft is a hyperbolic orbit rather than an elliptic one, and its centre of motion is the planet (Figure 6.6). The hyperbolic orbit is due to the fact that the spacecraft's velocity is higher than the escape velocity of the planet. Once the probe leaves the planet's sphere of influence, it will again be in an elliptical orbit around the Sun – but different from the one before [27].

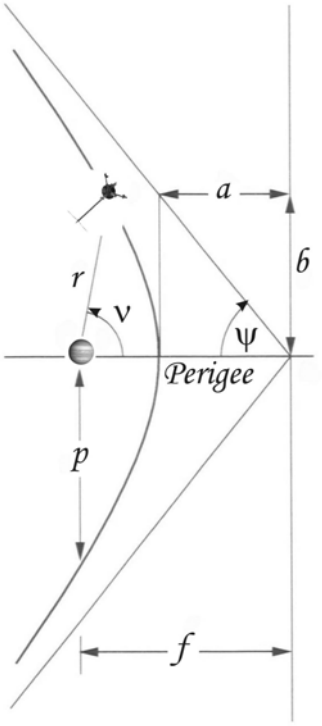

$$p = a\left(e^2 - 1\right) \tag{6-9}$$

$$e^2 = \frac{a^2 + b^2}{a^2} \tag{6-10}$$

$$\psi = \arccos\left(\frac{1}{e}\right) \tag{6-11}$$

$$v = \sqrt{\frac{GM}{p}\left(3 + 2e\cos\nu - e^2\right)} \tag{6-12}$$

Figure 6.6: Hyperbolic orbit and formulas.

Depending on the path of the spacecraft, passing behind or in front of the planet with respect to its motion around the Sun, it is pulled in the direction of the planet's motion and thus gains velocity with respect to the Sun or, respectively, it is pulled in the opposite direction, slowing the spacecraft down and lowering its orbit (Figure 6.5). To give an example for the magnitude of the velocity change Δv, consider Voyager 2 on its way to explore the outer solar system. In order to move outward and exceed the solar system escape velocity, the spacecraft gained up to 20 km/s speed during the various planet flybys (Figure 6.7).

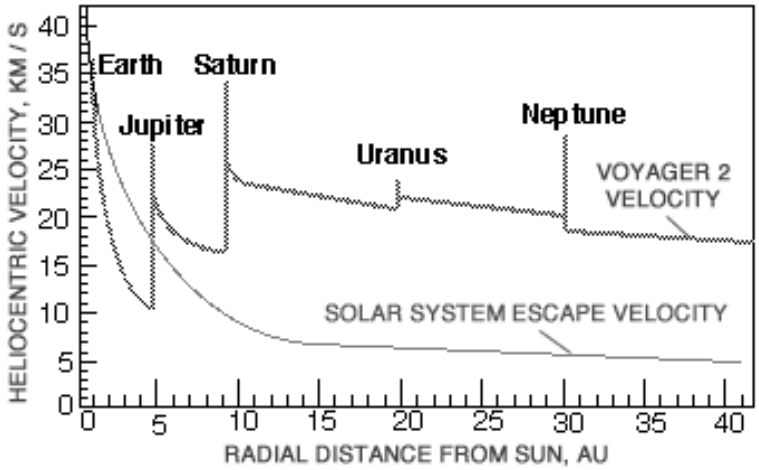

Figure 6.7: Voyager 2 gravity-assist velocity changes [Courtesy Steve Matousek, NASA/JPL].

6.4.2 GALILEO'S TRAJECTORY

The gravity-assist-technique was also used with GALILEO, which trajectory consisted of a Venus flyby (Δv = 2.0 km/s) and two Earth flybys (Δv_1 = 5.2 km/s, Δv_2 = 3.7 km/s) before it could reach its final destination Jupiter (Figure 6.8).

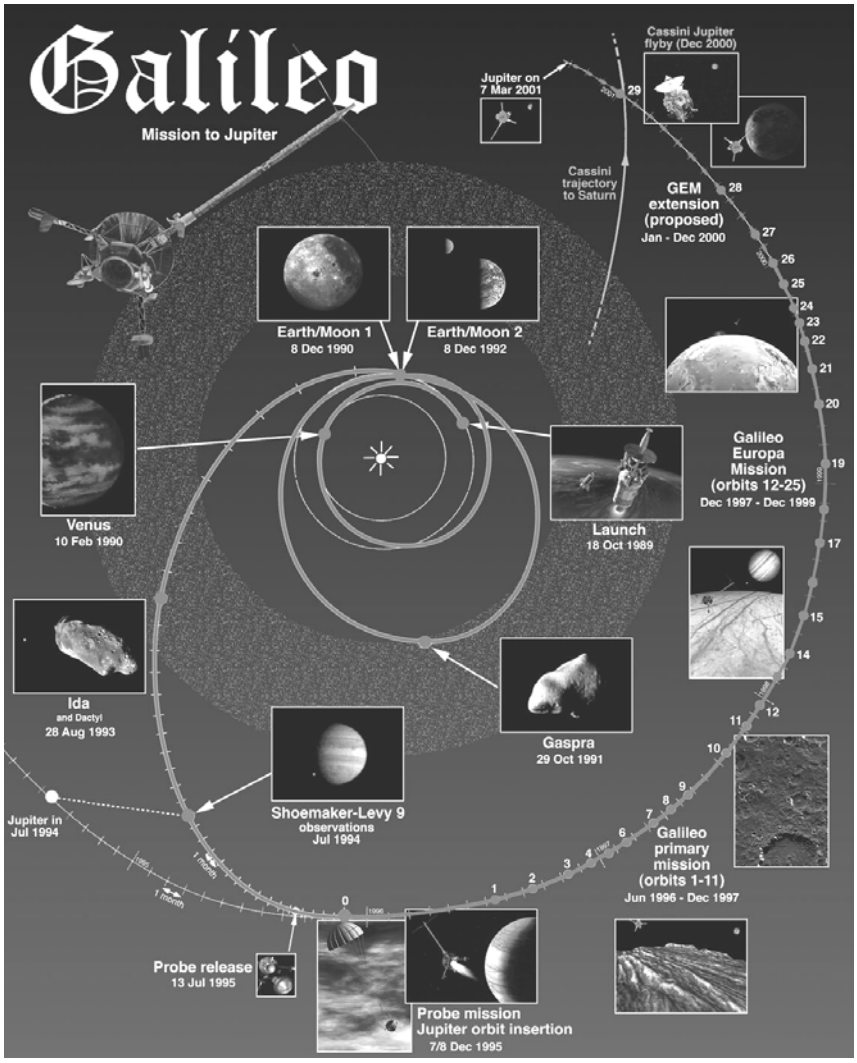

Figure 6.8: Galileo's trajectory until 2001 [Courtesy NASA/JPL-Caltech].

The same principle applies within the Jovian system, where Jupiter is the main influence of gravity and its moons can be used as gravity assists. In the case of GALILEO, the gravity of the massive Galilean moons was used to modify the orbiter's course during each highly elliptical revolution about Jupiter. This simultaneously sent the spacecraft towards the next encounter and provided extremely close, targeted approaches to the satellites for scientific measurements, called a 'tour'. While it is relatively easy to design a tour to satisfy any individual science requirement, it is difficult to design a single tour that suits all the science requirements, because the trajectories needed to satisfy individual science requirements tend to be dissimilar. Therefore, strategies are developed to maximise the satellite tour science and different encounters are often dedicated to specific science investigations, e.g. GALILEO's encounter with Amalthea (chapter 8).

7 RADIO SCIENCE FOR ORBIT AND GRAVITY FIELD DETERMINATION

The field of Radio Science improves our knowledge of the solar system through radio frequency experiments performed between a spacecraft and an Earth-based radio science system. These experiments allow scientists to characterise planetary atmospheres and planetary surfaces, confirm general relativity, search for gravitational waves, characterise planetary gravity, and determine the mass of the planets, moons and asteroids. In the case of GALILEO's encounter with Jupiter's moon Amalthea the flyby was dedicated to the latter two.

7.1 SPACECRAFT COMMUNICATION AND TRACKING

A space mission's communications network relates to the exchange of command and engineering data between spacecraft and ground controllers, as well as the processing and transmission of data from the payload to the users. It contains three elements: the satellite as the space- borne part of the system, the ground stations with Earth-based antennas and receivers, and the control centre that controls the satellite and all other elements in the network (Figure 7.1). In some cases an additional satellite might be integrated, which links the primary satellite with the ground stations [15].

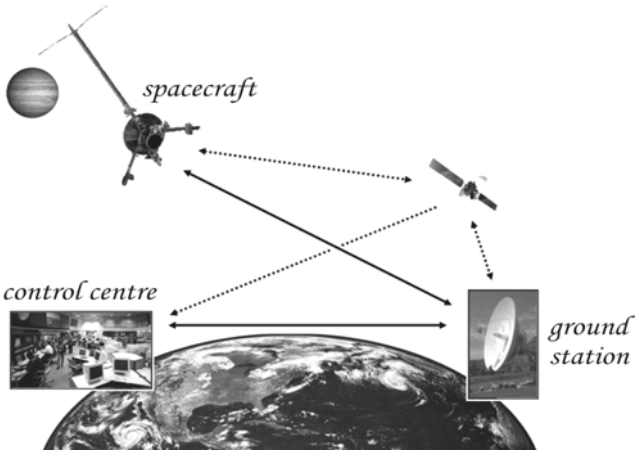

Figure 7.1: Communications network.

Communication across space is based on radio waves. In principle, a ground station broadcasts a carrier signal at some specific allocated frequency. The message being sent is superimposed on top of the carrier signal using some type of modulation scheme. The radio signal travels out from the ground station's antenna and is received by the antenna on the satellite. The same principle applies for a spacecraft generated signal.

7.1.1 THE DEEP SPACE NETWORK

Managed by JPL, the Deep Space Network (DSN) provides radio communications for all of NASA's interplanetary spacecraft and for some Earth-orbiting spacecraft in high-Earth orbits, and a selected group of satellites in low-Earth orbits. It is also utilised for radio astronomy and radar observations of the solar system and universe [43].

The current structure of the DSN consists of three Deep Space Communications Complexes, located around the world, approximately 120 degrees apart in longitude to compensate for the Earth's daily rotation and therefore providing continuous communications to the spacecraft. Situated near Canberra (Australia), Madrid (Spain), and Barstow (California), far away from

heavily populated areas, they consist of several deep space stations equipped with large parabolic reflector antennas (Figure 7.2) and ultra-sensitive receiving systems to detect the weak signals of the remote spacecraft. For the GALILEO mission arraying (the combination of signals from more than one antenna) was utilised to get higher data rates from the low-gain spacecraft antenna, necessitated by difficulties with the spacecraft's high-gain antenna (chapter 5.4).

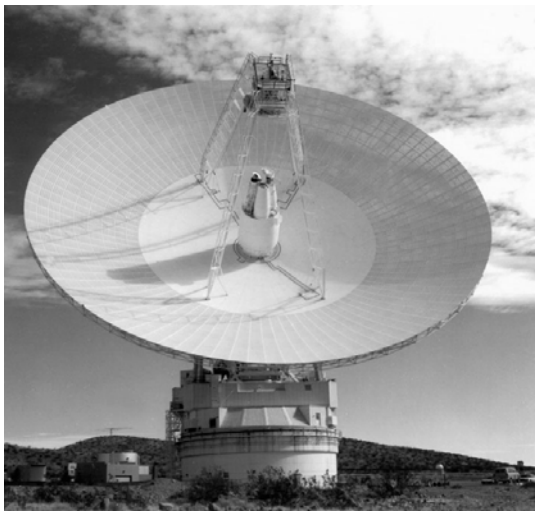

Figure 7.2: Front view of the 70m antenna at Goldstone, California/USA [Courtesy NASA/JPL-Caltech].

This sophisticated Earth-based communications system is an essential component for controlling a spacecraft's operation modes, loading and reprogramming its computers, navigating it to its destination, and sending scientific data back to Earth. The scientific data are then transferred via landlines, terrestrial microwave links, or communications satellites to the Deep Space Operations Center at JPL. Here the raw spacecraft and ground system data are processed into usable products for real-time delivery to mission control operators and mission scientist and engineers.

7.2 DOPPLER AND RANGING MEASUREMENTS

7.2.1 THE DOPPLER EFFECT

The Doppler effect or Doppler shift, named after the Austrian physicist Christian Doppler (1803-1853), denotes the difference between the frequency/wavelength of the radiation received at an observing point and the frequency/wavelength of the radiation at its source, when observer and source are moving with respect to each other [26]. For simplicity only the case where observer and source are moving along a straight line is considered. Motion of the radiation source along the line of sight away from the observer causes an increase of the wavelengths (red-shifts), and motion along the line of sight toward the observer causes a decrease of the wavelengths (blue-shifts). The wavelength shift ($\Delta\lambda$) due to the Doppler effect is directly proportional to the velocity of recession or approach (v), as long as the relative velocity is much less than the velocity of light (c):

$$\Delta\lambda = \frac{\lambda_0}{c} v \tag{7-1}$$

where λ_0 is the wavelength of the radiation produced by the source.

Observation techniques based on the Doppler principle are widely used in science and technology for the determination of velocities. In practice, the Doppler shift is determined from the difference between the transmitted (f_T) and the received frequency (f_R) within a given time interval (T), where the time of observation (t_O) is associated with the middle of the interval. In addition, the cycle count between the two times is normalised by the length of the interval. Therefore, the actual Doppler observable (F), that is available for further calculations, is given by:

$$F(t_O) = \frac{f_T}{T} \int_{t_O - \frac{1}{2}T}^{t_O + \frac{1}{2}T} \left(1 - \frac{f_R}{f_T}\right) dt_O \qquad (7\text{-}2)$$

The representation of the Doppler observable for purposes of velocity changes of a spacecraft, and hence orbital elements, requires [1]:

- a knowledge of the transmitter frequency
- the count time and the observation time
- a mathematical model for the integral as a function of the relative motions of the Earth and spacecraft and the propagation effects through particulate matter, which will advance the phase of a radio signal (e.g. Earth's atmosphere and ionosphere, interplanetary medium)

The acceleration of the spacecraft, and consequently the acceleration due to gravitational forces (e.g. nearby planetary bodies), is obtained through the variation of the Doppler observable with time. Based on these measurements the gravitational potential, given through the moments of gravitation (chapter 11.4.3), of a planetary body can be derived and thus interior structure models designed.

In general, different techniques can be used to derive the Doppler observables:

- 1-way Doppler measurements: an electromagnetic signal is transmitted continuously from the spacecraft and received by the tracking station on Earth
- 2-way Doppler data: the signal is transmitted continuously from a tracking station on Earth, received and retransmitted by the spacecraft, and received continuously by the same tracking station
- 3-way Doppler observable: as the 2-way but the signal is received by a different tracking station

As the reference and received frequency for the 2-way Doppler data are derived from the same atomic frequency standard, the 2-way Doppler gives the most accurate measure of the Doppler frequency shift and thus the range rate from the tracking station to the spacecraft.

7.2.2 SPACECRAFT RANGING

To obtain range data from a spacecraft, a phase modulation is placed on the signal being used for the Doppler data. This modulation, which is called the ranging code, is carried to the spacecraft and back to Earth at a frequency equal to the transmitter frequency f_T on the up leg of the transmission and at a frequency on the down leg that is slightly Doppler-shifted by the motion of the spacecraft. When the phase shift is such that the correlation of the received and transmitted codes is at a maximum, the number of cycles of phase shift yields the time delay between the transmitted and received signals.

This time delay constitutes the range observable (R):

$$R = c\left[t_3(ST) - t_1(ST)\right] \tag{7-3}$$

where $t_3(ST)$ and $t_1(ST)$ are the reception and transmission times, respectively, recorded on the station (ST) clock [20].

A ranging measurement will be a function of the relative positions of the Earth and the spacecraft, as well as a function of propagation effects of the signal through charged and neutral particles. In contrast to the Doppler signal the scattering from free electrons will retard the ranging signal.

7.3 ORBIT AND GRAVITY FIELD DETERMINATION

For the determination of precision orbits of interplanetary spacecraft, radar and optical sightings from Earth-based stations can be used, or radar and optical sightings of celestial bodies can be made from the spacecraft itself. Accurate spacecraft orbits on the other hand are required in order to determine the gravity fields of the planets and their satellites.

With respect to the GALILEO mission, in general only ground-based data was used for the radio science experiments, in particular two-way coherent range and Doppler data of the DSN. Because of the failure of the high-gain antenna, the investigations had to be carried out with the radio S-band (Earth-spacecraft uplink: 2215 MHz or 14.17 cm wavelength [25]) using the low-gain antenna of the satellite.

7.3.1 ACCURACY

To represent the spacecraft data it is necessary to carry at least as many digits in the numerical computation as are required to achieve full accuracy in the data themselves. In the case of Doppler data, the limiting accuracy is determined by the stability of the frequency standard, which is stated by the Allan variance (σ_y) [36]. This is a widely used statistic for assessing the performance of oscillators and clocks over a specified time interval, meaning how well an oscillator maintains a particular frequency or how well a clock keeps time.

For two-way Doppler data the relation between the range rate $\dot{\rho}$ and the frequency shift Δf is approximately [1]:

$$\frac{2\dot{\rho}}{c} \approx \frac{\Delta f}{f} \tag{7-4}$$

Thus, the error of the range rate for an appropriate interval of time of several seconds, over which the standard deviation (σ_f) of the frequency standard is clearly defined, is given by

$$\sigma_{\dot{\rho}} = \frac{1}{2} c \sigma_y = \frac{1}{2} c \left(\frac{\sigma_f}{f} \right) \tag{7-5}$$

The DNS's frequency and timing system is based on hydrogen-maser frequency standards; therefore the instrumental error (or Allan variation) in measuring the Doppler shift will be between 10^{-12} and 10^{-15} for the S-Band, depending on the length of observation. The corresponding measurement of velocity will be accurate in the range of $\pm 10^{-4}$ to $\pm 10^{-7}$ m/s, and ± 0.1 m for the range observable.

The basic limitations on the accuracy of the above mentioned computed observables are the inaccuracies in the troposphere and ionosphere corrections, as well as space plasma corrections, which can deteriorate the accuracy to a factor of 10.

7.3.2 DATA EVALUATION

At JPL the Double-Precise Orbit Determination Program (DPODP) is used to determine values of the parameters that specify the spacecraft trajectory for planetary missions, both for real-time and post-flight reduction of the tracking data. The DPODP differentially corrects a priori estimates of injection parameters, physical constants, manoeuvre parameters, and station locations to minimise the sum of weighted squares of residual errors between observed and computed quantities [21]. The programme was developed from 1964 to 1968 and is still in use for various spacecraft missions, such as e.g. GALILEO.

The parameters whose values may be estimated by the DPODP through least square techniques are e.g.:

- parameters that affect the relative position and velocity of the Sun, planets and the Moon (gravitational constants GM, osculating orbital elements, etc.)
- the harmonic coefficients J_n, C_{nm}, S_{nm} which describe the gravitational field of a body
- parameters affecting the acceleration of the spacecraft due to solar radiation pressure
- coefficients for small acceleration acting along each spacecraft axis (due to gas leaks and small forces arising from operation of the attitude control system)
- parameters affecting the transformation from universal time to ephemeris time due to e.g. relativistic effects
- station parameters
- spacecraft transmitter frequency for 1-way Doppler

Given the a priori estimate of the parameter vector q, the programme integrates the spacecraft acceleration using numerical integration methods to give position and velocity at any desired time. Using the spacecraft ephemeris along with the pre-computed ephemeris for the other bodies within the solar system, and the parameter vector q, the programme computes values for each observed quantity (normally Doppler shift, range, or angles) and forms the observed minus computed residuals.

In addition to integrating the acceleration of the spacecraft to obtain the spacecraft ephemeris, the programme integrates the partial derivative of the spacecraft acceleration with respect to the parameter vector q to give the partial derivative of the spacecraft state vector and furthermore the partial derivative of each computed observable. In combination with the residuals, the weights applied to each residual, the a priori parameter vector and its covariance matrix, the programme computes the differential correction Δq to the parameter vector, which serves as input for a new integration. This process is repeated until convergence is obtained and the sum of weighted squares of residual errors between observed and computed quantities is minimised.

These techniques and their mathematical formulation are discussed in detail by Moyer [21].

8 GALILEO AMALTHEA FLYBY

GALILEO's last and final flyby of its mission, a close encounter with Jupiter's small inner moon Amalthea, took place on November 5, 2002. The following chapter explains the planned scientific observations with respect to the gravity field of Amalthea, the problems that occurred during the flyby and the efforts of the radio science team to recover some of the data.

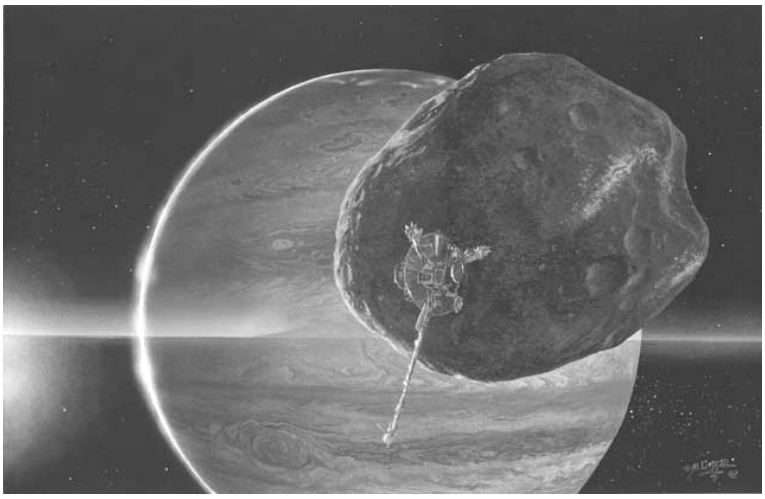

Figure 8.1: Artist impression of GALILEO's flyby at Amalthea [Courtesy Michael W. Carroll].

8.1 FLYBY GEOMETRY AND SCIENCE INVESTIGATIONS

8.1.1 PLANNED FLYBY

The flyby of Amalthea was mainly dedicated to the observation of its gravity field, thus the orbit designed to fulfil this objective. In order to get a strong Doppler signal, which includes information about the quadrupole moments of Amalthea's gravity field (chapter 11.4.3), it was anticipated for the flyby to occur approximately within the Jupiter-Amalthea equatorial plane and the Earth line of sight (which would result almost above the longest axis of the moon).

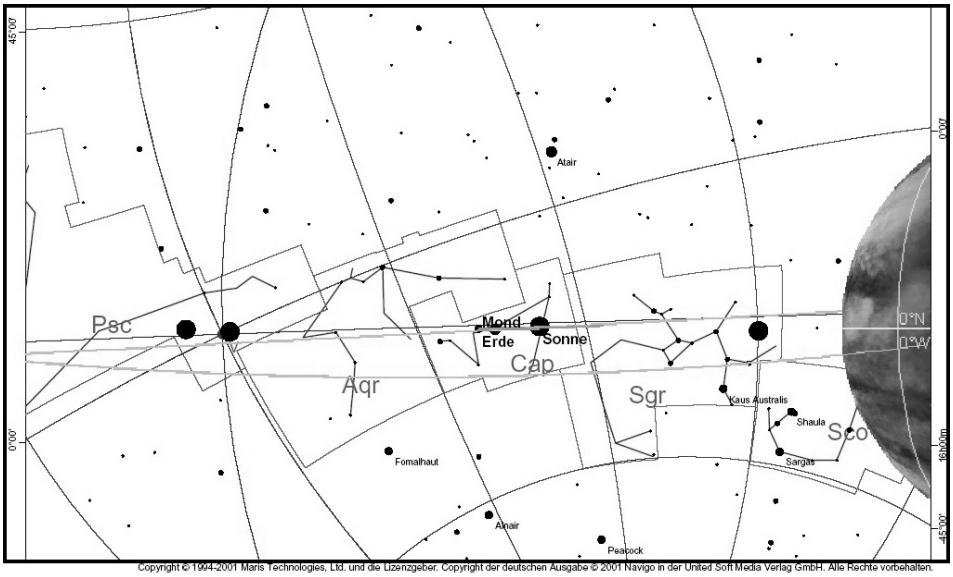

Figure 8.2: The solar system as seen from Amalthea on November 5, 2002, 6:18 UTC.

Because of Amalthea's small dimensions, and thus mass, and the spacecraft's high velocity, it has not been expected to get a detectable signal much outside of one minute about closest approach [37]. The data sample interval therefore needed to be high – one point per second. With an estimated Allen variation (σ_y) of 10^{-12} over this short period, the Doppler error for the 2-way Doppler signal (7-5), and thus measurement accuracy, amounts to ±0.15 mm/s.

The acceleration noise

$$\sigma_a = \frac{1}{2} c \frac{\sigma_y}{T} \tag{8-1}$$

per sample interval (T = 1 second) totals ±0.15 mm/s² and the total acceleration error floor over 60 seconds is ±2.5 x 10^{-3} mm/s².

Derived from equation (11-47), chapter 11.4.3, the axis a, b, c of Amalthea, and the flyby radius r the maximum signal level a_2 for the expected quadrupole moments of gravitation can be plotted (Figure 8.3):

$$a_2 = \frac{3}{10} \frac{GM}{r^6} \left[x^2 \left(2a^2 - b^2 - c^2 \right) + y^2 \left(-a^2 + 2b^2 - c^2 \right) + z^2 \left(-a^2 - b^2 + 2c^2 \right) \right] \tag{8-2}$$

Considering Amalthea's figure and values for a polar flyby ($x = y = 0$), the flyby would have had to occur below an altitude (= r - a) of ~800 km to get any gravity signal, but unfortunately the signal is buried in the data noise above an altitude of ~220 km. A flyby altitude of e.g. 380 km would have given already a gravity error of about 10%, higher altitudes deteriorating the results of the experiment even more. The values for an equatorial flyby ($y = z = 0$) are slightly better and considering the gravity errors, a flyby altitude (or respectively radius at closest approach) of ~150 km (~280 km, respectively) has been anticipated.

For completeness it should be stated that no range data was available for the experiment.

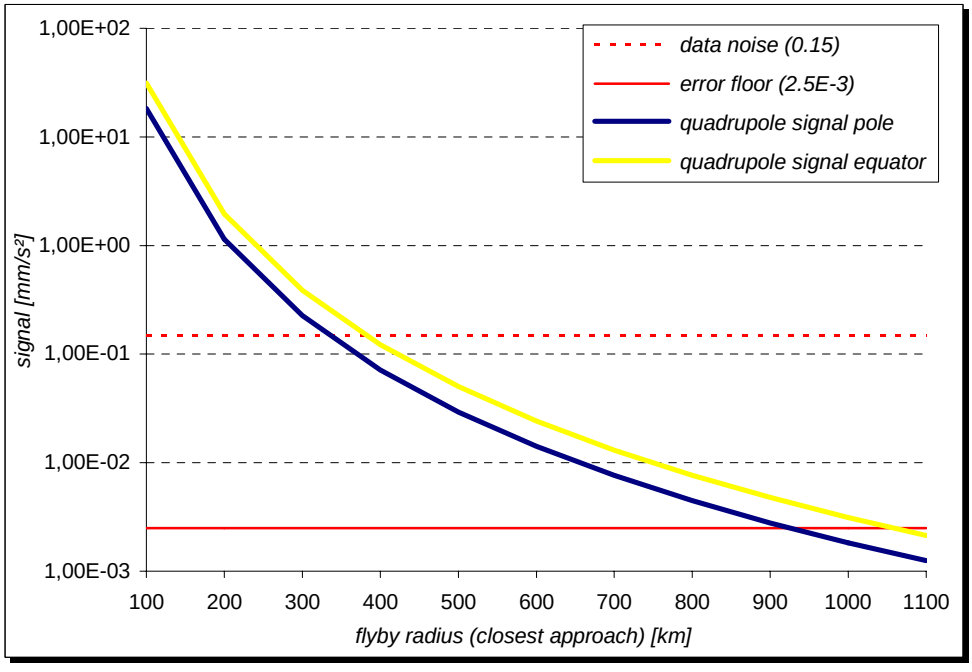

Figure 8.3: Maximum signal level for expected quadrupole gravity moments.

8.1.2 FLYBY SEQUENCE

The science observation sequence for GALILEO's final satellite encounter began on Monday, October 21, 2002, and lasted for three weeks. In addition to the gravity field experiments the following instruments participated in data collection for Jupiter's environment: the Dust Detector, the Energetic Particle Detector, the Heavy Ion Counter, the Magnetometer, the Plasma Subsystem and the Plasma Wave Subsystem. All other instruments, unfortunately including the SSI camera for obtaining optical images of Amalthea, had to be shut down because of Jupiter's immense radiation [38].

Figure 8.4: GALILEO's position (as seen from the north, direction of the sun points up) and Jupiter (as seen from the spacecraft) about a week before the flyby [Courtesy NASA/JPL-Caltech].

At 9:02 pm UTC, November 4, 2002, 10 hours before the closest approach, the Radio Science team began the experiment to measure the gravity field of Amalthea, which should have lasted 20 hours. This long period of observation would have given enough information about the moon's gravitational tug on GALILEO and thus the determination of the mass and the gravity field of Amalthea. For more details on all of the planned science observations and timeline of the encounter refer to Appendix B.

Figure 8.5: GALILEO's position (as seen from the north, direction of the sun points up) and Jupiter (as seen from the spacecraft) shortly before closest approach [Courtesy NASA/JPL-Caltech].

At 6:19:45 a.m. UTC, November 5, 2002, GALILEO reached its closest point to Amalthea, attaining a speed of 18.4 km/s with respect to the moon. At that time, GALILEO's radio signals took 44 minutes to travel between the spacecraft and Earth.

8.2 PROBLEMS AND SOLUTIONS

About five hours to closest approach it was anticipated to switch radio transmission from 1-way Doppler mode to 2-way Doppler to provide continuous coverage for the gravity measurements. Unfortunately the radio receiver on board GALILEO failed to phase lock to the uplink radio carrier transmitted by the DSN tracking station near Madrid, Spain, and therefore could not send back the signal. This failure was caused by an improper carrier frequency, which was outside the bandwidth of the spacecraft's receiver. As GALILEO is moving very fast near Jupiter, it is difficult to predict the Doppler-shifted frequency the spacecraft will receive. The prediction that was made was just not good enough for the 20-year-old receiver, which has been exposed to Jupiter's radiation more than four times the radiation dosage it was designed to take [2].

However, it was possible to receive 1-way Doppler data, generated from the spacecraft's crystal oscillator. Unfortunately it does not have sufficient accuracy to serve as a standard for precise Doppler and range transmissions and thus the gravity field of Amalthea cannot be determined from it alone. Nevertheless, the combination of both pre and post encounter 2-way Doppler data, attained a couple of days before and a day after encounter, in addition to the 1-way data can be used to derive at least the mass of the moon to a certain degree of precision.

8.2.1 ACTUAL DATA FROM THE FLYBY

The yearlong experience of the JPL Radio Science team enabled the scientists to analyse and interpret the Doppler data with means of the DPODP (chapter 7.3) and derive a mass estimation for Amalthea of $M = 2.083 \times 10^{18}$ kg ($GM = 1.39 \pm 0.1 \times 10^{8}$ m³/s² [16]). In combination with the volume of the moon (chapter 4.3) a mean density of $\rho_m = 860 \pm 60$ kg/m³ can be determined. This low density was unexpected for most Jupiter system models inside Io's orbit (chapter 4.4). In order to assess the material (or mineral) density of the body, a possible range of porosity Φ needs to be estimated (4-1). Because of Amalthea's shape it is unlikely that the moon consists solely of ice with $\Phi \sim 0$. The most likely range lies between $\Phi \sim 0.5$ with a low density rock or rock/ice mixture and $\Phi \sim 0.7$ with high density rock or rock/ice combination. Both assumptions indicate that Amalthea is probably a rubble pile with many volatile, icy and empty components. In contrast to the two accretion scenarios mentioned in chapter 4.4 there could also be the possibility that the rings and Amalthea formed much later in a different environment from the Galilean satellites, which generates difficulties for all theoretical modellers of the Jovian satellite formation at the moment, if the Amalthea results are correct [40].

In the frame of this work, these values have been used for the development of interior models and gravity field of Amalthea and further evaluations (chapter 13 and 14).

The various spacecraft data at closest approach with respect to the trajectory can be found in Appendix C. The actual flyby geometry is shown in Figure 8.6; the radius of closest approach (c/a) amounted to 254853.910 m*. The spacecraft's trajectory lies nearly parallel to Amalthea's longest axis, but approximately 200 km south of the Jupiter-Amalthea equatorial plane. With respect to the geometry of the trajectory the flyby would have been quite optimal for the gravity field experiment (chapter 14.2), if not for the data itself.

---

* Results from the latest JPL analysis show a flyby radius of 233.3 km (Anderson, J.D., et al: *Amalthea's Density is Less Than the Density of Water*, in preparation).

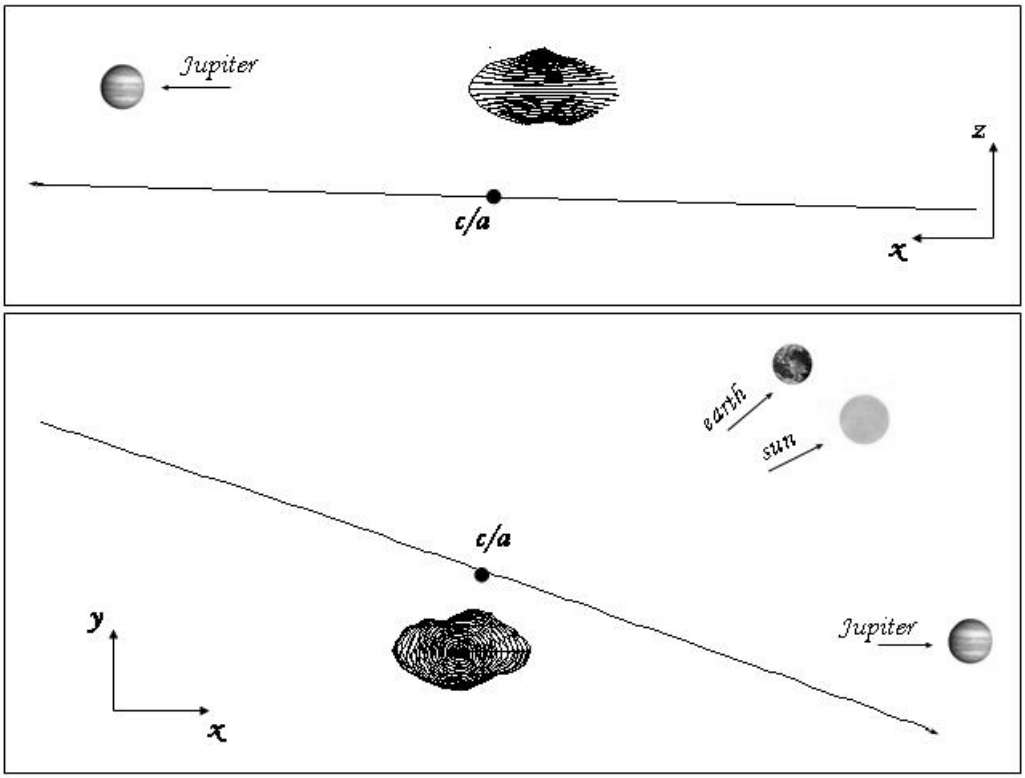

Figure 8.6: Galileo flyby geometry.

For completeness it should be stated that GALILEO placed itself in a standby precautionary mode after its closest approach to Amalthea, caused by the intense radiation of Jupiter. No further science investigations could be made, but the scientists where able to restore some of the gathered data and could make sure that the spacecraft was in good condition and on its right trajectory for the final impact on Jupiter on September 21, 2003.

Part III
Amalthea Models:
Preparatory Derivations

9 GEOMETRY OF A PLANETARY BODY

Although for a first order approximation spherical symmetry of planets and large moons can be assumed, in reality, a planetary body departs from that because of e.g. oblateness caused by body rotation, and asymmetric mass distribution. In order to get a more precise description of planetary bodies either a spheroid or general (triaxial) ellipsoid is applied. In some cases (e.g. small irregular objects) even an ellipsoidal approach is not sufficient and the shape of the body needs to be implemented. The following chapter gives the mathematical formulation of ellipsoidal equations with respect to planetary bodies.

9.1 CURVILINEAR COORDINATES

Sometimes it is necessary, or convenient, to derive various physical laws or solve problems in coordinates other than rectangular (Cartesian) coordinates. In Cartesian coordinates, the position of a point *P* is determined by the three coordinates *x, y, z,* which can be expressed through three new generalised coordinates u_1, u_2, u_3, called curvilinear coordinates (Figure 9.1):

$$\begin{aligned} x &= x(u_1,u_2,u_3) \\ y &= y(u_1,u_2,u_3) \\ z &= z(u_1,u_2,u_3) \end{aligned} \qquad \text{and conversely} \qquad \begin{aligned} u_1 &= u_1(x,y,z) \\ u_2 &= u_2(x,y,z) \\ u_3 &= u_3(x,y,z) \end{aligned} \tag{9-1}$$

In general, only orthogonal curvilinear coordinate systems, in which the three coordinate surfaces intersect at right angles, are of interest.

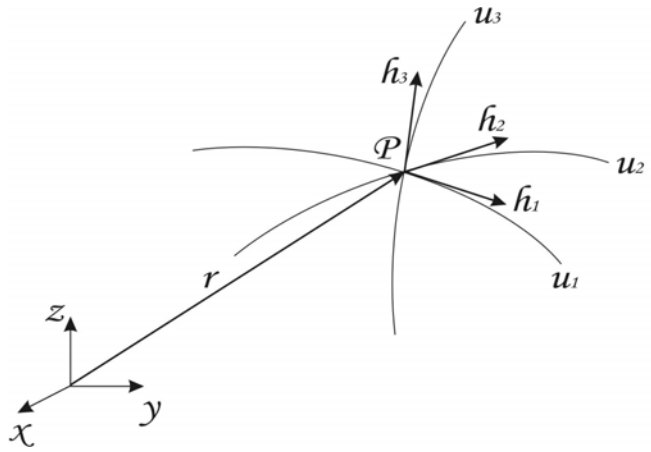

Figure 9.1: Curvilinear coordinates u_1, u_2, u_3.

Transforming the radius vector $\vec{r} = \vec{r}(x,y,z)$ to $\vec{r} = \vec{r}(u_1,u_2,u_3)$, and forming the derivate $\frac{\partial \vec{r}}{\partial u_1}$ gives the tangential vector of the coordinate line $u_1(u_2,u_3 = \text{const.})$, with the magnitude

$$h_1 = \left| \frac{\partial \vec{r}}{\partial u_1} \right| \qquad \text{and the unity vector} \quad \vec{e}_1 = \frac{\dfrac{\partial \vec{r}}{\partial u_1}}{h_1} \tag{9-2}$$

analogous with h_2 and h_3 [24].

The values h_1, h_2, h_3 are called scale (or geometry) factors and are functions of the curvilinear coordinates:

$$h_1 = h_1(u_1, u_2, u_3) \qquad h_2 = h_2(u_1, u_2, u_3) \qquad h_3 = h_3(u_1, u_2, u_3) \tag{9-3}$$

The vector $PP' = d\vec{r}$ of two adjacent points $P(u_1,u_2,u_3)$ and $P'(u_1+du_1,u_2+du_2,u_3+du_3)$ can be derived through:

$$d\vec{r} = \frac{\partial \vec{r}}{\partial u_1} du_1 + \frac{\partial \vec{r}}{\partial u_2} du_2 + \frac{\partial \vec{r}}{\partial u_3} du_3 \quad \text{or} \quad d\vec{r} = h_1 du_1 \vec{e}_1 + h_2 du_2 \vec{e}_2 + h_3 du_3 \vec{e}_3 \tag{9-4}$$

The incremental distance *ds* between those two points can be written as:

$$d\vec{r} \cdot d\vec{r} = ds^2 = h_1^2 du_1^2 + h_2^2 du_2^2 + h_3^2 du_3^2 \tag{9-5}$$

Analogous the incremental volume element $d\tau$ can be found. The components of $d\vec{r}$ form an infinitesimal rectangular parallelepiped which volume equals:

$$d\tau = h_1 h_2 h_3 du_1 du_2 du_3 \tag{9-6}$$

9.2 Spherical or Polar Coordinates

In spherical coordinates the position of a point *P* is determined by the three curvilinear coordinates *r*, φ, λ, where *r* is the radius vector, φ the latitude and λ the longitude. In most cases the polar angle $\vartheta = 90 - \varphi$ is used instead of the latitude (Figure 9.2).

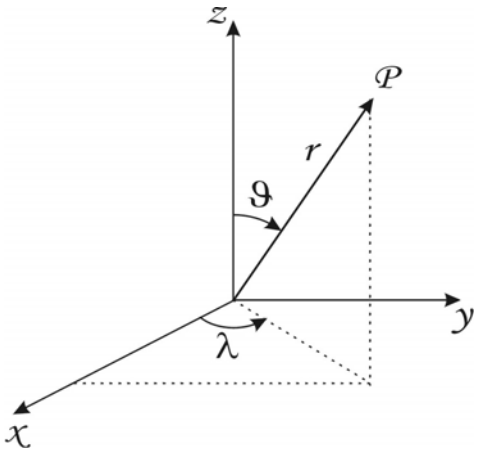

Figure 9.2: Polar coordinates r, ϑ, λ.

The three orthogonal coordinate surfaces are concentric spheres about the origin (*r* = const.), right circular cones with apex at the origin and axis along the *z*-axis (ϑ = const.), and half-planes through *z* (λ = const.), respectively. The position of a point *P* is given through:

$$\vec{r} = \begin{Bmatrix} x = r\cos\varphi\cos\lambda \\ y = r\cos\varphi\sin\lambda \\ z = r\sin\varphi \end{Bmatrix} = \begin{Bmatrix} x = r\sin\vartheta\cos\lambda \\ y = r\sin\vartheta\sin\lambda \\ z = r\cos\vartheta \end{Bmatrix} \tag{9-7}$$

$$\text{correspondingly} \qquad \left\{ \begin{array}{c} r = \sqrt{x^2 + y^2 + z^2} \\ \vartheta = \arctan\left(\sqrt{\dfrac{x^2 + y^2}{z^2}} \right) \\ \lambda = \arctan\left(\dfrac{y}{x} \right) \end{array} \right\} \tag{9-8}$$

The scale factors for spherical/polar coordinates become:

$$h_1 = \left| \frac{\partial \vec{r}}{\partial r} \right| = 1 \qquad h_2 = \left| \frac{\partial \vec{r}}{\partial \vartheta} \right| = r \qquad h_3 = \left| \frac{\partial \vec{r}}{\partial \lambda} \right| = r \cos\varphi = r \sin\vartheta \tag{9-9}$$

and thus the infinitesimal volume element:

$$d\tau = h_1 h_2 h_3 \, dr \, d\vartheta \, d\lambda = r^2 \sin\vartheta \, dr \, d\vartheta \, d\lambda \tag{9-10}$$

In some formulas the derivatives of the polar coordinates with respect to the Cartesian coordinates are needed and stated as:

$$\begin{array}{lll} \dfrac{\partial r}{\partial x} = \dfrac{x}{r} & \dfrac{\partial r}{\partial y} = \dfrac{y}{r} & \dfrac{\partial r}{\partial z} = \dfrac{z}{r} \\ \dfrac{\partial \vartheta}{\partial x} = \dfrac{x \cdot z}{r^2 \sqrt{x^2 + y^2}} & \dfrac{\partial \vartheta}{\partial y} = \dfrac{y \cdot z}{r^2 \sqrt{x^2 + y^2}} & \dfrac{\partial \vartheta}{\partial z} = -\dfrac{\sqrt{x^2 + y^2}}{r^2} \\ \dfrac{\partial \lambda}{\partial x} = -\dfrac{y}{x^2 + y^2} & \dfrac{\partial \lambda}{\partial y} = \dfrac{x}{x^2 + y^2} & \dfrac{\partial \lambda}{\partial z} = 0 \end{array} \tag{9-11}$$

9.3 SPHEROIDAL COORDINATES

A spheroid is a surface of revolution obtained by rotating an ellipse about an axis (depending on whether $c < a$ or $c > a$ it is called an oblate spheroid or prolate spheroid, respectively). In the case of planetary bodies, the major axis a lies in the body's equatorial plane (and in general is equated with the x-axis) and the minor axis c coincides with the axis of rotation (z-axis). The y-axis is perpendicular to the x-axis and oriented counter clockwise (Figure 9.3).

The fundamental equation of a spheroid with axis $a = b > c$ is defined as:

$$\frac{x^2 + y^2}{a^2} + \frac{z^2}{c^2} = 1 \tag{9-12}$$

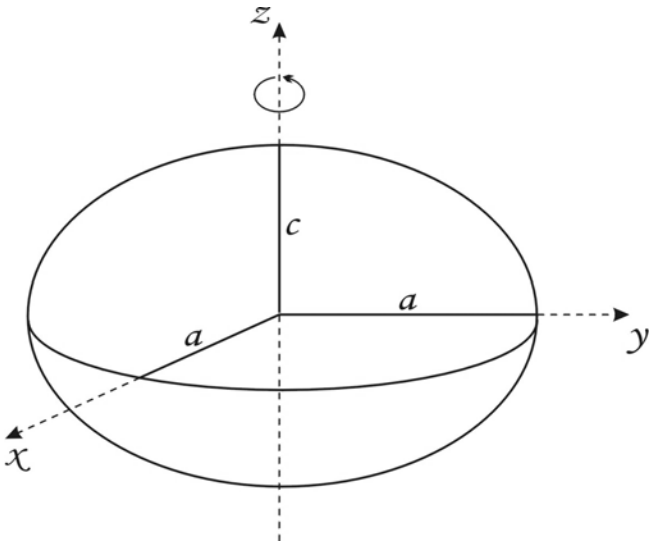

Figure 9.3: Spheroid and axis.

For the determination of the position of a point P the curvilinear coordinates u, ϑ, λ are used, where u is the minor axis and $\bar{e} = a \cdot e$ the constant linear eccentricity [32]:

$$\vec{r} = \begin{Bmatrix} x = \sqrt{u^2 + \bar{e}^2}\sin\vartheta\cos\lambda \\ y = \sqrt{u^2 + \bar{e}^2}\sin\vartheta\sin\lambda \\ z = u\cos\vartheta \end{Bmatrix} \qquad \text{and} \qquad r = |\vec{r}| = \sqrt{u^2 + \bar{e}^2\sin^2\vartheta} \tag{9-13}$$

The major axis a equals $\sqrt{u^2 + \bar{e}^2}$, ϑ is the reduced polar distance, and λ the longitude (Figure 9.4).

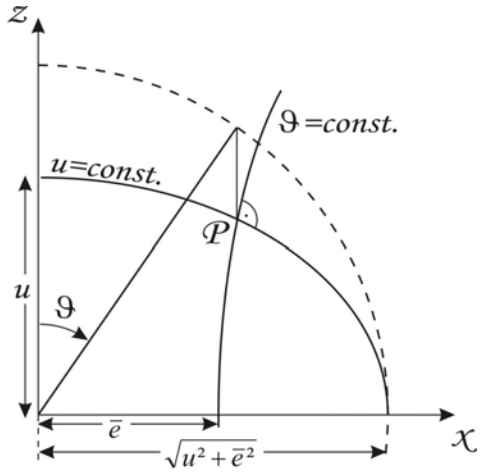

Figure 9.4: Spheroidal Coordinates.

Elimination of ϑ and λ (u = const.) gives confocal spheroids with minor axis u and constant linear eccentricity $\bar{e}$:

$$\frac{x^2 + y^2}{u^2 + \bar{e}^2} + \frac{z^2}{u^2} = 1 \tag{9-14}$$

Elimination of u and λ (ϑ=const) gives one-sheeted hyperboloids with constant focal circle $(x^2 + y^2) = \bar{e}^2$:

$$\frac{x^2 + y^2}{\bar{e}^2 \sin^2 \vartheta} - \frac{z^2}{\bar{e}^2 \cos^2 \vartheta} = 1 \tag{9-15}$$

The third surface (λ = const.) are planes through the rotational axis and are given by:

$$y = x \tan \lambda \tag{9-16}$$

The scale factors for spheroidal coordinates become:

$$h_1 = \left|\frac{\partial \vec{r}}{\partial u}\right| = \sqrt{\frac{u^2 + \bar{e}^2 \cos^2 \vartheta}{u^2 + \bar{e}^2}} \qquad h_2 = \left|\frac{\partial \vec{r}}{\partial \vartheta}\right| = \sqrt{u^2 + \bar{e}^2 \cos^2 \vartheta} \qquad h_3 = \left|\frac{\partial \vec{r}}{\partial \lambda}\right| = \sqrt{(u^2 + \bar{e}^2) \sin^2 \vartheta} \tag{9-17}$$

The incremental volume element is calculated through:

$$d\tau = h_1 h_2 h_3 \, du \, d\vartheta \, d\lambda = (u^2 + \bar{e}^2 \cos^2 \vartheta) \sin \vartheta \, du \, d\vartheta \, d\lambda \tag{9-18}$$

The above system turns into spherical (or polar) coordinates for $\bar{e} = 0$. The spheroidal coordinates are a special case of the general ellipsoidal coordinates.

9.4 ELLIPSOIDAL COORDINATES

Ellipsoidal coordinates can be related in various ways to the Cartesian coordinates. They are defined with respect to a fundamental ellipsoid of semi-axis $a > b > c$:

$$\frac{x^2}{a^2} + \frac{y^2}{b^2} + \frac{z^2}{c^2} = 1 \tag{9-19}$$

If a constant γ is added to the semi-axis, the resulting quadric is a surface whose principal sections have the same foci as before – a surface confocal with the original [33]:

$$\frac{x^2}{a^2 + \gamma} + \frac{y^2}{b^2 + \gamma} + \frac{z^2}{c^2 + \gamma} = 1 \tag{9-20}$$

For $\gamma > -c^2$ the surface is an ellipsoid, for $-c^2 > \gamma > -b^2$ the surface is an elliptic hyperboloid of one sheet, and for $-b^2 > \gamma > -a^2$ the surface is an elliptic hyperboloid of two sheets (Figure 9.5). Calling the parameters γ in order of magnitude λ, μ, ν a set of orthogonal curvilinear coordinates is defined – the ellipsoidal coordinates. The coordinate λ (not to mistake for the longitude of a sphere or spheroid!) is often called the 'elliptic radius' by analogy with the spherical radius r.

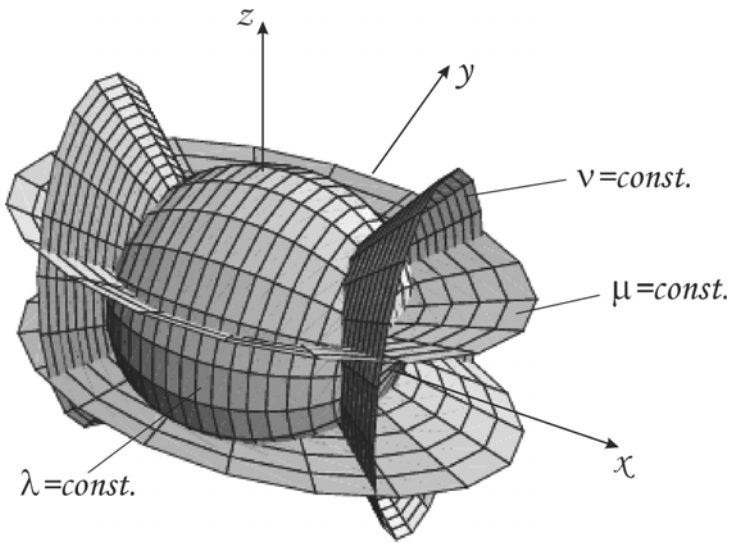

Figure 9.5: Ellipsoidal coordinates λ, μ, ν.

The equations for the quadrics can therefore be written as:

$$\begin{aligned}
&\frac{x^2}{a^2+\lambda}+\frac{y^2}{b^2+\lambda}+\frac{z^2}{c^2+\lambda}=1 && -c^2<\lambda<\infty \\
&\frac{x^2}{a^2+\mu}+\frac{y^2}{b^2+\mu}+\frac{z^2}{c^2+\mu}=1 && -b^2<\mu<-c^2 \\
&\frac{x^2}{a^2+\nu}+\frac{y^2}{b^2+\nu}+\frac{z^2}{c^2+\nu}=1 && -a^2<\nu<-b^2
\end{aligned} \tag{9-21}$$

For every point $P(x,y,z)$ there is a unique set of ellipsoidal coordinates. However, a set of (λ,μ,ν) specifies eight points symmetrically located in octants. Solving the above system for x, y and z gives:

$$\begin{aligned}
x^2&=\frac{(a^2+\lambda)(a^2+\mu)(a^2+\nu)}{(a^2-b^2)(a^2-c^2)} \\
y^2&=-\frac{(b^2+\lambda)(b^2+\mu)(b^2+\nu)}{(a^2-b^2)(b^2-c^2)} \\
z^2&=\frac{(c^2+\lambda)(c^2+\mu)(c^2+\nu)}{(a^2-c^2)(b^2-c^2)}
\end{aligned} \tag{9-22}$$

In the same manner as before the scale factors can be found:

$$\begin{aligned}
h_1&=\left|\frac{\partial\vec{r}}{\partial\lambda}\right|=\sqrt{\left(\frac{\partial x}{\partial\lambda}\right)^2+\left(\frac{\partial y}{\partial\lambda}\right)^2+\left(\frac{\partial z}{\partial\lambda}\right)^2}=\frac{1}{2}\sqrt{\frac{(\lambda-\mu)(\lambda-\nu)}{(a^2+\lambda)(b^2+\lambda)(c^2+\lambda)}} \\
h_2&=\left|\frac{\partial\vec{r}}{\partial\mu}\right|=\sqrt{\left(\frac{\partial x}{\partial\mu}\right)^2+\left(\frac{\partial y}{\partial\mu}\right)^2+\left(\frac{\partial z}{\partial\mu}\right)^2}=\frac{1}{2}\sqrt{-\frac{(\lambda-\mu)(\mu-\nu)}{(a^2+\mu)(b^2+\mu)(c^2+\mu)}} \\
h_3&=\left|\frac{\partial\vec{r}}{\partial\nu}\right|=\sqrt{\left(\frac{\partial x}{\partial\nu}\right)^2+\left(\frac{\partial y}{\partial\nu}\right)^2+\left(\frac{\partial z}{\partial\nu}\right)^2}=\frac{1}{2}\sqrt{\frac{(\lambda-\nu)(\mu-\nu)}{(a^2+\nu)(b^2+\nu)(c^2+\nu)}}
\end{aligned} \tag{9-23}$$

as well as the infinitesimal volume element:

$$d\tau = h_1 h_2 h_3 d\lambda\, d\mu\, d\nu = \\ = \frac{(\lambda-\mu)(\lambda-\nu)(\mu-\nu)}{8\sqrt{-(a^2+\lambda)(b^2+\lambda)(c^2+\lambda)(a^2+\mu)(b^2+\mu)(c^2+\mu)(a^2+\nu)(b^2+\nu)(c^2+\nu)}} \quad (9\text{-}24)$$

9.5 SHAPE APPROXIMATION

The satellite systems of the outer planets include many members that are small (mean radius < 150 km) which are usually described as irregularly shaped as they are generally been considered to be remnants of collisional fragmentation. Most of the asteroids in our solar system fall within this category as well. The data of the shape of these small bodies is obtained through limb coordinate measurements from spacecraft images which allow for a much more scientifically useful application, with respect to e.g. body formation, cratering history, interior structure, and relationship to planetary rings [29].

Coordinates of limb points are measured to sub-pixel accuracy from the raw digital images using empirically derived criteria for detection of high contrast edges. They are corrected for electronic distortion of the image and scaled to the object, using the camera focal length and the distance from spacecraft to target. The limb data is usually specified in longitude, latitude and radius. The limb coordinates can furthermore be fit by ellipses, which allow an accurate measurement of the volume of these irregular objects. Ellipses fit to limb data taken from several different orientations and the volume estimate can be combined to solve for an ellipsoidal description of the body with axes *a*, *b* and *c* (for Amalthea's shape data and axes see chapter 4.3)

A full description of these measurement and calculation techniques is given in Dermott and Thomas [9].

10 DEFINITION OF COORDINATE SYSTEMS

The orbital parameters (chapter 6.1) and positions of planetary bodies and spacecraft in our solar system have to refer to appropriate coordinate systems, e.g. local body-fixed (chapter 9) or inertial coordinate systems. Depending on the problem, a mathematical formulation of the relationship between those systems is of importance.

10.1 INERTIAL COORDINATE SYSTEM

Within the Newton's mechanics an inertial system is characterised as a system where the 1st Newton axiom is valid – such a system is without motion or moves uniformly in a straight line without rotation. In small scales like in our solar system this assumption is sufficient, though in some cases small corrections because of relativistic effects need to be made.

The IAU has kinematically defined an International Celestial Reference System (ICRS) with origin in the barycentre of our solar system, which lies within the Sun. The ICRS is based on the directions to extra-galactic radio sources, called quasars [7].

As measurements are derived on Earth (or from artificial satellites orbiting the Earth), the origin of the ICRS is usually moved to the Earth's centre of gravity, the geocentre. Barycentric and geocentric time scales differ by small periodic terms. Because of the variability of the Earth's equatorial and ecliptic planes with time, it is necessary to define coordinates with respect to a given date, called epoch – e.g. the J2000.0 coordinate system has the standard epoch of January 1, 2000, 12pm UTC.

10.1.1 ORIENTATION

The diameter of the Earth is insignificantly small with respect to the distance to the stars, thus all directions from the Earth to a star are parallel. Furthermore, the stars seem to be positioned on a sphere with the Earth in its centre. If the radius of this sphere is set to unity, the direction to a star can be described by means of two angles, latitude and longitude, as long as a reference plane and an origin (prime meridian) are defined.

In mathematical and geodetic terminology, the terms 'latitude' and 'longitude' refer to a right-hand coordinate system in which latitude is defined as the angle between a vector and the equatorial plane, and longitude is the angle between the vector and the plane of the prime meridian measured in an eastern direction [8].

Within the ICRS the reference plane lies close to the Earth equator of J2000.0. The latitude, called declination δ, is measured north and south of the equator; north latitudes are designated as positive. The Non-Rotating Origin (NRO), which lies close to the vernal equinox (γ) J2000.0, defines the origin for the measurement of the longitude, also called right ascension α, which is measured eastwards from 0 to 24 hours, respectively 0°-360° (Figure 10.1).

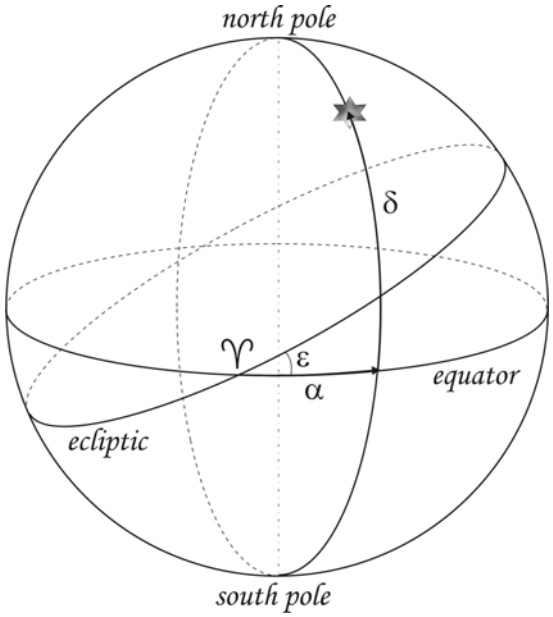

Figure 10.1: Inertial equator system (ε … ecliptic obliquity).

As the proportions of our solar system are insignificantly small with respect to the distances in the universe, the NRO is also used as a reference point for other planetocentric coordinate systems.

10.2 PLANETARY COORDINATE SYSTEMS

The coordinates described in chapter 9 are local body-fixed coordinates with the origin usually located in the centre of mass. The position of a spacecraft can be expressed within such a planetocentric coordinate system as well. In order to associate the local coordinate system with the inertial the following definitions have been made by the IAU/IAG/COSPAR* Working Group on Cartographic Coordinates and Rotational Elements of the Planets and Satellites [8] (Figure 10.2):

- Planetary coordinate systems are defined relative to their mean axis of rotation and various definitions of longitude depending on the body. In the absence of other information, the axis of rotation is assumed to be normal to the mean orbital plane.
- The longitude systems of most of the bodies in our solar system with observable rigid surfaces have been defined by references to a surface feature such as a crater. In cases of small planetary satellites the prime meridian coincides with the direction to the main planet.
- The north pole is that pole of rotation that lies on the north side of the invariable plane of the solar system.
- The direction of the north pole is specified by the value of its right ascension α_0 and declination δ_0, which are usually given in function of Julian centuries T from the standard epoch.
- The location of the prime meridian is specified by the angle W that is measured along the body's equator (in an easterly direction with respect to the planet's north pole) from the node Q.

* International Astronomical Union (IAU), International Association of Geodesy (IAG), Committee on Space Research (COSPAR)

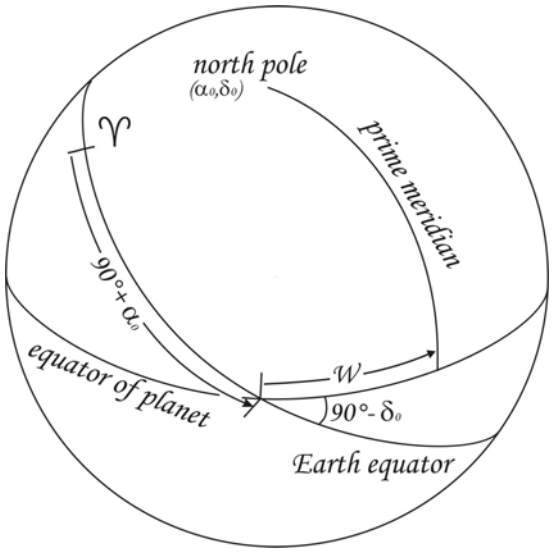

Figure 10.2: Reference system used to define the orientation of a planet.

Because the prime meridian is assumed to rotate uniformly with the planet, W accordingly varies linearly with time, which is stated in the expression of W as:

$$W = W_0 + Wd \tag{10-1}$$

where d is the interval in days from the standard epoch. For Amalthea's data refer to chapter 4.3.

If W increases with time, the planet has a prograde rotation and if W decreases with time, the rotation is said to be retrograde.

10.3 TRANSFORMATIONS

The transformation of a point P (given through the coordinate vector $\vec{x}$) from the inertial coordinate system (index i) to a body-fixed coordinate system (index B) is in general given through a displacement of the origin, up to three rotations and a change of scale. In the case of the Earth and the variability of its equatorial plane, the transformation needs to consider Earth-rotation, displacement of the pole, nutation and precession.

In the scope of this work, and with respect to Amalthea, the coordinate systems are orthogonal, the origin of both systems is placed in the centre of the body, and the scale is identical. The transformation therefore reduces to:

$$\vec{x}_B = R\vec{x}_i \tag{10-2}$$

where R defines the orthogonal rotational matrix.

R is compound of three rotational matrixes with angles ε_x, ε_y, ε_z about the coordinate axis x, y, z, and can be stated as [4]:

$$R_x = \begin{pmatrix} 1 & 0 & 0 \\ 0 & \cos\varepsilon_x & \sin\varepsilon_x \\ 0 & -\sin\varepsilon_x & \cos\varepsilon_x \end{pmatrix} \quad R_y = \begin{pmatrix} \cos\varepsilon_y & 0 & -\sin\varepsilon_y \\ 0 & 1 & 0 \\ \sin\varepsilon_y & 0 & \cos\varepsilon_y \end{pmatrix} \quad R_z = \begin{pmatrix} \cos\varepsilon_z & \sin\varepsilon_z & 0 \\ -\sin\varepsilon_z & \cos\varepsilon_z & 0 \\ 0 & 0 & 1 \end{pmatrix} \tag{10-3}$$

$$R = R_z R_y R_x =$$

$$= \begin{pmatrix} \cos\varepsilon_y \cos\varepsilon_z & \sin\varepsilon_x \sin\varepsilon_y \cos\varepsilon_z + \cos\varepsilon_x \sin\varepsilon_z & -\cos\varepsilon_x \sin\varepsilon_y \cos\varepsilon_z + \sin\varepsilon_x \sin\varepsilon_z \\ -\cos\varepsilon_y \sin\varepsilon_z & -\sin\varepsilon_x \sin\varepsilon_y \sin\varepsilon_z + \cos\varepsilon_x \cos\varepsilon_z & \cos\varepsilon_x \sin\varepsilon_y sun\varepsilon_z + \sin\varepsilon_x \cos\varepsilon_z \\ \sin\varepsilon_y & -\sin\varepsilon_x \cos\varepsilon_y & \cos\varepsilon_x \cos\varepsilon_y \end{pmatrix} \tag{10-4}$$

Vice versa the rotational angles can be derived:

$$\tan\varepsilon_x = -\frac{a_{32}}{a_{33}} \qquad \sin\varepsilon_y = a_{31} \qquad \tan\varepsilon_z = -\frac{a_{21}}{a_{11}} \tag{10-5}$$

Because of the orthogonal characteristics the transposed matrix results to:

$$R^T = R_x^T R_y^T R_z^T =$$

$$= \begin{pmatrix} \cos\varepsilon_y \cos\varepsilon_z & -\sin\varepsilon_z \cos\varepsilon_y & \sin\varepsilon_y \\ \sin\varepsilon_x \sin\varepsilon_y \cos\varepsilon_z + \cos\varepsilon_x \sin\varepsilon_z & -\sin\varepsilon_x \sin\varepsilon_y \sin\varepsilon_z + \cos\varepsilon_x \cos\varepsilon_z & -\sin\varepsilon_x \cos\varepsilon_y \\ -\cos\varepsilon_x \sin\varepsilon_y \cos\varepsilon_z + \sin\varepsilon_x \sin\varepsilon_z & \cos\varepsilon_x \sin\varepsilon_y \sin\varepsilon_z + \sin\varepsilon_x \cos\varepsilon_z & \cos\varepsilon_x \cos\varepsilon_y \end{pmatrix} \tag{10-6}$$

and hence the back transformation from body-fixed to inertial:

$$\vec{x}_i = R^T \vec{x}_B \tag{10-7}$$

The components a_{11}, a_{12}, a_{13} of the orthogonal matrix can be expressed through:

$$a_{11} = a_{22}a_{33} - a_{23}a_{32} \qquad a_{12} = a_{23}a_{31} - a_{21}a_{33} \qquad a_{13} = a_{21}a_{32} - a_{22}a_{31} \tag{10-8}$$

Only two identical points in both systems are necessary in order to derive the components of the matrix or the rotational angles, nevertheless three points are used in general for a better determination.

In the frame if this work it is as well necessary to transform velocities and accelerations from one system into the other. Consequently the derivates of the transformation equation need to be formed:

$$\begin{aligned} \dot{\vec{x}}_B &= \dot{R}\vec{x}_i + R\dot{\vec{x}}_i \\ \ddot{\vec{x}}_B &= \ddot{R}\vec{x}_i + 2\dot{R}\dot{\vec{x}}_i + R\ddot{x}_i \end{aligned} \tag{10-9}$$

The products $\ddot{R}\vec{x}_i$ and $\dot{R}\dot{x}_i$ can be numerically neglected, and thus the transformation of the acceleration vector results to:

$$\ddot{\vec{x}}_B = R\ddot{\vec{x}}_i \quad \text{and} \quad \ddot{\vec{x}}_i = R^T \ddot{\vec{x}}_B \tag{10-10}$$

11 POTENTIAL THEORY AND GRAVITY FIELDS

According to Newton's law of gravitation two masses attract each other with a force that is proportional to the product of the masses and conversely proportional to the square of their distance (chapter 6.1). The effect of the gravitation can be described by means of the gradient of a scalar function – the potential (Joseph-Louis Lagrange, 1777). With respect to the purpose of this work, the following chapter explains the fundamentals of potential theory, including the basics of spherical harmonics. A more detailed derivation can be found in Heiskanen and Moritz [14].

11.1 POTENTIAL OF GRAVITATION

For simplicity the attracted mass (m_2) in Newton's law of gravitation (6-1) is set to unity:

$$\left|\vec{F}\right| = \frac{GM}{r^2} \tag{11-1}$$

If the force $\vec{F}(x, y, z)$ can be linked to a scalar function $V(x,y,z)$ through

$$F_x = -\frac{\partial V}{\partial x} \qquad F_y = -\frac{\partial V}{\partial y} \qquad F_z = -\frac{\partial V}{\partial z} \tag{11-2}$$

V is called the potential of gravitation:

$$V = \frac{GM}{r} \tag{11-3}$$

respectively $\vec{F}$ is called the gradient of the potential V:

$$\vec{F} = \text{grad } V \tag{11-4}$$

The potential V is continuous throughout the whole space and vanishes at infinity. The first derivatives of V, the force components, are also continuous throughout space, but not so the second derivatives. At points where the density changes discontinuously (e.g. inside an attracting body) the potential satisfies Poisson's equation:

$$\Delta V = \frac{\partial^2 V}{\partial x^2} + \frac{\partial^2 V}{\partial y^2} + \frac{\partial^2 V}{\partial z^2} = -4\pi G\,\rho(x, y, z) \tag{11-5}$$

Outside the attracting body, in empty space where the density ρ is zero, the potential satisfies the Laplace equation:

$$\Delta V = 0 \tag{11-6}$$

Its solutions are called harmonic functions. Hence the potential of gravitation is a harmonic function outside the attracting mass (but not inside).

The harmonic function V is uniquely determined by its values on the surface of the attracting body. However, there are infinitely many mass distributions which have the given harmonic function V as exterior potential. It is therefore impossible to determine uniquely the generating masses from the external potential, e.g. the interior structure of a planetary body

cannot be defined exclusively by the potential of gravitation. To determine the problem more completely, additional information, like geology or seismic measurements, is necessary.

11.2 SPHERICAL HARMONICS

The most important harmonic functions are the so-called spherical harmonics. In order to solve Laplace's equation for the potential of a spherical body, the variables r, ϑ, λ need to be separated by means of the trial substitution:

$$V(r,\vartheta,\lambda) = f(r)Y(\vartheta,\lambda) \tag{11-7}$$

Solutions are given by the functions:

$$f(r) = r^n \qquad f(r) = \frac{1}{r^{n+1}} \tag{11-8}$$

As the sum of these results is also a solution, the potential V can now be written as:

$$V = \sum_{n=0}^{\infty} r^n Y_n(\vartheta,\lambda) \qquad V = \sum_{n=0}^{\infty} \frac{Y_n(\vartheta,\lambda)}{r^{n+1}} \tag{11-9}$$

where the second case yields the external potential. Physical significant solutions are given only for integer values of n. To determine the so-called surface harmonics $Y_n(\vartheta,\lambda)$ a second trial substitution needs to be implemented:

$$Y_n(\vartheta,\lambda) = g(\vartheta)\cdot h(\lambda) \tag{11-10}$$

with solutions:

$$h(\lambda) = \cos m\lambda \qquad h(\lambda) = \sin m\lambda \qquad g(\vartheta) = P_{nm}(\cos\vartheta) \tag{11-11}$$

The $P_{nm}(\cos\vartheta)$ are called Legendre functions and will be considered in some detail in the next section. The general expression for the surface harmonic of degree n now reads (A_{nm} and B_{nm} are arbitrary constants):

$$Y_n(\vartheta,\lambda) = \sum_{m=0}^{n}\left[A_{nm}P_{nm}(\cos\vartheta)\cos m\lambda + B_{nm}P_{nm}(\cos\vartheta)\sin m\lambda\right] \tag{11-12}$$

Physical evocative solutions are provided only for $m \le n$.

$$V(r,\vartheta,\lambda) = \sum_{n=0}^{\infty}\frac{1}{r^{n+1}}\sum_{m=0}^{n}\left[A_{nm}P_{nm}(\cos\vartheta)\cos m\lambda + B_{nm}P_{nm}(\cos\vartheta)\sin m\lambda\right] \tag{11-13}$$

respectively with abbreviations

$$V(r,\vartheta,\lambda) = \sum_{n=0}^{\infty}\frac{1}{r^{n+1}}\sum_{m=0}^{n}\left[A_{nm}C_{nm}(\vartheta,\lambda) + B_{nm}S_{nm}(\vartheta,\lambda)\right] \tag{11-14}$$

gives the general solution of Laplace's equation for the external potential.

11.2.1 LEGENDRE FUNCTIONS OF THE FIRST KIND

It is convenient to transform the Legendre equation by the substitution

$$t = \cos\vartheta \tag{11-15}$$

and hence the solutions can be written as:

$$P_{nm}(t) = \frac{1}{2^n n!}\left(1-t^2\right)^{\frac{m}{2}} \frac{d^{n+m}}{dt^{n+m}}\left(t^2-1\right)^n \tag{11-16}$$

For $m = 0$ the functions are called Legendre polynomials and denoted as $P_n(t)$.

Higher order polynomials can be obtained more simply by the recursion formula:

$$P_n(t) = -\frac{n-1}{n}P_{n-2}(t) + \frac{2n-1}{n}tP_{n-1}(t) \tag{11-17}$$

The associated Legendre functions can easily be deduced from the Legendre polynomials by means of the equation:

$$P_{nm}(t) = \left(1-t^2\right)^{\frac{m}{2}} \frac{d^m P_n(t)}{dt^m} \tag{11-18}$$

For the use in computer programming the following expression is more convenient:

$$P_{nm}(t) = 2^{-n}\left(1-t^2\right)^{\frac{m}{2}} \sum_{k=0}^{r}(-1)^k \frac{(2n-2k)!}{k!(n-k)!(n-m-2k)!} t^{n-m-2k} \tag{11-19}$$

where r is the greatest integer $\leq \frac{n-m}{2}$; e.g. r is $\frac{n-m}{2}$ or $\frac{n-m-1}{2}$, whichever is an integer.

The derivates of the Legendre functions are given through:

$$\frac{dP_{nm}(\cos\vartheta)}{d\vartheta} = -\sin\vartheta\left[-\frac{mt}{2^n}\left(1-t^2\right)^{\frac{m}{2}-1}\sum_{k=0}^{r}S_{nmk}t^{n-m-2k} + \frac{1}{2^n}\left(1-t^2\right)^{\frac{m}{2}}\sum_{k=0}^{\bar{r}}(n-m-2k)S_{nmk}t^{n-m-2k-1}\right]$$

$$S_{nmk} = (-1)^k \frac{(2n-2k)!}{k!(n-k)!(n-m-2k)!} \tag{11-20}$$

The first few Legendre polynomials, associated Legendre functions and derivates are given in Appendix E.1.

11.3 EXPANSION OF A FUNCTION INTO SPHERICAL HARMONICS

A general function f on the surface σ of the sphere (r set to unity) can be expanded into a series of surface spherical harmonics:

$$f(\vartheta,\lambda)=\sum_{n=0}^{\infty}\sum_{m=0}^{n}\left[A_{nm}C_{nm}(\vartheta,\lambda)+B_{nm}S_{nm}(\vartheta,\lambda)\right] \tag{11-21}$$

In order to determine the coefficients A_{nm} and B_{nm} the orthogonality relations are needed, which mean that the integral over the unit sphere of the product of any two different functions C_{nm} and S_{nm} is zero and the product of two equal functions is given through:

$$\iint_{\sigma} C_{nm}^2(\vartheta,\lambda)d\sigma=\iint_{\sigma} S_{nm}^2(\vartheta,\lambda)d\sigma=\frac{2\pi(n+m)!}{(2n+1)(n-m)!}\quad \text{for}\quad m\neq 0 \tag{11-22}$$

$$\iint_{\sigma} C_{n0}^2(\vartheta,\lambda)d\sigma=\frac{4\pi}{2n+1}\quad \text{for}\quad m=0 \tag{11-23}$$

The solutions for the coefficients A_{nm} and B_{nm} can be stated as:

$$\begin{aligned}
A_{n0} &= \frac{2n+1}{4\pi}\int_0^{2\pi}\int_0^{\pi} f(\vartheta,\lambda)P_n(\cos\vartheta)\sin\vartheta\, d\vartheta d\lambda \\
A_{nm} &= \frac{2n+1}{2\pi}\frac{(n-m)!}{(n+m)!}\int_0^{2\pi}\int_0^{\pi} f(\vartheta,\lambda)C_{nm}(\vartheta,\lambda)\sin\vartheta\, d\vartheta d\lambda \\
B_{nm} &= \frac{2n+1}{2\pi}\frac{(n-m)!}{(n+m)!}\int_0^{2\pi}\int_0^{\pi} f(\vartheta,\lambda)S_{nm}(\vartheta,\lambda)\sin\vartheta\, d\vartheta d\lambda
\end{aligned} \tag{11-24}$$

In general, the function $f(\vartheta,\lambda)$ is not given analytically but through observables, e.g. temperature, atmospheric pressure, heights, and gravity. The degree of expansion depends on the quantity of observables – each observable defines one equation and thus $(n+1)^2$ equations are needed for the number of coefficients up to degree n. If the data is given on specific latitudes and equidistant longitudes, the derivation of the coefficients A_{nm} and B_{nm} becomes much easier (Franz Neumann, 1798-1895).

11.3.1 SECOND METHOD OF NEUMANN

For an expansion up to degree n the values for $f(\vartheta,\lambda)$ at the intersection of $2n$ equidistant meridians with $2n+1$ 'optional' almucantarates are required, which amounts to $2n(n+1)$ values [32].

Initially, $n+1$ auxiliary quantities $a_1, a_2, a_3, ..., a_{n+1}$ need to be determined:

$$a_1 t_1^i + a_2 t_2^i + ... + a_{n+1} t_{n+1}^i = \begin{cases} 0 & i = odd \\ 2/(i+1) & i = even \,\&\, 0 \end{cases} \qquad 0 \le i \le 2n+1 \tag{11-25}$$

with $t_1, t_2, t_3, ..., t_{n+1}$ being the roots of $P_{n+1}(t)=0$, and thus the latitudes. The values of a and t for degree 4, 5 and 6 are given in Appendix E.2.

Further, the quantity $\frac{2\pi}{2n} = \frac{\pi}{n} = \lambda_0$ is set and new coefficients c_{mj} and s_{mj} are introduced:

$$
\begin{aligned}
c_{0,j} &= \frac{1}{2n}\sum_{k=0}^{2n-1} f\left(\vartheta_j, k\lambda_0\right) & s_{0,j} &= 0 \\
c_{1,j} &= \frac{1}{n}\sum_{k=0}^{2n-1} f\left(\vartheta_j, k\lambda_0\right)\cos k\lambda_0 & s_{1,j} &= \frac{1}{n}\sum_{k=0}^{2n-1} f\left(\vartheta_j, k\lambda_0\right)\sin k\lambda_0 \\
c_{2,j} &= \frac{1}{n}\sum_{k=0}^{2n-1} f\left(\vartheta_j, k\lambda_0\right)\cos 2k\lambda_0 & s_{2,j} &= \frac{1}{n}\sum_{k=0}^{2n-1} f\left(\vartheta_j, k\lambda_0\right)\sin 2k\lambda_0 \\
&\ldots\ldots & &\ldots\ldots \\
c_{(m-1),j} &= \frac{1}{n}\sum_{k=0}^{2n-1} f\left(\vartheta_j, k\lambda_0\right)\cos\left((m-1)k\lambda_0\right) & s_{(m-1),j} &= \frac{1}{n}\sum_{k=0}^{2n-1} f\left(\vartheta_j, k\lambda_0\right)\sin\left((m-1)k\lambda_0\right) \\
c_{m,j} &= \frac{1}{2n}\sum_{k=0}^{2n-1} f\left(\vartheta_j, k\lambda_0\right)\cos mk\lambda_0 & s_{m,j} &= 0
\end{aligned}
\qquad (11\text{-}26)
$$

with $0 \le m \le n$, and $f\left(\vartheta_j, k\lambda_0\right)$ being the data values.

Finally, the coefficients of the spherical expansion can be written as:

$$
\begin{aligned}
A_{nm} &= \frac{2n+1}{2}\frac{(n-m)!}{(n+m)!}\sum_{j=1}^{n+1} a_j c_{mj} P_{nm}\left(t_j\right) \\
B_{nm} &= \frac{2n+1}{2}\frac{(n-m)!}{(n+m)!}\sum_{j=1}^{n+1} a_j s_{mj} P_{nm}\left(t_j\right)
\end{aligned}
\qquad (11\text{-}27)
$$

11.4 GRAVITATIONAL POTENTIAL OF A PLANETARY BODY

In order to develop the gravitational potential V at a fixed point P outside an attracting mass the effect of a variable mass element dM needs to be determined. Therefore, V is denoted as:

$$V = G\iiint_{body} \frac{dM}{l} \qquad (11\text{-}28)$$

with l being the distance between P and dM (Figure 11.1). The expansion of the reciprocal distance into zonal harmonics can be written as:

$$\frac{1}{l} = \sum_{n=0}^{\infty} \frac{r'^n}{r^{n+1}} P_n\left(\cos\psi\right) \quad \text{with} \quad \cos\psi = \cos\vartheta\cos\vartheta' + \sin\vartheta\sin\vartheta'\cos\left(\lambda - \lambda'\right) \qquad (11\text{-}29)$$

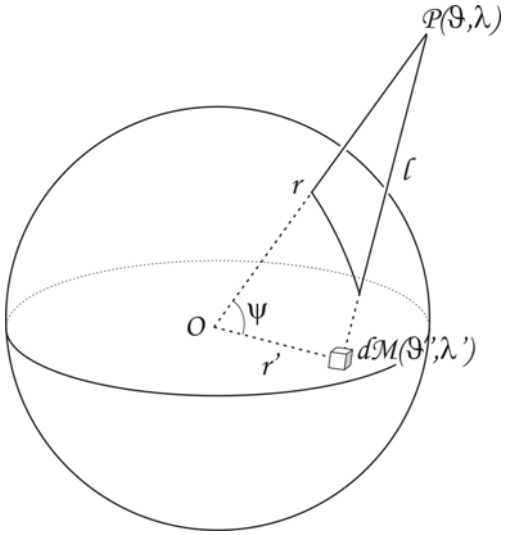

Figure 11.1: Reference geometry for the expansion of the gravitational potential at P.

Since the mass element is (compare to chapter 9.2 (9-10)):

$$dM = \rho r'^2 \sin\vartheta' \, dr' d\vartheta' d\lambda' \tag{11-30}$$

the coefficients A_{nm} and B_{nm} become:

$$\begin{aligned} A_{n0} &= G\iiint_{body} r'^n P_n(\cos\vartheta') dM \\ A_{nm} &= 2\frac{(n-m)!}{(n+m)!} G\iiint_{body} r'^n C_{nm}(\vartheta',\lambda') dM \\ B_{nm} &= 2\frac{(n-m)!}{(n+m)!} G\iiint_{body} r'^n S_{nm}(\vartheta',\lambda') dM \end{aligned} \tag{11-31}$$

11.4.1 Moments of Inertia

The first few harmonics C_{nm} and S_{nm} can be interpreted with simple mechanics. They read in Cartesian coordinates:

$$\begin{aligned} C_{00} &= 1 & S_{00} &= 0 \\ C_{10} &= \frac{z'}{r'} & S_{10} &= 0 \\ C_{11} &= \frac{x'}{r'} & S_{11} &= \frac{y'}{r'} \\ C_{20} &= \frac{-x'^2 - y'^2 + 2z'^2}{2r'^2} & S_{20} &= 0 \\ C_{21} &= \frac{3x'z'}{r'^2} & S_{21} &= \frac{3y'z'}{r'^2} \\ C_{22} &= \frac{3x'^2 - 3y'^2}{r'^2} & S_{22} &= \frac{6x'y'}{r'^2} \end{aligned} \tag{11-32}$$

Substituting these functions into the expressions for A_{nm} and B_{nm}, they yield:

$$
\begin{aligned}
A_{00} &= G\iiint_{body} dM = GM \\
A_{10} &= G\iiint_{body} z'dM \\
A_{11} &= G\iiint_{body} x'dM & B_{11} &= G\iiint_{body} y'dM \\
A_{20} &= \frac{G}{2}\iiint_{body}\left(-x'^2 - y'^2 + 2z'^2\right)dM \\
A_{21} &= G\iiint_{body} x'z'dM & B_{21} &= G\iiint_{body} y'z'dM \\
A_{22} &= \frac{G}{4}\iiint_{body}\left(x'^2 - y'^2\right)dM & B_{22} &= \frac{G}{2}\iiint_{body} x'y'dM
\end{aligned}
\qquad (11\text{-}33)
$$

It is known from mechanics that

$$
\xi = \frac{1}{M}\iiint x'dM \qquad \eta = \frac{1}{M}\iiint y'dM \qquad \varsigma = \frac{1}{M}\iiint z'dM \qquad (11\text{-}34)
$$

are the rectangular coordinates of the centre of gravity. If the origin of the coordinate system coincides with the centre of gravity, all first-degree terms in the spherical harmonic expansion vanish!

The moments of inertia *A*, *B*, *C* can be expressed through:

$$
\begin{aligned}
A &= \iiint\left(y'^2 + z'^2\right)dM \\
B &= \iiint\left(z'^2 + x'^2\right)dM \\
C &= \iiint\left(x'^2 + y'^2\right)dM
\end{aligned}
\qquad (11\text{-}35)
$$

Furthermore, the products of inertia *F*, *G*, *H* are defined as:

$$
F = \iiint y'z'dM \qquad G = \iiint z'x'dM \qquad H = \iiint x'y'dM \qquad (11\text{-}36)
$$

They are zero if the coordinate axes coincide with the principal axes of inertia. Since the *z*-axis of a body is usually identical with the mean rotational axis, which coincides with the axis of maximum inertia *C*, the products of inertia *F* and *G* must vanish, respectively all harmonics of degree 2 and order 1. For a spheroidal body the term B_{22}, which is proportional to the product of inertia *H*, would vanish as well.

The expansion of the gravitational potential *V* up to the second degree in Cartesian coordinates can now be written as:

$$
V = \frac{GM}{r} + \frac{G}{2r^5}\left[(B + C - 2A)x^2 + (C + A - 2B)y^2 + (A + B - 2C)z^2\right] \qquad (11\text{-}37)
$$

11.4.2 Mass Functions

In connection with satellite dynamics, the potential V is often written in the form:

$$V = \frac{GM}{r}\left\{1 - \sum_{n=1}^{\infty}\sum_{m=0}^{n}\left(\frac{R}{r}\right)^n \left[J_{nm}C_{nm}(\vartheta,\lambda) + K_{nm}S_{nm}(\vartheta,\lambda)\right]\right\} \tag{11-38}$$

where R is the (mean) equatorial radius of the gravitating body. Taking into account the above mentioned assumptions, the summation actually begins with $n = 2$. For $n \neq 0$ the following relations exist:

$$\begin{aligned} A_{nm} &= -GMR^n J_{nm} \\ B_{nm} &= -GMR^n K_{nm} \end{aligned} \tag{11-39}$$

J_{nm} and K_{nm} are the so-called mass functions (or moments of gravitation). They can be related to the moments and products of inertia and stated as:

$$\begin{aligned} J_{10} &= J_{11} = K_{11} = 0 \\ J_{20} &= \frac{1}{R^2 M}\left[C - \frac{1}{2}(A+B)\right] \\ J_{21} &= K_{21} = 0 \\ J_{22} &= \frac{A-B}{4R^2 M} \qquad\qquad K_{22} = -\frac{H}{2R^2 M} \end{aligned} \tag{11-40}$$

The second degree mass coefficients are also called “quadrupole moments of gravitation”. For $m = 0$ they describe the flattening of the body; terms of higher degree contribute to a better adjustment. Mass coefficients of second order take into consideration the non-spheroidal (e.g. 3-axial) shape. Furthermore, the coefficients can be interpreted with respect to the mass distribution within the body. But as stated earlier, a uniquely determination cannot be achieved.

Coefficients of higher degree can be neglected for larger distances; for planetary distances even the first term of the gravitational potential, which represents the potential of a point mass, is generally sufficient.

11.4.3 Gravitational Disturbances in Cartesian Coordinates

In order to e.g. calculate the trajectory of a spacecraft influenced by a nearby gravitating body, the gravitational disturbances need to be derived in Cartesian coordinates and implemented into e.g. a numerical integration method. For this purpose the gravitational potential V can be written as:

$$V = \frac{GM}{r} + T \tag{11-41}$$

where T denotes the disturbed potential. The gradient of V is obtained by:

$$\frac{\partial V}{\partial r} = -\frac{GM}{r^2} + \frac{\partial T}{\partial r} \tag{11-42}$$

The disturbed acceleration $\ddot{\vec{x}}_i^d$ of the spacecraft in an inertial coordinate system (index *i*) is given through [31]:

$$\ddot{\vec{x}}_i^d = \left(\frac{\partial T}{\partial x_i}, \frac{\partial T}{\partial y_i}, \frac{\partial T}{\partial z_i} \right)^T \tag{11-43}$$

If *T* is defined within a body-fixed coordinate system (index *B*) the derivatives cannot be derived directly.

At first, the acceleration vector $\ddot{\vec{x}}_B^d$ within the local system has to be calculated and later transformed into the inertial system:

$$\ddot{\vec{x}}_B^d = D\nabla T \qquad \ddot{\vec{x}}_i^d = R^T \ddot{\vec{x}}_i^d \tag{11-44}$$

where

$$\ddot{\vec{x}}_B^d = \begin{pmatrix} \frac{\partial T}{\partial x_B} \\ \frac{\partial T}{\partial y_B} \\ \frac{\partial T}{\partial z_B} \end{pmatrix}, \quad D = \begin{pmatrix} \frac{\partial r}{\partial x_B} & \frac{\partial \vartheta}{\partial x_B} & \frac{\partial \lambda}{\partial x_B} \\ \frac{\partial r}{\partial y_B} & \frac{\partial \vartheta}{\partial y_B} & \frac{\partial \lambda}{\partial y_B} \\ \frac{\partial r}{\partial z_B} & \frac{\partial \vartheta}{\partial z_B} & \frac{\partial \lambda}{\partial z_B} \end{pmatrix} \quad \text{and} \quad \nabla T = \begin{pmatrix} \frac{\partial T}{\partial r} \\ \frac{\partial T}{\partial \vartheta} \\ \frac{\partial T}{\partial \lambda} \end{pmatrix} \tag{11-45}$$

The first derivatives of the disturbed potential are stated as:

$$\begin{aligned} \frac{\partial T}{\partial r} &= GM \sum_{n=2}^{\infty} -(n+1) \frac{R^n}{r^{n+2}} \sum_{m=0}^{n} \left(J_{nm} \cos m\lambda + K_{nm} \sin m\lambda \right) P_{nm}(\cos \vartheta) \\ \frac{\partial T}{\partial \vartheta} &= GM \sum_{n=2}^{\infty} \frac{R^n}{r^{n+1}} \sum_{m=0}^{n} \left(J_{nm} \cos m\lambda + K_{nm} \sin m\lambda \right) \frac{\partial P_{nm}(\cos \vartheta)}{\partial \vartheta} \\ \frac{\partial T}{\partial \lambda} &= GM \sum_{n=2}^{\infty} \frac{R^n}{r^{n+1}} \sum_{m=0}^{n} m\left(- J_{nm} \sin m\lambda + K_{nm} \cos m\lambda \right) P_{nm}(\cos \vartheta) \end{aligned} \tag{11-46}$$

For further reference (chapter 8.1.1), the quadrupole acceleration a_2 in Cartesian coordinates is given:

$$a_2 = \frac{3}{2} \frac{G}{r^6} \left[x^2 (2A - B - C) + y^2 (-A + 2B - C) + z^2 (-A - B + 2C) \right] \tag{11-47}$$

11.5 APPLICATION

With respect to this work the ellipsoidal coordinates and scale factors (chapter 9.4) are applied in order to obtain the individual mass elements *dM* of a body. Their effect on the Neumann points (lying on a circumscribed sphere with radius equal to the body's major axis *a*) gives the body's potential of gravitation, which leads to the derivation of the moments of gravitation (mass coefficients) by the second method of Neumann. Based on these coefficients the gravitational disturbances (accelerations) acting on a spacecraft can be calculated and thus its trajectory. The approach is described in the following chapters.

12 'GRASP'

The main focus of this work lies in the derivation of Amalthea's gravity field, based on different interior models of the moon (chapter 13), which have in return a direct impact on a spacecraft trajectory (chapter 14). In order to carry out the required calculations the computer programme GRASP (**Gra**vity Field of a Planetary Body and its Influence on a **Sp**acecraft Trajectory) has been developed. GRASP is coded in the computer language Borland Delphi Professional, Version 3.0, the Windows-based version of Borland Pascal, to ensure an user-friendly product.

With GRASP it is possible to:

- derive the volume of any spherical, spheroidal or ellipsoidal body,
- calculate the potential of gravitation, the mass coefficients, and the moments of inertia of these bodies, and
- analyse the effect of the body's gravity field on a spacecraft trajectory.

All these aspects are taken care through various numerical integration methods.

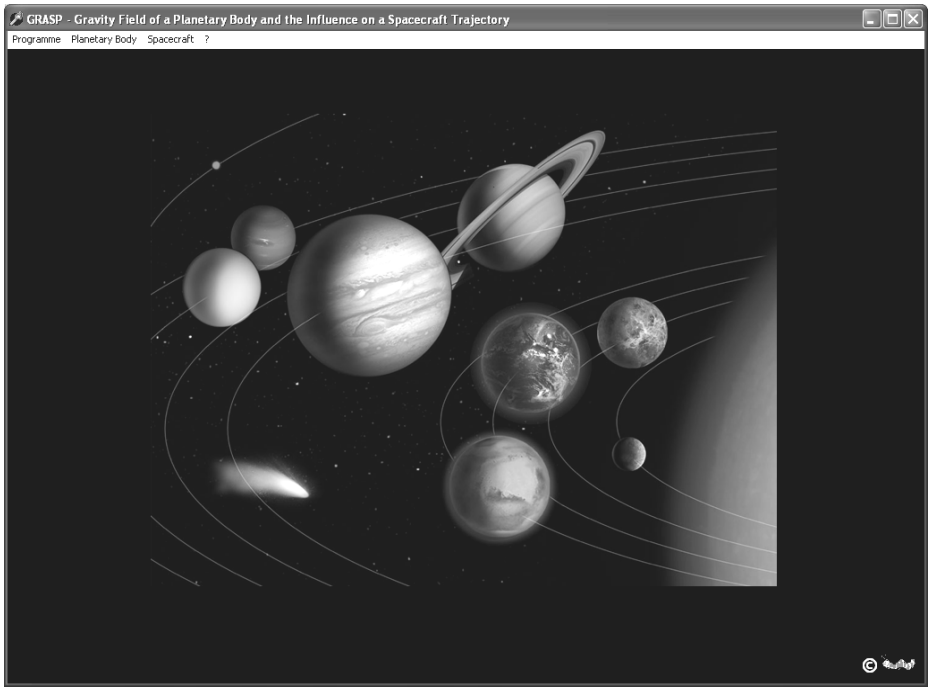

Figure 12.1: GRASP – start page.

The calculation times for GRASP given in the following sections refer to a notebook with a 1.6 GHz Intel Pentium processor and 504 MB RAM.

12.1 Volume of a Planetary Body

GRASP provides options to calculate the volume of a body through a spheroidal or ellipsoidal approach, which is derived by the summation of infinitesimal volume elements $d\tau$ (chapters 9.3 and 9.4, respectively equations (9-18) and (9-24)); the smaller the elements the better the volume approximation – selectable through the number of sections that indicate the thickness of the spheroidal/ellipsoidal shells. The body axes have to be provided through a data file ('DataBody.txt'), as well as the rotational period of the body that is needed for the calculation of a spacecraft trajectory (Figure 12.2). Furthermore, the density ρ or the mass M

of the body can be entered, which is essential for supplementary computations of the gravity field.

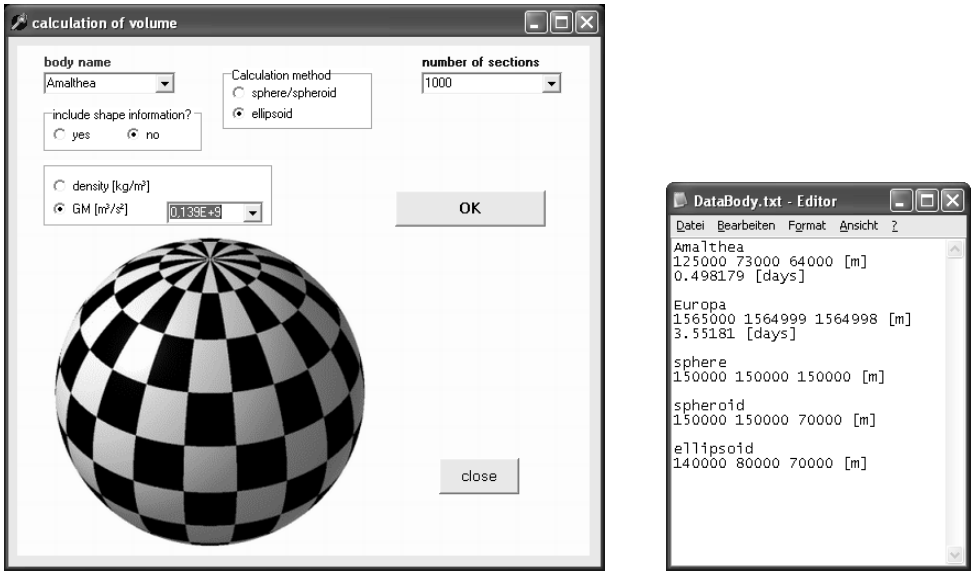

Figure 12.2: GRASP – data input for volume calculation.

The coded algorithms are stated in Appendix F.1.

12.1.1 Spheroidal approach

In addition to the above mentioned inputs the spheroidal calculation of the infinitesimal volume element requires the length of the longitudinal and latitudinal steps (Figure 12.3).

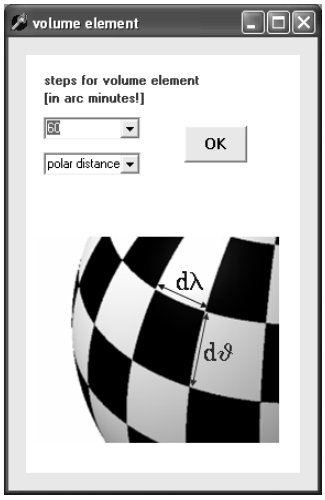

Figure 12.3: GRASP – data input for volume element.

In order to optimise computation time and output accuracy, the volume calculation was tested through various input options (number of sections, longitudinal and latitudinal steps) and compared to the reference volume of a sphere, respectively spheroid:

$$\tau = \frac{4}{3} r^3 \pi \qquad \tau = \frac{4}{3} a^2 c \pi \tag{12-1}$$

with r being the radius of the sphere, respectively a and c the axes of the spheroid.

The results for a spheroid of axes a = 125 km and c = 64 km, which stand for any spheroid, are shown in Figure 12.4. The implementation of more sections gives a better volume approximation, although no significant improvement can be derived with more than 1000 sections. In comparison to 5° steps slightly better values are obtained for 1° steps; steps of 30' and less give no upgrading but increase the calculation time. It is therefore recommended to use 1° steps and 1000 sections for the calculation of the volume, which results in an accuracy of about ±0.04 %. The computation time on the above mentioned notebook amounts to approximately one minute.

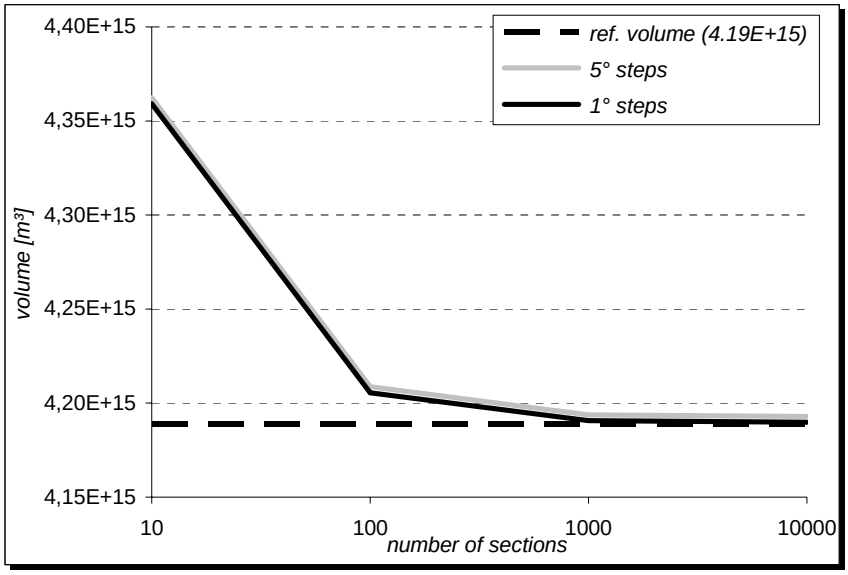

Figure 12.4: Volume approximation by variation of input parameters.

12.1.2 Ellipsoidal approximation

Most of the smaller bodies in our solar system cannot be approximated well by a sphere or spheroid, but with an ellipsoid, as it is the case with Jupiter's moon Amalthea. It is therefore necessary to calculate the volume with means of ellipsoidal coordinates.

In order to maximise the output accuracy, a similar test as for the spheroidal approach was carried out, comparing the output volume to the reference volume of an ellipsoid with same axes a, b, and c:

$$\tau = \frac{4}{3} abc\pi \tag{12-2}$$

The results for an ellipsoid of axes a = 125 km, b = 73 km and c = 64 km (values for Amalthea), which stand for any ellipsoid, are shown in Figure 12.5. As expected, the implementation of more sections gives a better volume approximation; the accuracy for 5000 sections results to roughly ±1.2 %. But because of the complex algorithms for this approach, the computation time amounts to ~24 hours (!) for 5000 sections on the above mentioned notebook, which is not feasible for further calculations. It is therefore recommended to use 500 or 1000 sections, resulting in a volume accuracy of better than ±4 %, but a calculation time of only one, respectively twelve minutes.

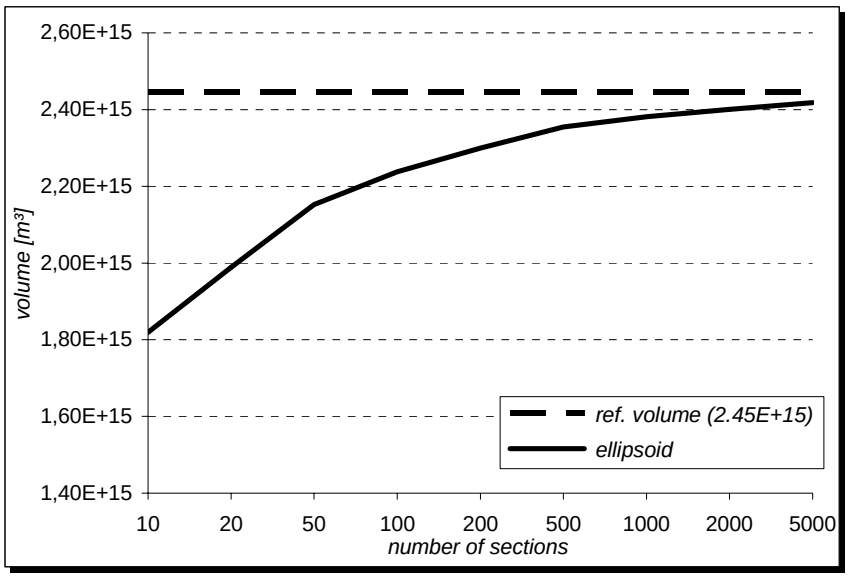

Figure 12.5: Volume approximation for an ellipsoid.

12.1.3 Shape implementation

For very irregular bodies not even an ellipsoidal volume approximation is sufficient, which actually would be the case for Amalthea. As mentioned in chapter 4.3 shape data of the moon exist (Figure 12.6) that can be implemented into GRASP. Based on the ellipsoidal approach, the coordinates of the current volume element are calculated, transferred into polar coordinates and the radius of this point compared to the radius of the shape model. If latter is smaller, the volume element is not added to the total volume.

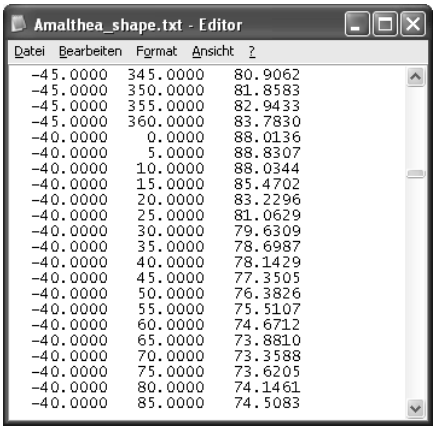

Figure 12.6: Data file with shape information of body (latitude, longitude, and radius).

This method lacks precision, but for a first order assessment of its feasibility the approach is sufficient. In order to analyse the method's accuracy, the shape information of various ellipsoids was implemented and tested in comparison to the normal ellipsoidal approximation.

As the ellipsoidal axes of the data file are used to give a reference ellipsoid, the approach does not take into consideration any volume elements which might lie outside. It would therefore be obvious to apply a larger reference ellipsoid. Unfortunately, a larger reference ellipsoid involves larger volume elements, thus a poor approximation and a too large volume, as can be seen in Figure 12.7: the task was to derive the volume of an ellipsoid with axes a = 125 km, b = 73 km and c = 64 km, which was given as shape data in 5° steps. The red line gives the reference volume as stated in the previous section. The blue line refers to a reference ellipsoid

with the same axes – demonstrating the same volume as derived through the normal ellipsoidal approximation. The other two lines denote larger reference ellipsoids and thus larger volumes.

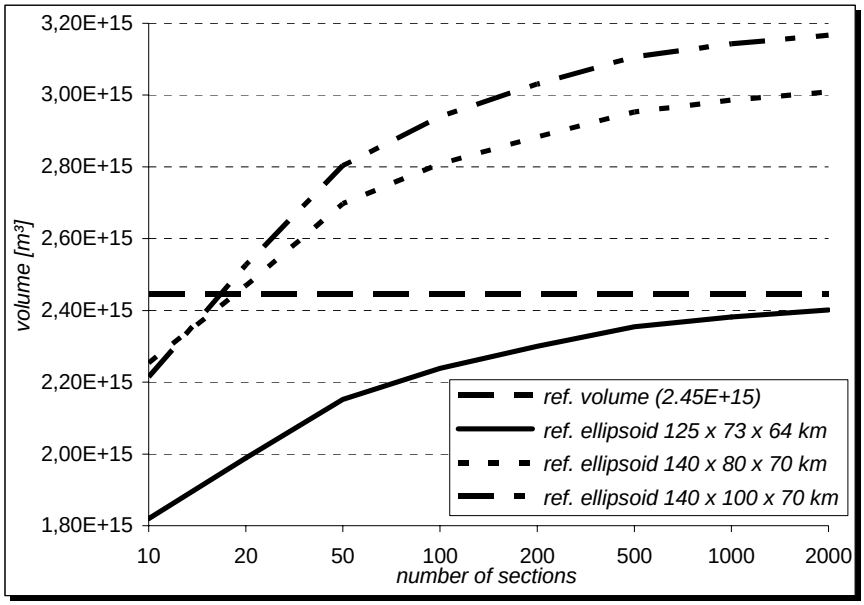

Figure 12.7: Shape implementation with various reference ellipsoids.

The computation times for this approach are already enormous, and even higher for 1° step shape data, which do not give better values.

Consequently it can be stated that the above mentioned method as such gives no valuable results. A more precise derivation of volume element coordinates and comparison algorithms would only increase computation time and was therefore not considered. There are of course different approaches for including the shape data, e.g. [11], but they cannot be exploited for the calculation method of the gravity field used in this work.

However, one valuable conclusion of the tests can be made for the volume of Amalthea (Figure 12.8): it is certainly smaller than the one derived by its axis, although the exact value cannot be determined. The blue line refers to a reference ellipsoid with axes a = 125 km, b = 73 km and c = 64 km (similar to Figure 12.7). Because of Amalthea's irregular shape, the reference ellipsoid does not cover the whole body – it is not fully filled and parts of the moon lie outside, which are thus not calculated. The results expectedly show a smaller volume compared to Figure 12.7. The yellow line denotes a larger reference ellipsoid that entirely covers the moons shape but, concluding from the previous calculations, gives a too large volume. Amalthea's actual volume must thus amount to a value between those two lines. This result lies well within the volume accuracy derived by P. Thomas (chapter 4.3).

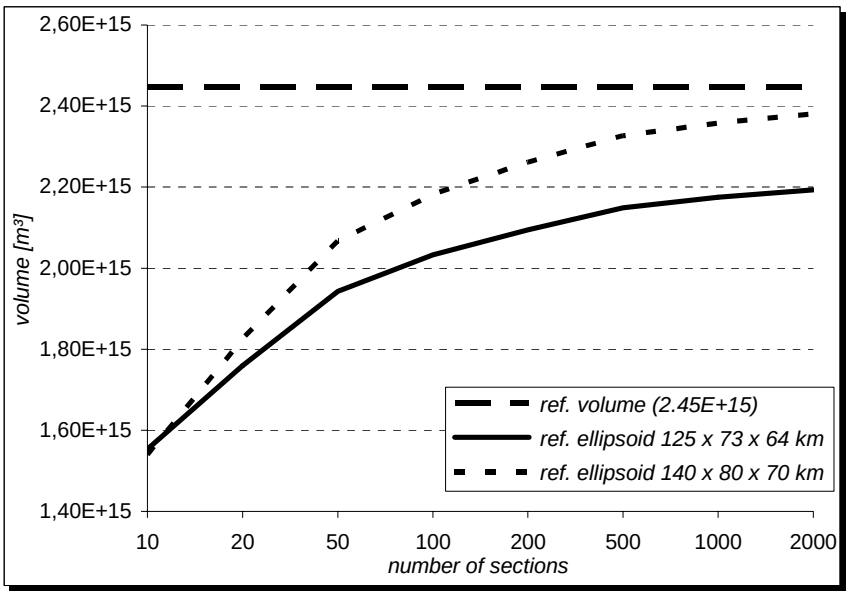

Figure 12.8: Amalthea's shape based on different reference ellipsoids.

12.1.4 Conclusions and Data Output

Considering the above results and conclusions for the ellipsoidal approach and shape implementation, the fact that Amalthea's shape data is given only in an interval of 5°, and the computation times, the volume approximation for Amalthea with the ellipsoidal approach is sufficient using 500 sections. These volume calculations serve as a basis for the further derivation of the body's gravity field.

Sample output data files are given in Figure 12.9:

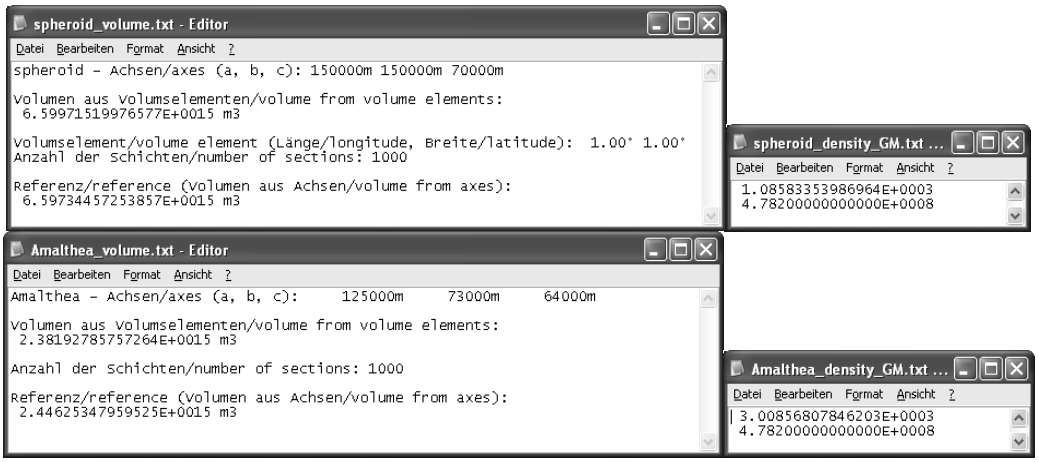

Figure 12.9: GRASP – data output for volume calculations.

12.2 Gravity Field

The determination of the mass coefficients for a planetary body is implemented in GRASP through the second method of Neumann (chapter 11.3.1). Depending on the degree of the gravity field expansion the correct input for the data file of the Neumann coefficients needs to be given (e.g. 'Neumann6.txt', Figure 12.10). Based on the Neumann coefficients *t* and the degree of expansion GRASP computes the coordinates of the required Neumann points (lying on a circumscribed sphere with radius equal to the body's major axis *a*) in which the potential of gravitation will be calculated.

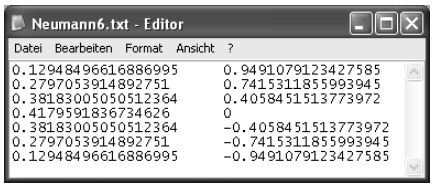

Figure 12.10: GRASP – data input Neumann coefficients a and t.

In addition to the Neumann data file the number of sections needs to be indicated, as well as in case of a heterogeneous body the number of layers, their thickness and mean density (Figure 12.11). The thickness and mean density of the outer layer result from the body's shape and overall mean density; latter has been derived in the course of the volume calculation.

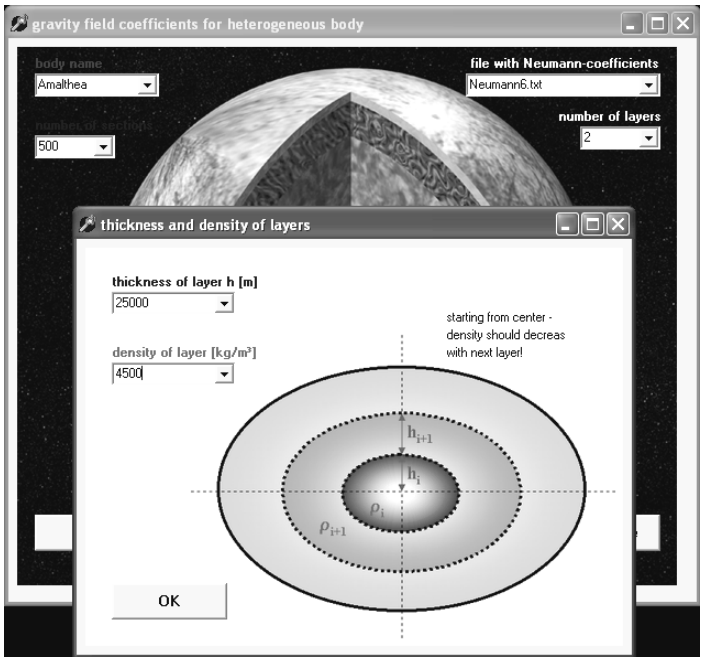

Figure 12.11: GRASP – data input for gravity field determination (heterogeneous body).

The potential of each Neumann point $V(\vartheta,\lambda)$ is derived through the summation of the effect of each infinitesimal mass element $dM(\vartheta',\lambda')$:

$$V(\vartheta,\lambda) = \sum dV(\vartheta',\lambda') = G\sum \frac{dM(\vartheta',\lambda')}{l} = G\sum \frac{d\tau(\vartheta',\lambda')\rho}{l} \qquad (12\text{-}3)$$

with l being the distance between P and dM (compare with Figure 11.1) and ρ the density of the current layer.

Thus the values/functions needed for the implementation of the second method of Neumann are given; and based on the coefficients of the spherical expansion A_{nm}, B_{nm} (11-39) the mass functions of gravitation can be calculated:

$$J_{nm} = -\frac{a}{GM}A_{nm} \qquad K_{nm} = -\frac{a}{GM}B_{nm} \qquad (12\text{-}4)$$

Furthermore, GRASP uses the same approach of summation to derive the moments of inertia (chapter 11.4.1). The computation time for a spheroidal approach (1° steps, 1000 sections)

amounts to 30 minutes, for an ellipsoidal approach (500 sections) already to 8 hours, respectively 15 hours depending on the degree of the coefficients.

12.3 Trajectory

GRASP offers two options to calculate the trajectory of a spacecraft (s/c) influenced by a nearby body, provided that a starting point (e.g. closest approach c/a) and a starting velocity of the spacecraft are given:

- ⋆ s/c trajectory in a local, body-fixed coordinate system
- ⋆ s/c trajectory in the inertial J2000, body centred coordinate system

For the latter the coordinates of three points (e.g. planets) need to be known in both inertial and local coordinate systems (Figure 12.12), in order to derive the rotation angles ε_x, ε_y, ε_z, which are needed for the transformation between these two coordinate systems.

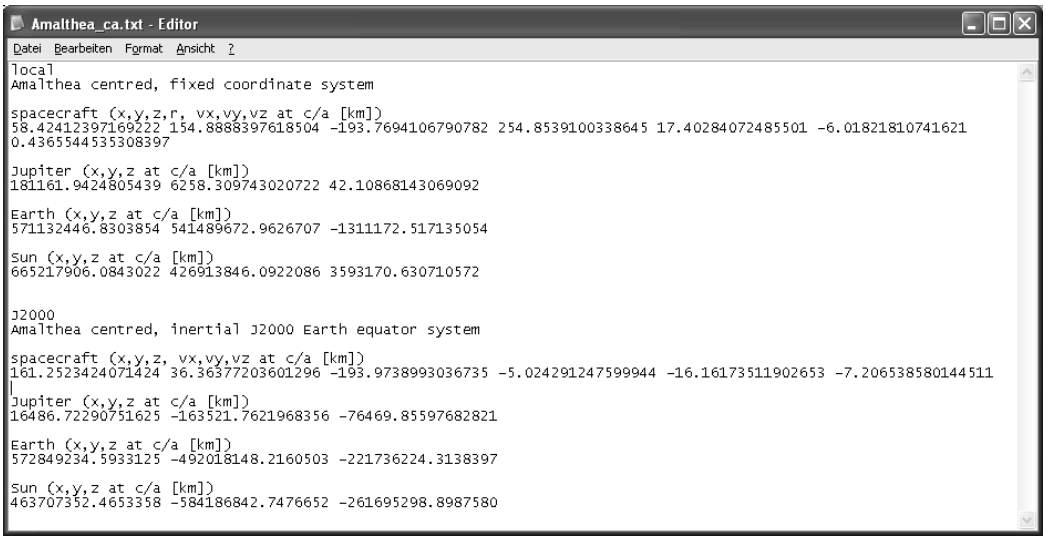

Figure 12.12: Data input for spacecraft coordinates and velocity at starting point.

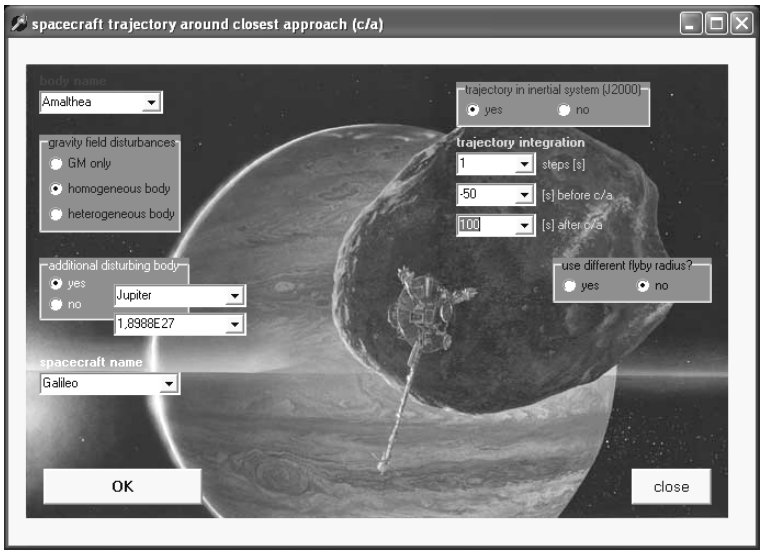

Figure 12.13: GRASP – data input for trajectory calculation.

Further input options include (Figure 12.13):

- ⋆ the main body's gravity field (point mass only, homogeneous respectively heterogeneous interior), based on the calculations described in the previous section
- ⋆ an additional nearby disturbing body, treated as point mass
- ⋆ the integration steps for the s/c trajectory and the time interval
- ⋆ a different flyby radius as stated in the input file

12.3.1 Algorithms

The gravity field of a body influences the path of a spacecraft permanently. Depending on the current position of the spacecraft within the body's local coordinate system the gravity field disturbances accelerate or decelerate the spacecraft. Based on the equations in chapter 11.4.3 GRASP determines the disturbing accelerations $\ddot{\vec{x}}_B^d$ and, if indicated, adds an additional gravitational tug from another nearby body.

If the calculations are derived within an inertial coordinate system (index *i*), the accelerations need to be transformed into the inertial system ($\ddot{\vec{x}}_i^d$, see chapter 11.4.3 for the detailed expressions). The body rotation of Amalthea ω_z is thereby taken into consideration as supplement to ε_z.

The computed algorithms for the above mentioned expressions are stated in Appendix F.2 and F.3.

The spacecraft trajectory is calculated through the numerical integration method of Runge-Kutta (chapter 6.3). As this method can only be used to solve differential equations of first order, but the equations of motion are of second order, the method needs to be applied twice within one step. The two differential equations of motion read:

$$\dot{\vec{x}} = v \qquad\qquad \ddot{\vec{x}} = \dot{\vec{v}} = -\frac{GM}{r^3}\vec{x} - \ddot{\vec{x}}^d \tag{12-5}$$

And thus the expanded expressions for the Runge-Kutta:

$$\begin{array}{lll}
\vec{x}_1 = \vec{x}_j & \vec{k}_1 = h\cdot\vec{v}_j = h\cdot\vec{v}_1 & \vec{k}_1^v = h\cdot\left(-\dfrac{GM}{r_1^3}\vec{x}_1 - \ddot{\vec{x}}_j^d\right) \\
\vec{x}_2 = \vec{x}_1 + \dfrac{1}{2}\vec{k}_1 & \vec{k}_2 = h\cdot\left(\vec{v}_1 + \dfrac{1}{2}\vec{k}_1^v\right) & \vec{k}_2^v = h\cdot\left(-\dfrac{GM}{r_2^3}\vec{x}_2 - \ddot{\vec{x}}_2^d\right) \\
\vec{x}_3 = \vec{x}_1 + \dfrac{1}{2}\vec{k}_2 & \vec{k}_3 = h\cdot\left(\vec{v}_1 + \dfrac{1}{2}\vec{k}_2^v\right) & \vec{k}_3^v = h\cdot\left(-\dfrac{GM}{r_3^3}\vec{x}_3 - \ddot{\vec{x}}_3^d\right) \\
\vec{x}_4 = \vec{x}_1 + \vec{k}_3 & \vec{k}_4 = h\cdot\left(\vec{v}_1 + \vec{k}_4^v\right) & \vec{k}_4^v = h\cdot\left(-\dfrac{GM}{r_4^3}\vec{x}_4 - \ddot{\vec{x}}_4^d\right)
\end{array} \tag{12-6}$$

with $\vec{x}_j$ denoting the starting point (e.g. closest approach), $\vec{v}_j$ its velocity, $\ddot{\vec{x}}_j^d$ the disturbing acceleration, and *h* the integration step in e.g. seconds.

Coordinates and velocity of the next trajectory point read:

$$\vec{x}_{j+1} = \vec{x}_j + \frac{1}{6}\left(\vec{k}_1 + 2\vec{k}_2 + 2\vec{k}_3 + \vec{k}_4\right)$$
$$\vec{v}_{j+1} = \vec{v}_j + \frac{1}{6}\left(\vec{k}_i^{\,v} + 2\vec{k}_2^{\,v} + 2\vec{k}_3^{\,v} + \vec{k}_4^{\,v}\right) \qquad (12\text{-}7)$$

Part IV
Amalthea Models:
Gravity and Trajectory

13 MODEL CALCULATIONS FOR AMALTHEA

In order to derive the mass coefficients J_{nm} and K_{nm} for Amalthea, reasonable models for the interior structure of the moon need to be defined. Based on the current controversial knowledge of Amalthea's composition (chapters 4.4 and 8.2.1) and the vague interpretations of the moon's formation, two basic model assumptions are taken into account within the present work. They have been analysed with respect to each other, serve as a basis for further interpretations of Amalthea's interior and have been implemented into the analysis of a nearby spacecraft trajectory (chapter 14).

13.1 EXPLANATIONS

The two basic model types for Amalthea are based on two different assumptions of the moon's mass (Table 13.1). A first model applies the GALILEO pre-flyby hypothesis about the moon's mean density, respectively mass (M = 7.167 x 10^{18} kg), considering that Amalthea has most likely accreted during the Jovian system formation. The second type takes into account the post-flyby data evaluation and thus a mass of only M = 2.083 x 10^{18} kg, implying that the moon is an object with high porosity and probably captured.

	assumption	*mean density (ρ_m)*	*mass (M)*	*GM*
type I (pre-flyby)	low porosity body, most likely accreted during the Jovian system formation	~ 3000 kg/m³	7.167 x 10^{18} kg	4.782 x 10^{8} m³/s²
type II (post-flyby)	high porosity body, probably captured	860 ± 60 kg/m³	2.083 x 10^{18} kg	1.39 x 10^{8} m³/s²

Table 13.1: Mean density model assumptions for Amalthea.

Based on these two basic mean density (or mass) types, interior structure models of Amalthea have been generated (Figure 13.1). The standard model *A* describes a homogeneous body interior and thus shows no differentiation into core and mantle, which is likely to apply for both basic types. Model *B* consists of a two-layer interior with a dense core that can only be related to the higher mass (pre-flyby) type *I*. A third model *C* shows as well a two-layer interior, but highlights a loose inner agglomeration and a regolith layer – a scenario expected for the low mass (post-flyby) type *II*.

Because of Amalthea's small dimensions, no three- or higher layer models are taken into consideration for further analysis.

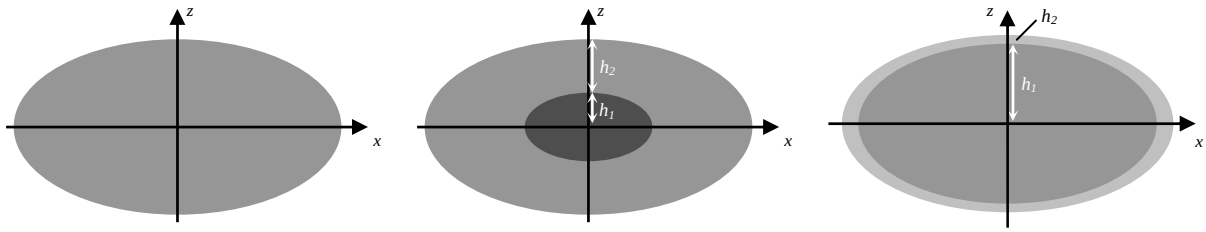

model A – homogeneous

model B – heterogeneous, 2-layer
h_1 ~ 25 km, h_2 ~ 39 km

model C – heterogeneous, 2-layer
h_1 ~ 63 km, h_2 ~ 1 km

Figure 13.1: Interior structure models for Amalthea.

The interpretations of the interior geology of Amalthea with respect to the stated types and models are given in the following sections; as well as the expansions of the gravity field for

the different interior models of Amalthea, which have been derived up to degree and order 6. For clarification it should be noted that the computed mean densities of the models differ slightly from the above due to the body volume approximation (chapter 12.1).

With reference to the expansion of the potential into spherical harmonics (chapter 11.4), and the definition of the moments and products of inertia, the origin of the local coordinate system lies in Amalthea's centre of gravity. Furthermore, the coordinate axes are supposed to coincide with the principal axes of inertia, and the *z*-axis of the moon is identical with the mean rotational axis. Consequently, the mass coefficients of degree 2 and order 1 vanish, as well as all mass coefficients K_{nm}. Because the volume of Amalthea is derived through an ellipsoidal approach (no shape data is implemented with reference to chapter 12.1.4), which represents equator symmetry, no odd degree mass coefficients exist. Furthermore, based on the ellipsoidal approach, symmetry is given with respect to the *xz*-plane and thus all odd order mass coefficients vanish as well.

13.2 HOMOGENEOUS CASES

As a first step for the calculation of Amalthea's gravity field, respectively moments of gravitation (or mass coefficients), the homogeneous model *A* has been applied for both basic mass types of the moon (Table 13.2).

mass coefficients (moments of gravitation)			*moments of inertia [kg m²]*	
	not normalised	*normalised*	*model I/A*	
J_{20}	0.08403024	0.03757947	*A*	1.34785×10^{28}
J_{22}	-0.03408576	-0.05280543	*B*	2.86366×10^{28}
J_{40}	-0.01990302	-0.00663434	*C*	3.04198×10^{28}
J_{42}	0.00205441	0.00918760	*model II/A*	
J_{44}	-0.00021269	-0.01006645	*A*	3.91785×10^{27}
J_{60}	0.00880104	0.00244097	*B*	8.32389×10^{27}
J_{62}	-0.00041013	-0.00329676	*C*	8.84222×10^{27}
J_{64}	0.00001201	0.00317384		
J_{66}	-0.00000061	-0.00261296		

Table 13.2: Mass coefficients and moments of inertia for homogeneous models.

The mass coefficients of the two models have to be identical, differences are due to the calculation uncertainties, which as well apply for the odd order terms and the coefficients K_{nm}. J_2 defines the flattening of Amalthea, J_{22} the non-spheroidal and thus ellipsoidal shape of the moon; higher degree coefficients contribute to a better adjustment.

As its axis coincides with the body's mean rotational axis, the maximum moment of inertia *C* is of importance for the interior structure of Amalthea. For a homogeneous spherical body the reduced dimensionless moment of inertia Γ [17]

$$\Gamma = \frac{C}{M R^2} \tag{13-1}$$

equals 0.4 (*R* denoting the body's radius). Smaller values indicate a density increase towards the body's interior. Deviation from spherical shape tends to increase Γ, which is clearly the

case in Amalthea's homogeneous models, where Γ equals 0.609 (for a mean radius *R* of 83.5 km).

As mentioned in chapter 11.1, a uniquely determination of Amalthea's interior structure cannot be defined exclusively by the potential of gravitation, which is obvious by considering the variety of interpretations that can be derived from the undifferentiated (homogeneous) assumptions. A likely selection would be:

- ⋆ model I/A: $GM = 4.782 \times 10^8$ m³/s², rocky material or rock/iron mixture with $\rho_m = \rho_0 \sim 3000$ kg/m³
- ⋆ model II/A: $GM = 1.39 \times 10^8$ m³/s² and $\rho_m \sim 880$ kg/m³, which can be interpreted e.g. as:
  - rocky material or rock/iron mixture with $\rho_0 \sim 3500$ kg/m³ and porosity $\Phi \sim 0.75$ (probably demonstrating ice content and holes); the rock composition would imply that Amalthea is not a captured body but accreted during the Jovian system formation
  - carbon-rich material with $\rho_0 \sim 2000$ kg/m³ and porosity $\Phi \sim 0.55$; considering Amalthea as a captured body with interior volatile and void components

In order to get more valuable insights into Amalthea's interior structure additional information from in-situ geological or seismic measurements are needed.

13.3 HETEROGENEOUS CASES

To derive heterogeneous two layer models for Amalthea, model *B* has been applied for type *I* and model *C* for type *II*. Based on the assumptions in the previous section for the interior structure, a similar interpretation for the heterogeneous models can be made:

- ⋆ model I/B: $GM = 4.782 \times 10^8$ m³/s² ($\rho_m \sim 3000$ kg/m³), iron rich core with $\rho_1 = 4500$ kg/m³ and thus resulting in a slightly porous outer layer with $\Phi \sim 0.1$ and $\rho_2 = 2670$ kg/m³ ($\rho_0 \sim 3000$ kg/m³, rocky material or rock/iron mixture)
- ⋆ model II/C: $GM = 1.39 \times 10^8$ m³/s² ($\rho_m \sim 880$ kg/m³), agglomeration of smaller objects with properties similar to the two scenarios mentioned for model II/A (chapter 13.2):
  - interior with $\rho_1 = 870$ kg/m³ ($\rho_0 \sim 3500$ kg/m³, porosity $\Phi \sim 0.75$), and thus resulting in an outer regolith layer with $\rho_2 = 1390$ kg/m³ ($\rho_0 = 3000$ kg/m³, $\Phi \sim 0.5$)
  - interior with $\rho_1 = 870$ kg/m³ ($\rho_0 \sim 2000$ kg/m³, porosity $\Phi \sim 0.55$), outer regolith layer with $\rho_2 = 1390$ kg/m³ ($\rho_0 = 2000$ kg/m³, $\Phi \sim 0.3$)

Taking into account the latest data from GALILEO, model II/C is the most likely scenario for Amalthea, although it should be perceived with care. Data analysis of future exploration should yield more precise information about the moon's interior structure.

The properties of the gravity field for the above models are given in Table 13.3. The mass coefficients of the two models differ slightly from those of the homogeneous models, which is due to a different internal mass distribution. Latter can as well be derived from the reduced dimensionless moment of inertia Γ (13-1):

- ⋆ model I/B: Γ = 0.585 and hence smaller as the homogeneous value of 0.609, indicating a density increase towards the centre of the body
- ⋆ model II/C: Γ = 0.613 and thus larger than the homogeneous value of 0.609 due to the dense regolith layer

mass coefficients (moments of gravitation)					
model I/B			*model II/C*		
	not normalised	*normalised*		*not normalised*	*normalised*
J_{20}	0.08403304	0.03758072	J_{20}	0.08402517	0.03757720
J_{22}	-0.03408290	-0.05280100	J_{22}	-0.03408343	-0.05280182
J_{40}	-0.01999098	-0.00666366	J_{40}	-0.01987390	-0.00662463
J_{42}	0.00206005	0.00921282	J_{42}	0.00205218	0.00917765
J_{44}	-0.00021365	-0.01011177	J_{44}	-0.00021235	-0.01005041
J_{60}	0.00887681	0.00246199	J_{60}	0.00877179	0.00243286
J_{62}	-0.00041317	-0.00332121	J_{62}	-0.00040886	-0.00328661
J_{64}	0.00001209	0.00319352	J_{64}	0.00001198	0.00316455
J_{66}	-0.00000061	-0.00263046	J_{66}	-0.00000061	-0.00260569
moments of inertia [kg m²]					
model I/B			*model II/C*		
A	1.22786×10^{28}		*A*	3.97214×10^{27}	
B	2.74287×10^{28}		*B*	8.37884×10^{27}	
C	2.92128×10^{28}		*C*	8.89716×10^{27}	

Table 13.3: Mass coefficients and moments of inertia for heterogeneous models.

As the difference of the mass coefficients ($\Delta_{coefficients}$) of Amalthea's homogeneous and heterogeneous gravity field models amounts at the most to 9×10^{-5} the resulting acceleration $a_{s/c}$ acting on the spacecraft

$$a_{s/c} = \Delta_{coefficients} \frac{GM}{r^2} \qquad (13\text{-}2)$$

is less than 6.5×10^{-4} mm/s² (with a flyby radius r of 254.8 km and $GM = 4.782 \times 10^{8}$ m³/s²).

14 SPACECRAFT DATA IMPLEMENTATION AND EVALUATION

In case of availability of 2-way Doppler data for the GALILEO Amalthea flyby the moon's models derived in the previous chapter could have been implemented as a priori information into the JPL's DPODP and the analysis of the remaining Doppler residuals would have given more information on Amalthea's gravity field and thus interior structure. Because of the already mentioned non-availability of these data a reverse approach and interpretation of the existing data has been taken into consideration within the frame of this work.

As stated in chapter 8.2 the yearlong experience of the JPL Radio Science team guaranteed the analysis of the 1-way Doppler data from GALILEO's Amalthea flyby with respect to the mass of the body as well as the spacecraft's position at closest approach (c/a). Latter can be found in Appendix C. With the support of B. Kazeminejad, Space Research Institute of the Austrian Academy of Sciences, the c/a-data was conveyed to Amalthea's local coordinate system using the SPICE Toolkit. SPICE (Spacecraft, Planet, Instrument, C-matrix, Events), developed by JPL's Navigation and Ancillary Information Facility (NAIF), provides tools and data files of e.g. planetary body's ephemeris, shapes, reference frames, star catalogues, etc. for spacecraft mission evaluation, observation planning and data analysis.

In order to derive the rotation angles ε_x, ε_y, ε_z, which are needed for the transformation between the local and the inertial J2000 coordinate system (chapter 10.3), the positions of Earth, Sun and Jupiter at the time of closest approach have been transformed as well (Appendix D). For the further calculation of GALILEO's flyby trajectory, no variations in the positions of the Earth and Jupiter are considered because of the short time interval of about three minutes.

14.1 SPACECRAFT TRAJECTORIES

Based on GALILEO's state vector $(\vec{r},\vec{v})$ at the time of closest approach, the numerical integration method of Runge-Kutta (chapters 6.3 and 12.3) and the gravity field models of Amalthea derived in chapter 13, various spacecraft trajectories around closest approach have been calculated with GRASP. A sample trajectory for 100 seconds is given in Figure 14.1.

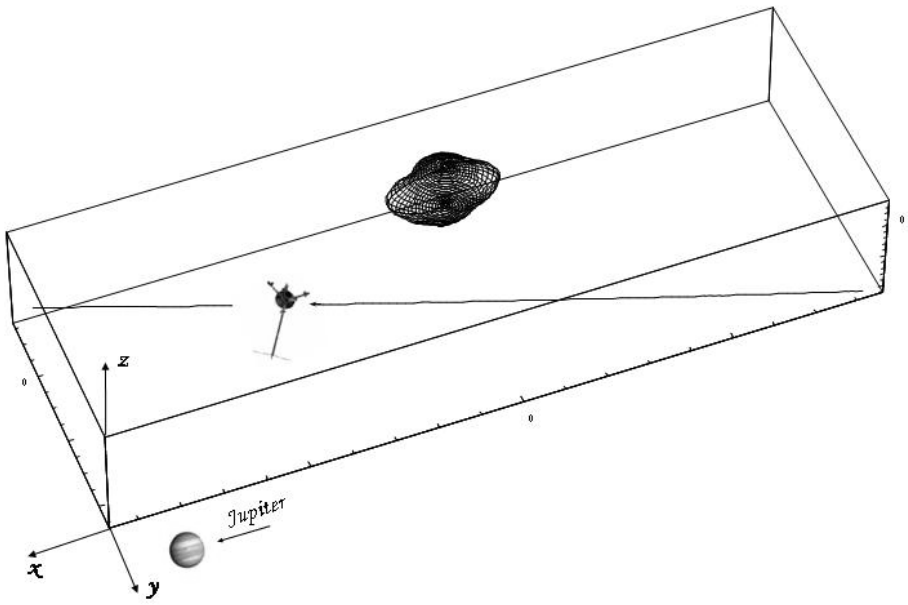

Figure 14.1: Spacecraft trajectory based on GALILEO's data at closest approach.

For further evaluations the following trajectories have been derived (Jupiter is included as additional gravitating body, the time period totals 200 seconds covering 100 seconds before and after closest approach):

- T-I/0: trajectory based on Amalthea as point mass (*GM* only, pre-flyby assumption)
- T-I/A: Amalthea homogeneous model I/A (chapter 13.2)
- T-I/B: Amalthea heterogeneous model I/B (chapter 13.3)
- T-II/0: Amalthea as point mass with post-flyby data
- T-II/A: Amalthea homogeneous model II/A (chapter 13.2)
- T-II/C: Amalthea heterogeneous model II/C (chapter 13.3)

Data which roughly represent the values of all trajectories are given in the following graphs (Figure 14.2, Figure 14.3 and Figure 14.4). The sample interval equals one second and thus the trajectory points lie one second apart.

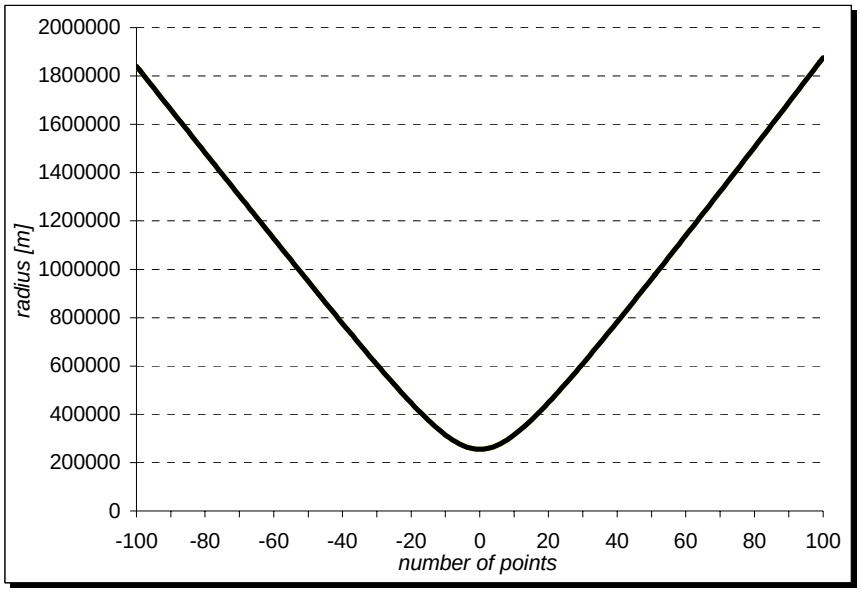

Figure 14.2: Spacecraft radius around closest approach.

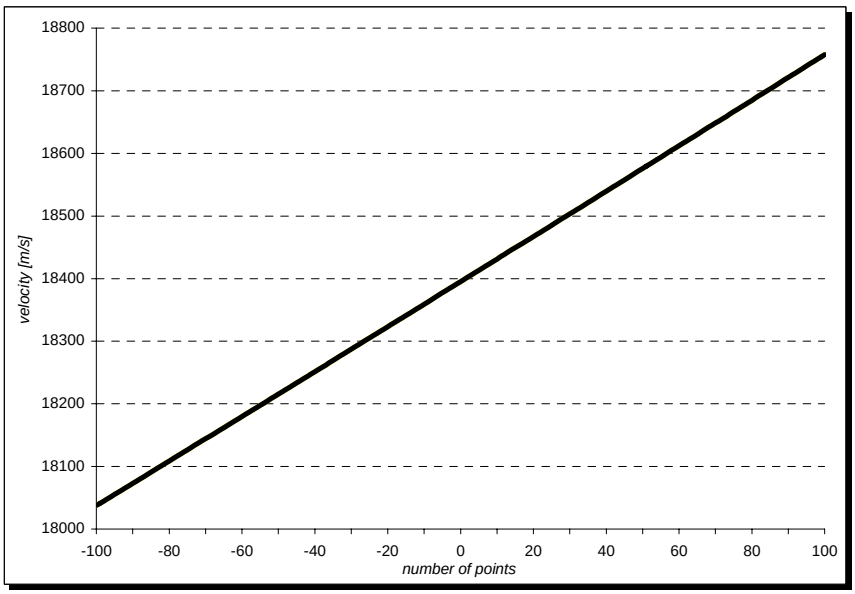

Figure 14.3: Spacecraft velocity around closest approach.

The acceleration of the spacecraft is influenced by Jupiter's gravitational tug and is based on Amalthea's gravity field derived up to degree and order 6 (chapter 13), hence includes effects from quadrupole and higher degree mass coefficients. Amalthea's gravitational force acting on the spacecraft can be clearly seen in Figure 14.4.

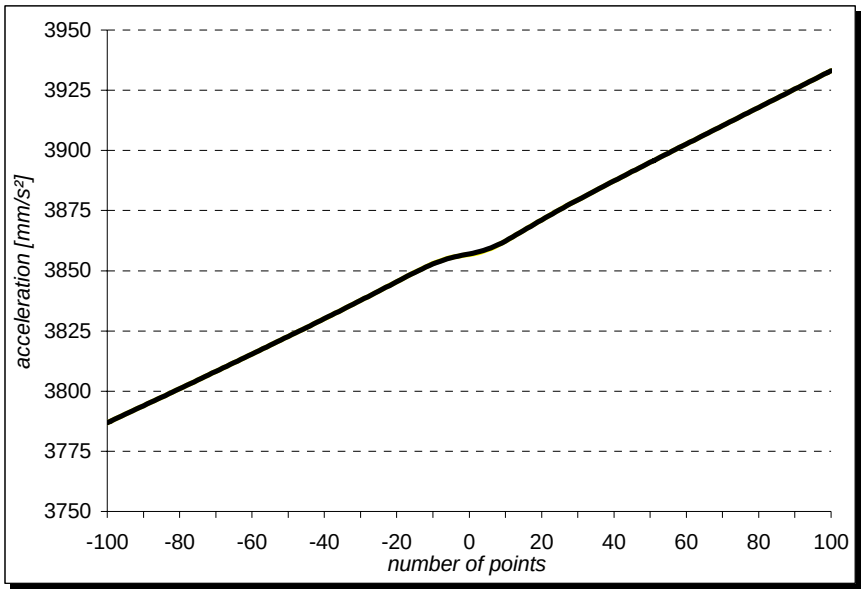

Figure 14.4: Spacecraft acceleration around closest approach.

The difference of the spacecraft's position from the two trajectories T-I/0 and T-I/A amounts to ~ 23 cm at the end of the chosen time interval (Figure 14.5), and ~ 7 cm for the trajectories T-II/0 and T-II/A. The trajectories T-I/A and T-I/B (respectively T-II/A and T-II/B) are nearly identical – they only vary in the order of a tenth of a millimetre, which was expected from the small differences in the spacecraft's acceleration (compare to chapter 13.3).

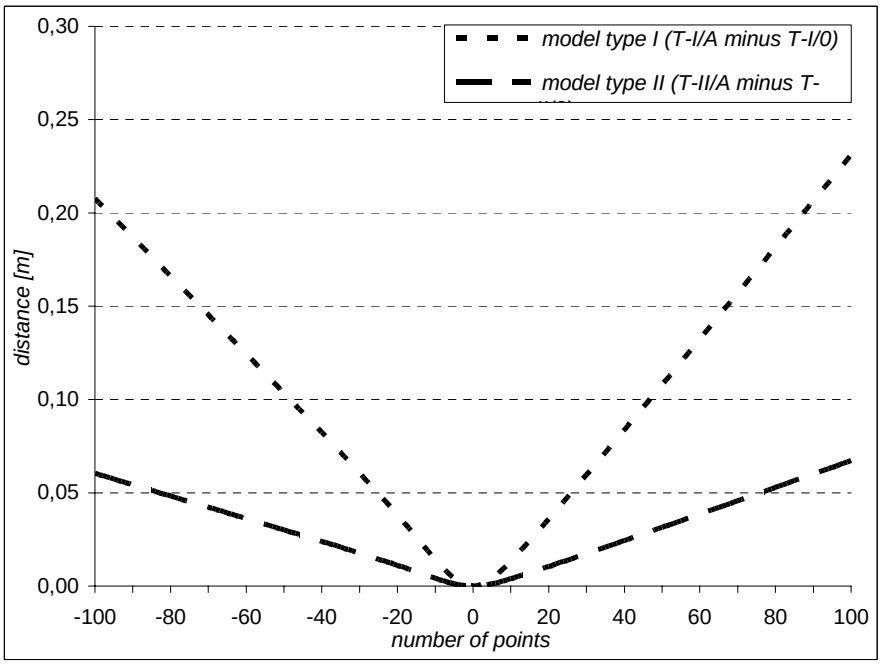

Figure 14.5: Difference of spacecraft position.

14.2 INTERPRETATION

The objective of this work, with respect to the trajectory data of GALILEO, is to get insight about the closest approach configuration regarding Amalthea's gravity field determination and thus to answer the following questions:

- ⋆ are the moments of gravitation for Amalthea undetectable with the 1-way Doppler data (hence verifying the conclusions of the Radio Science team)?
- ⋆ would the moments of gravitation have been detectable with the 2-way Doppler data?
- ⋆ would a heterogeneous mass distribution within Amalthea been detectable with 2-way Doppler-data?

In order to answer those questions and derive conclusions the various trajectories have to be analysed with respect to each other:

- ⋆ case 1: T-I/0 and T-I/A (respectively T-II/0 and T-II/A) for the mass coefficients,
- ⋆ case 2: T-I/A and T-I/B (respectively T-II/A and T-II/B) for the interior structure,

computing the spacecraft velocity (and acceleration) differences of the two trajectories, with T-I/A (respectively T-II/A) as reference trajectory. As the Doppler observables are derived on Earth the spacecraft velocity difference *dv* (and acceleration difference *da*) of the two trajectories needs to be projected on the Earth line of sight (ELoS):

$$\Delta v^{ELoS} = \frac{|\vec{r} \cdot d\vec{v}|}{|\vec{r}|} \quad \text{and} \quad \Delta a^{ELoS} = \frac{|\vec{r} \cdot d\vec{a}|}{|\vec{r}|} \tag{14-1}$$

with $\vec{r}$ being the radius vector spacecraft-Earth.

The results for case 1 are given in Figure 14.6 and Figure 14.7 and analysed in the following sections (to recall: model type *I* represents the higher mass from the pre-flyby data for Amalthea, model type *II* denotes the low mass derived after the flyby of GALILEO).

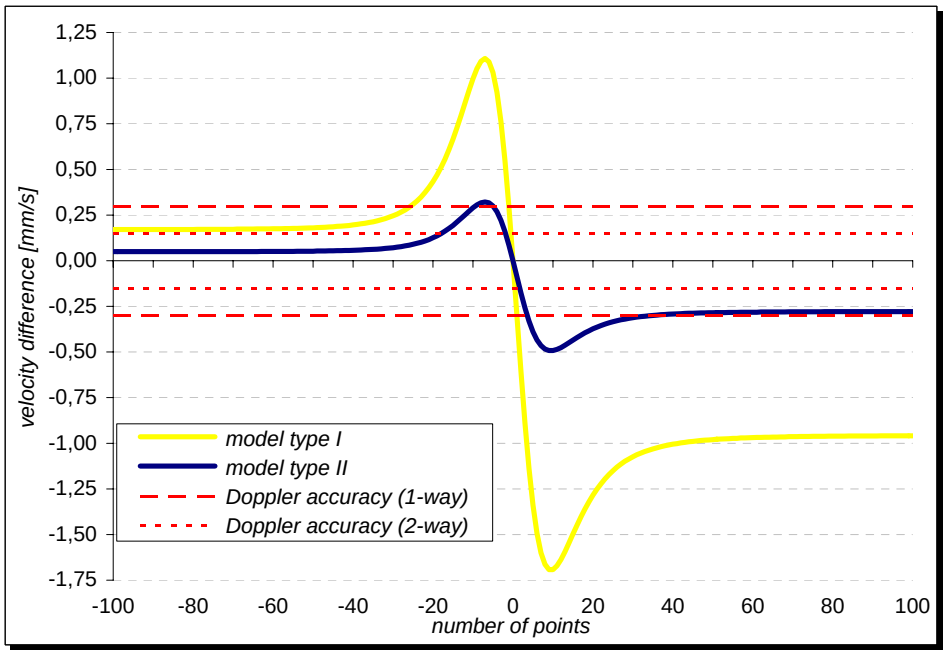

Figure 14.6: Velocity plot for case 1.

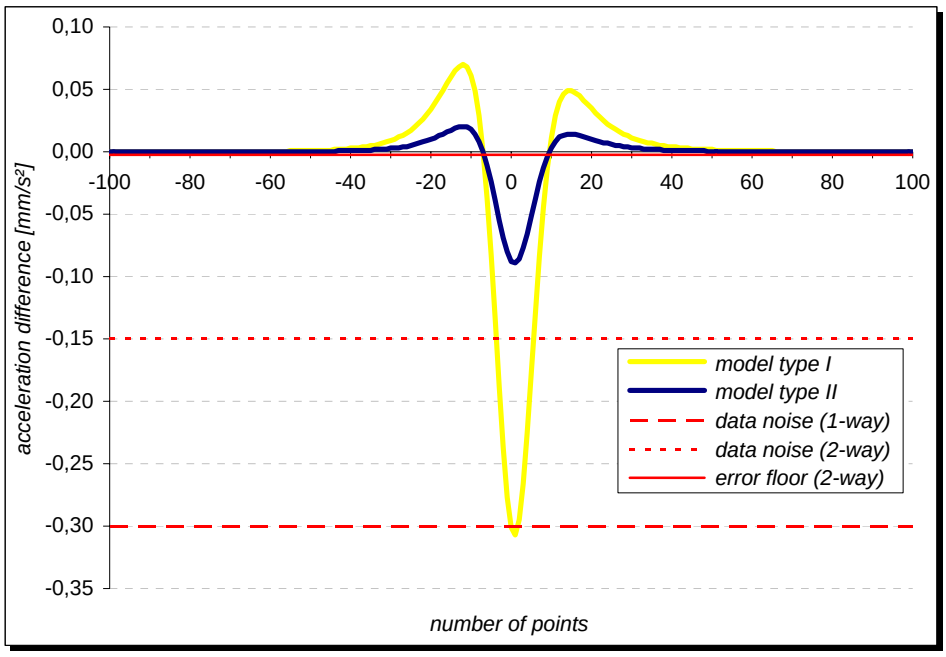

Figure 14.7: Acceleration plot for case 1.

Case 2 yields practically no differences in velocity and acceleration for both model types, thus no information about the heterogeneous interior structure of Amalthea can be derived for the actual flyby configuration!

14.2.1 Actual Flyby Configuration

The actual flyby data (for Doppler data information refer to chapters 7 and 8.1.1) is given through:

- Amalthea's mean density of $\rho_m \sim 860$ kg/m³ (model type *II*), and
- the available 1-way Doppler data received from GALILEO

The values for model type *II* are represented by the blue line in the above graphics. The Doppler accuracy for the 1-way Doppler data (±0.3 mm/s) is too low to detect any velocity differences between the two trajectories. Hence the acceleration difference gives no information about the moments of gravitation. Latter are buried deep in the data noise, although still above the error floor of $\pm 5 \times 10^{-3}$ mm/s² over 60 seconds for 1-way Doppler data (compare to (8-1)). The determination certainty results to approximately 30 % and thus an analysis of the Doppler residuals derived by the DPODP would yield no useful values.

14.2.2 Other Configurations

Considering model type *II* and 2-way Doppler data, velocity differences between the two trajectories would have been detected taking into account a 2-way Doppler accuracy of ±0.15 mm/s. Nevertheless the mass coefficients are still buried in the data noise and could only be derived by the DPODP with a certainty of 60 %.

In the case of model type *I* the Doppler accuracy of the 1-way data would have been good enough to detect velocity differences between the two trajectories. Although the moments of gravitation are still buried in the data noise they could have been analysed by the DPODP with a high certainty. The values for model type *I* are represented by the yellow line in the above graphics.

For the planned 2-way Doppler data and the predicted mean density of Amalthea (model type *I*) it would have been possible to determine the mass coefficients. Nevertheless the flyby configuration would yield no information about a heterogeneous interior structure of the moon.

Considering the same flyby data with respect to the spacecraft's velocity and its polar coordinates but a closer flyby radius (e.g. 100 km, resulting in an altitude above Amalthea of about 29 km), the 1-way Doppler data would have given much better results. The moments of gravitation could have been easily detected (Figure 14.8); still, a heterogeneous interior structure of the moon only with a certainty of approximately 25 % for model type *I* but not at all for the actual low density model type *II* (Figure 14.9). On the other hand, a flyby at such a close distance to the moon is a risky undertaking because of spacecraft navigation uncertainties and thus a possible crash on the body.

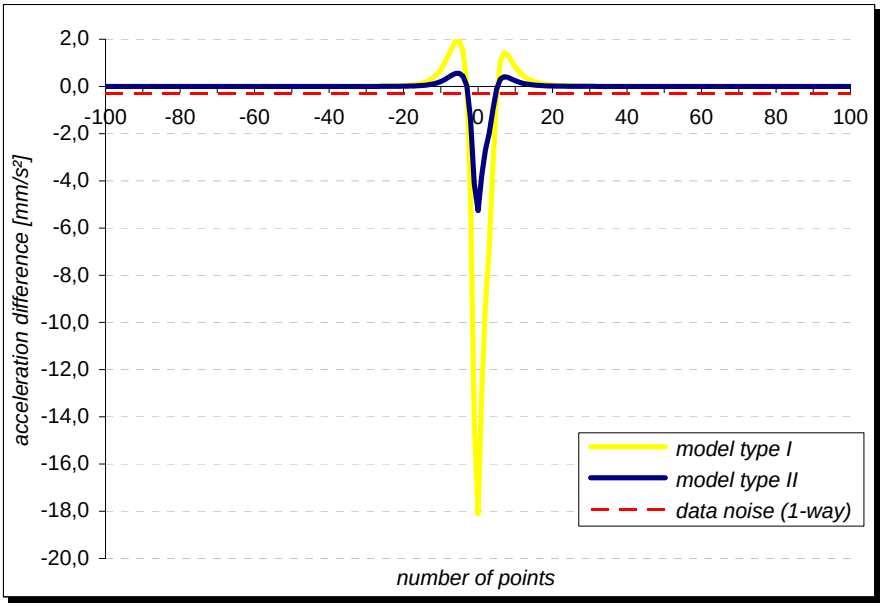

Figure 14.8: Acceleration plot for closer flyby (c/a radius 100 km), case 1.

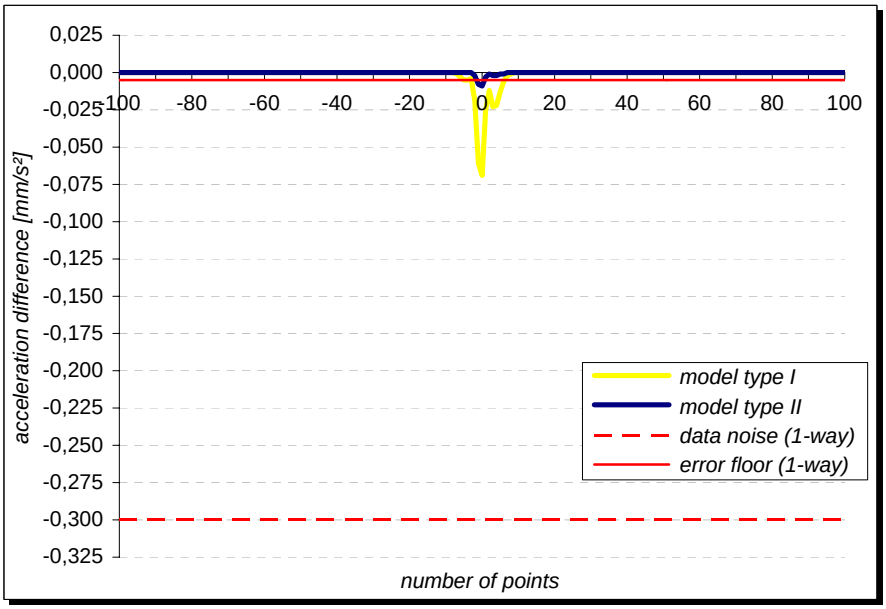

Figure 14.9: Acceleration plot for closer flyby (c/a radius 100 km), case 2.

14.3 PREDICTIONS

In addition to the above interpretations and conclusions, predictions for further space mission flybys of Amalthea can be made through GRASP. For the calculations carried out within the present work, Jupiter's position with respect to the moon is taken over from the actual GALILEO flyby data (closest approach), as well as the spacecraft's velocity $v_{s/c}$~ 18.4 km/s and its altitude $H_{c/a}$~ 183 km above surface. The results are derived within Amalthea's local body-fixed coordinate system and thus take not into consideration the position of the Earth, which will depend on the future flyby date (a perfect Doppler data output can be obtained by placing the Earth line of sight approximately into the spacecraft's flyby direction).

Three scenarios are considered with Amalthea model types *II* (Table 14.1). The different flyby radii $r_{c/a}$ are due to the moon's irregular shape ($r_{c/a} = H_{c/a}$ + body axis).

Flyby scenario	*spacecraft coordinates at c/a*			*spacecraft velocity at c/a*		
	x	y	z	v_x	v_y	v_z
equator, along y-axis (A)	308 km	0	0	0	18.4 km/s	0
equator, along x-axis (B)	0	256 km	0	18.4 km/s	0	0
polar, along x-axis (C)	0	0	247 km	18.4 km/s	0	0

Table 14.1: Future flyby scenarios.

As in chapter 14.2 the following plots illustrate the spacecraft velocity and acceleration differences for the trajectories derived with the assumption of Amalthea as a point mass (considering only *GM*) and Amalthea with a homogeneous interior structure. Because no projection on the Earth line of sight is taken into account, the values shown are absolute. Further to the above mentioned flyby altitude of 183 km a closer flyby with an altitude of 80 km is demonstrated in the graphs. The values for scenario B lie among the other scenarios and are not displayed.

For all scenarios velocity differences between the two trajectories should be easily detectable taking into account a 2-way Doppler accuracy of ±0.15 mm/s. The closer the flyby is chosen the better the evaluation of the Doppler residuals with respect to the moments of gravitation. Furthermore, a polar flyby will generate stronger gravity field signals.

Nevertheless, the evaluation of velocity and acceleration differences between trajectories based on Amalthea with a homogeneous and a heterogeneous interior (case 2) yield signals far below the data noise, even for a very close flyby (comparable to Figure 14.9). Thus no analysis of Amalthea's interior can be made from a spacecraft flyby alone, but needs other means like in-situ geological measurements.

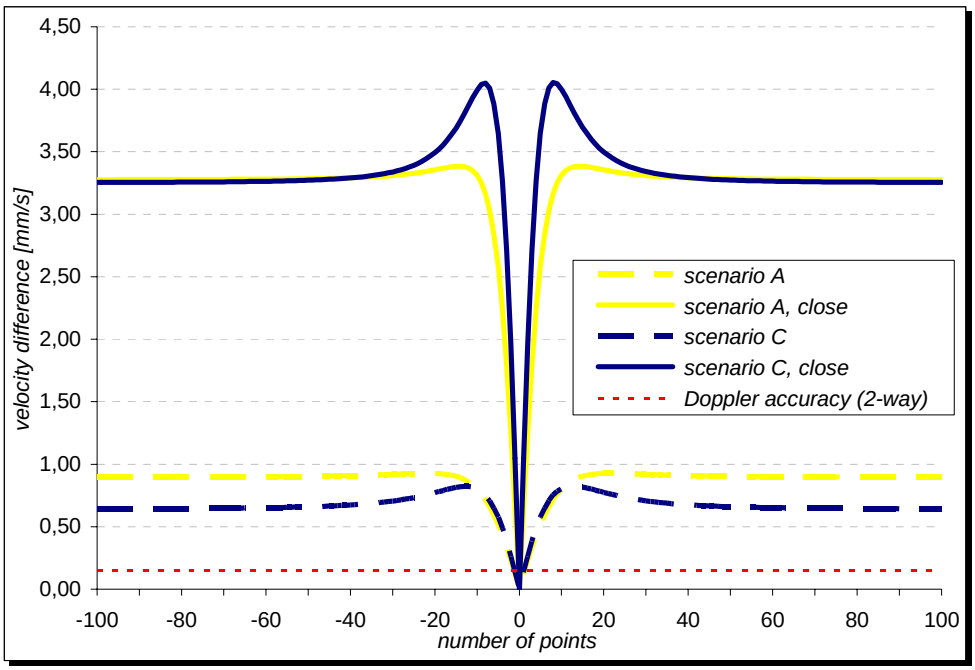

Figure 14.10: Velocity plot for future flyby scenarios.

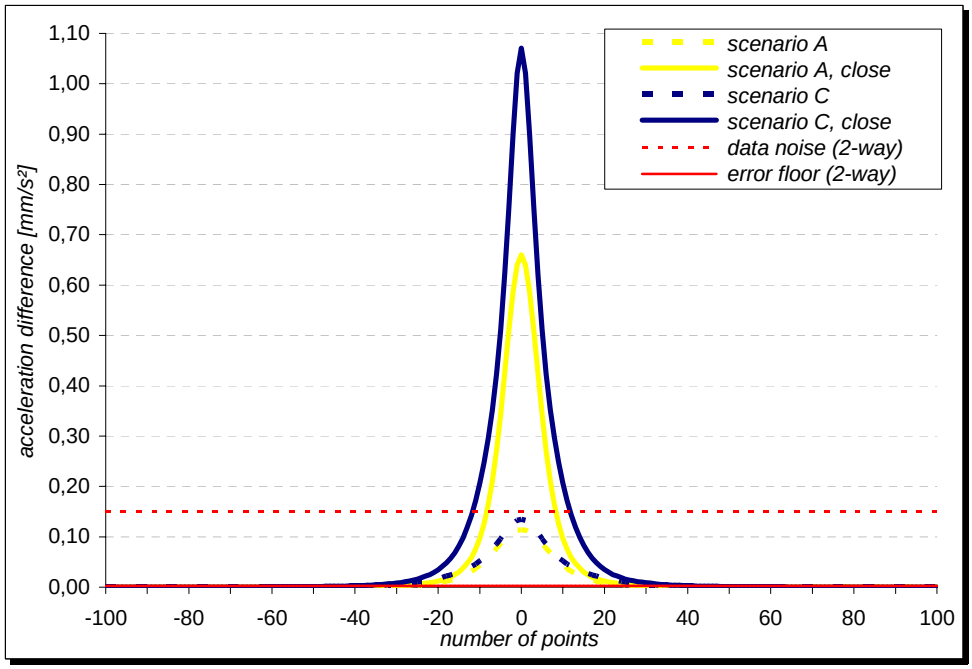

Figure 14.11: Acceleration plot for future flyby scenarios.

15 CONCLUSIONS

The international space endeavours of the past decades have shown social cohesion and public consensus concerning the fundamental, long-range and common causes and purposes of civilisation – survival and progress. The most important objective is the devotion to progressive change and readiness to improve knowledge for the benefit of all the peoples on Earth, whose destiny is to improve life on their planet along with their expansion into the Universe. With scientific and international cooperation being an essential element, the present work provides fundamental contributions to these efforts, the focus lying on planetary body modelling and spacecraft trajectory predictions. The knowledge of the configuration, composition and interior structure of planetary bodies offers insights about our solar system's formation and structure, usability of resources, possible presence of organic material (and thus some form of life), and facilitates the navigation of spacecraft on their planetary exploration tours.

Amalthea, one of Jupiter's small inner moons and the study object within the present work, has the shape of an ellipsoid with axis of 125 km, 73 km and 64 km, and a mean radius of 83.45 km derived for an equal volume sphere. Analyses of the one-way Doppler data obtained during a flyby of the moon by NASA's spacecraft GALILEO reveal a body with a small mass of 2.083×10^{18} kg and consequently mean density of 860 ± 60 kg/m³. This low density was unexpected for most Jupiter system models inside the orbit of the Galilean moon Io and thus implies that Amalthea probably did not aggregate during the Jovian system formation but is a captured planetary body with a composition similar to an asteroid. These objects mostly have a rubble pile structure and are highly fractured inside with considerable pore spaces. A likely composition and interior structure model for Amalthea consists of volatile and void components, carbon-rich materials (rock density ranges from 2000 to 3600 kg/m³, common to CI class asteroids) including water content in the form of water bound in the minerals, and most likely a regolith layer with a couple of hundred kilometre thickness. An open question is whether water-ice might contribute to the low density. Future exploration of Amalthea by means of spacecraft flybys (preferably including imaging) or even in-situ geological measurements will confirm or alter the compiled models of the moon.

Founded on the models for Amalthea's interior structure the gravity field of the moon has been obtained and is described by the moments of gravitation (mass coefficients up to degree and order 6). Latter have been derived by the application of Neumann's second method and the numerical integration of infinitesimal volume elements, calculated by the scale factors of a three-axial ellipsoid (elliptic coordinates) due to Amalthea's non-spherical shape. Actual shape data of the moon can be implemented within the approach but because of long computation times provide no useful input. The analysis of various spacecraft trajectories, based on Amalthea's gravity models and GALILEO's closest approach data, compared to the available GALILEO one-way Doppler data yield no information about the quadrupole or higher degree moments of gravitation. Despite of that, a determination of the mass coefficients would have been possible with the actual flyby configuration, the planned availability of two-way Doppler data and the predicted higher mass of Amalthea (7.167×10^{18} kg).

Future spacecraft flyby scenarios should take into consideration Amalthea's low mass and thus have a low spacecraft altitude in the order of 80 km above surface. Lower altitudes would of course yield more valuable results but are a risky undertaking because of spacecraft navigation uncertainties. To conclude, the best flyby configuration for deriving Amalthea's mass coefficients by means of two-way Doppler data from spacecraft tracking would be a polar flyby along the moon's major axis.

For completeness it should be stated that the above approach for modelling planetary interiors and predicting flyby configuration for the determination of planetary body's gravity fields can be applied to any planetary body, regardless of size, shape and number of interior layers.

16 Acknowledgement

The present study was partially financed by the Zonta International Foundation under the "Amelia Earhart Fellowship" and by the Austrian Ministry of Transport, Infrastructure and Technology under the scholarship for "Short-time Scientific Work at Foreign Institutions". Further support was granted by the Radio Science Team of the Jet Propulsion Laboratory (JPL/NASA), by the Austrian Space Agency, by AUSTROSPACE (the Association of Austrian Space Industries), and by the Institute of Geodesy and Geophysics of the Vienna University of Technology.

The research in the scope of this work would not have been possible without the unrestricted support and patience of my supervisor Prof. Dr. Robert Weber. His encouragement to pursue part of my thesis at a foreign institution and his continuing assistance during this time were very much appreciated, as well as his consequence of moving on. Not to forget the various discussions that led to a much deeper understanding of the subject.

Prof. Dr. Pascale Ehrenfreund's knowledge on the space sciences related to this work and the geology regarding small planetary bodies has helped to improve this contribution. Her subsequent readiness to act as an examiner was very encouraging.

I would like to thank Dr. John D. Anderson for his administrative efforts regarding my one year research visit to JPL, the supply of technical infrastructure, and the valuable insights to spacecraft navigation, mission planning and radio science analysis.

The technical assistance of DI. Mag. Bobby Kazeminejad with respect to the SPICE Toolkit served as a significant input to the data evaluation.

I am very grateful to the various discussions with my space colleagues and their constructive comments, especially to the continually support of my friends Dr. Gerhard Kminek, Dr. Lance Bush, Mag. Gernot Grömer and DI. Norbert Frischauf.

I would like to thank Dr. Gerhard Triebnig for his understanding of finishing my thesis parallel to my full-time work at the Austrian Research Centres.

A special gratitude goes to Elizabeth Gaughen, who was like a grandmother during my stay in the US and has at all times been open-minded and encouraging.

I would like to thank my friends who have always been trying to understand my enthusiasm for space and I am delighted to see some rising interest in the topic with them. I especially want to give appreciation to Dr. Christina Hebenstreit and the time she invested in proof-reading.

And last, but not least, I express gratitude to my parents – I very much esteemed their never-ending support and encouragement, their patience, their discussions and their down-to-Earth point of view.

17 REFERENCES

17.1 LITERATURE

[1] Anderson, John D.: *Lectures on Physical and Technical Problems Posed by Precision Radio Tracking*, Experimental Gravitation, Proceedings of the International School of Physics „Enrico Fermi", Course LVI, Academic Press, New York, 1974.

[2] Anderson, J.D., et al: *Determination of the Mass and Density of Amalthea*, P12C-13, American Geophysical Union (AGU) Fall Meeting, San Francisco, December 2002.

[3] Beebe, Reta: *Jupiter – The Giant Planet*, Smithsonian Institution Press, Washington, 1994.

[4] Bretterbauer, Kurt: *Höhere Geodäsie*, lecture notes, Vienna University of Technology, 1997.

[5] Brown, M.E. et al: *Discovery of a Candidate Inner Oort Cloud Planetoid*, submitted to ApJ Letters, March 2004.

[6] Burns, J.A., Matthews, M.S. (Editors): *Satellites*, University of Arizona Press, Tucson, 1986.

[7] Capitaine, N. et al (Editors): Proceedings of the IERS Workshop on the Implementation of the New IAU Resolutions, IERS Technical Note 29, 2002.

[8] Davies, M.E., et al: *Report of the IAU/IAG/COSPAR Working Group on Cartographic Coordinates and Rotational Elements of the Planets and Satellites: 1994*, Celestial Mechanics and Dynamical Astronomy 63, p. 127-148, Kluwer Academic Publishers, Netherlands, 1996.

[9] Dermott, S.F., Thomas, P.C.: *The Shape and Internal Structure of Mimas*, Icarus 73, p. 25-65, 1988.

[10] Gehrels, Tom (Editor): *Jupiter*, University of Arizona Press, Tucson, 1976.

[11] Gozdziewski, K., et al: *A Model of the Gravitational Field of Amalthea – Part I: Derivation*, Earth, Moon, and Planets 64, p. 243-264, Kluwer Academic Publishers, Netherlands, 1994.

[12] Grant, M., Hazel, J.: *Lexikon der antiken Mythen und Gestalten*, Deutscher Taschenbuch Verlag GmbH, München, 1980.

[13] Hartmann, William K.: *Moons & Planets*, 4th edition, Wadsworth Publishing Company, Belmont/CA, 1999.

[14] Heiskanen, W.A., Moritz, H.: *Physical Geodesy*, W.H. Freeman and Company, San Francisco, 1967.

[15] Houston, A., Rycroft, M. (Editors): *Keys to Space – An Interdisciplinary Approach to Space Studies*, International Space University/McGraw Hill, 1999.

[16] Johnson, T.V., et al: *Galileo's Encounter with Amalthea*, EGS/AGU/EGU Spring Meeting, Nice, April 2003.

[17] Kömle, Norbert I.: *Planetologie I*, lecture notes, Karl-Franzens-University Graz, 2003.

[18] Kreyszig, Erwin: *Advanced Engineering Mathematics*, 7th edition, John Wiley & Sons, Inc., New York, 1993.

[19] Morrison, David (Editor): *Satellites of Jupiter*, University of Arizona Press, Tucson, 1982.

[20] Mottinger, N.A., Moyer, T.D.: *A Close Encounter with a Doppler Observable*, Interoffice Memorandum, Jet Propulsion Laboratory, Pasadena, 1986.

[21] Moyer, Theodore D.: *Mathematical Formulation of the Double-Precision Orbit Determination Program (DPODP)*, Technical Report 32-1527, NASA Jet Propulsion Laboratory, Pasadena, 1971.

[22] Mueller, Ivan I.: *Introduction to Satellite Geodesy*, Frederick Ungar Publishing Co. Inc., New York, 1964.

[23] O'Donnell, Franklin (Editor): *The Jet Propulsion Laboratory*, NASA JPL 400-1048, Pasadena, October 2002.

[24] Officer, Charles: *Introduction to Theoretical Geophysics*, Springer-Verlag Berlin, 1974.

[25] Russell, C.T. (Editor): *The Galileo Mission*, Space Science Reviews, Volume 60, Nos. 1-4, Kluwer Academic Publishers, Netherlands, 1992.

[26] Seeber, Günter: *Satellite Geodesy*, Walter de Gruyter Verlag, Berlin, 2003.

[27] Steiner, W., Schagerl, M.: *Dynamik und Steuerung von Raumfahrzeugen*, lecture notes, Vienna University of Technology, 2003.

[28] Stooke, Philip J.: *A Model and Map of Amalthea*, Earth, Moon, and Planets 56, p. 123-139, Kluwer Academic Publishers, Netherlands, 1992.

[29] Thomas, Peter C.: *The Shapes of Small Satellites*, Icarus 77, p. 248-273, 1989.

[30] Thomas, P.C., et al: *The Small Inner Satellites of Jupiter*, Icarus 135, p. 360-371, 1998.

[31] Titz, Helmut: *Numerische Integration von GPS-Satellitenbahnen auf einem Parallelrechner*, master thesis, Vienna University of Technology, 1995.

[32] Weber, Robert: *Potentialtheorie*, lecture notes, Vienna University of Technology, 2002.

[33] Webster, Arthur G.: *The Dynamics of Particles and of Rigid, Elastic, and Fluid Bodies*, Lectures on Mathematical Physics, 3rd Edition, B.G.Teubner, Leipzig, 1925.

[34] Yoder, Charles F.: *Astrometric and Geodetic Properties of Earth and the Solar System*, Global Earth Physics – A Handbook of Physical Constants, American Geophysical Union (AGU) Reference Shelf 1, 1995.

[35] Zimmermann, H., Weigert, A.: *ABC-Lexikon Astronomie*, 8. überarbeitete Auflage, Spektrum Akademischer Verlag GmbH, Heidelberg, 1995.

17.2 Personal Communication, E-Mail News, WebPages

[36] Allan, David W., *Allan Variance*, http://www.allanstime.com/AllanVariance/index.html

[37] Anderson, John D.: personal communications, September 2002.

[38] Baalke, Ron: *Today on Galileo – November 4-5, 2002*, Galileo-email-news, Jet Propulsion Laboratory, Pasadena, 2002.

[39] Baalke, Ron: *Galileo e-mail Newsletter*, NASA Jet Propulsion Laboratory, Pasadena, 2003.

[40] Johnson, Torrence V.: personal communications, May 2004.

[41] Sheppard, Scott S.: *Jupiter Irregular Satellite and Moon Page*, http://www.ifa.hawaii.edu/~sheppard/satellites, University of Hawaii, Institute of Astronomy, 2004.

[42] Thomas, Peter C.: personal communication, July 2002.

[43] *Deep Space Network*, http://deepspace.jpl.nasa.gov/dsn, NASA Jet Propulsion Laboratory, Pasadena, 2004.

[44] *Galileo Mission to Jupiter*, NASA Facts Jet Propulsion Laboratory, Pasadena, September 2003.

[45] *Jupiter Icy Moons Orbiter*, http://www.jpl.nasa.gov/jimo, Project Homepage, NASA Jet Propulsion Laboratory, Pasadena, 2004.

[46] *Pioneer*, http://spaceprojects.arc.nasa.gov/Space_Projects/pioneer/PNhome.html and http://spaceprojects.arc.nasa.gov/Space_Projects/ThePast/pioneer.html, Project Homepage, NASA Ames Research Center, Moffet Field, 2004.

[47] *Voyager – The Interstellar Mission*, http://voyager.jpl.nasa.gov, Project Homepage, NASA Jet Propulsion Laboratory, Pasadena, 2004.

17.3 Photos and Graphics

Figure 1.1: http://homepage.mac.com/cparada/GML/000Free/000Planets/source/7.html

Figure 1.2: http://www-gap.dcs.st-and.ac.uk/~history/PictDisplay/Galileo.html

Figure 1.3: http://astro.uchicago.edu/yerkes/virtualmuseum/Barnardfull.html

Figure 2.1: http://spaceprojects.arc.nasa.gov/Space_Projects/pioneer/path.html

Figure 2.2: http://saturn.jpl.nasa.gov/multimedia/images/artwork/index.cfm

Figure 2.3: http://www.hardyart.demon.co.uk/html/p-jup1.html

Figure 3.1: http://www.solarviews.com/cap/misc/obliquity.htm

Figure 3.2: http://www.solarviews.com/cap/jup/jupsystm.htm

Figure 3.3: http://www.solarviews.com/cap/jup/jupint.htm

Figure 3.4: http://photojournal.jpl.nasa.gov/catalog/PIA01627

Figure 3.5: http://photojournal.jpl.nasa.gov/catalog/PIA00600

Figure 4.1: http://homepage.mac.com/cparada/GML/000Free/000Zeus/source/9.html

Figure 4.2: http://www.solarviews.com/cap/jup/amalthea.htm

Figure 4.3: http://photojournal.jpl.nasa.gov/catalog/PIA01624

Figure 4.4: © Gudrun Weinwurm

Figure 4.5: [6] Burns, J.A., Matthews, M.S. (Editors): *Satellites*, University of Arizona Press, Tucson, 1986.

Figure 5.1: © Gudrun Weinwurm

Figure 5.2: [25] Russell, C.T. (Editor): *The Galileo Mission*, Space Science Reviews, Volume 60, Nos. 1-4, Kluwer Academic Publishers, Netherlands, 1992.

Figure 5.3: http://galileo.jpl.nasa.gov/images/idacolor.html

Figure 5.4: http://photojournal.jpl.nasa.gov/catalog/PIA00139

Figure 6.1, Figure 6.2: © Gudrun Weinwurm

Figure 6.3: Numerical Recipes in C: the Art of Scientific Computing, p. 712, Cambridge University Press, 1988-1992.

Figure 6.4 – Figure 6.6: © Gudrun Weinwurm

Figure 6.7: http://www2.jpl.nasa.gov/basics/bsf4-1.htm

Figure 6.8: http://www.jpl.nasa.gov/galileo/sepo/education/bulletin/launch_to_g29.html

Figure 7.1: © Gudrun Weinwurm

Figure 7.2: http://www.jpl.nasa.gov/images/dsn/goldstone/index.html

Figure 8.1: http://www.asaa-avart.org/Exhibit2003images/CarrollEncounter.html

Figure 8.2: © Gudrun Weinwurm with RedShift4 (Maris Multimedia, Ltd.)

Figure 8.3: © Gudrun Weinwurm

Figure 8.4, Figure 8.5: http://www2.jpl.nasa.gov/galileo/countdown/
Figure 8.6: © Gudrun Weinwurm
Figure 9.1 – Figure 9.5: © Gudrun Weinwurm
Figure 10.1, Figure 10.2: © Gudrun Weinwurm
Figure 11.1: © Gudrun Weinwurm
Figure 12.1 – Figure 12.13: © Gudrun Weinwurm
Figure 13.1: © Gudrun Weinwurm
Figure 14.1 – Figure 14.11: © Gudrun Weinwurm

Appendix

A. GALILEO'S SCIENTIFIC PAYLOAD AND OBJECTIVES

Source: [25] Russell, C.T. (Editor): *The Galileo Mission*, Space Science Reviews, Volume 60, Nos. 1-4, Kluwer Academic Publishers, Netherlands, 1992.

Experiment	*Mass (kg)*	*Range*	*Objectives*
Probe			
Atmospheric Structure Instrument (ASI)	4	Temperature: 0-540 K Pressure: 0-28 bar	Determine temperature, pressure, density, and molecular weight as a function of altitude
Neutral Mass Spectrometer (NMS)	11	Covers 1-150 amu	Determine chemical composition of atmosphere
Helium Abundance Detector (HAD)	1	Accuracy: 0.1%	Determine relative abundance of helium
Nephelometer (NEP)	5	0.2-20 μm particles as few as 3 cm^3	Detect clouds and inter states of particles (liquid versus solid)
Net-flux Radiometer (NFR)	3	6 infrared filters from 0.3 to 100 μm	Determine ambient thermal and solar energy as a function of altitude
Lighting and Energetic Particles (LRD/EPI)	2	Fisheye lens sensors, 1 Hz-100 kHz	Verify the existence of lightning and measure energetic particles in inner magnetosphere
Orbiter			
Solid-State Imaging (SSI)	28	1500 mm, f/8.5, 800x800 CCD, 8 filters, 0.47° field-of-view	Map Galilean satellites at roughly 1km resolution, and monitor atmospheric circulation over 20 months while in orbit around planet
Near-Infrared Mapping Spectrometer (NIMS)	18	0.7-5.2 m range, 0.03 μm resolution 0.5 m rad IFOV	Observe Jupiter and its satellites in the infrared to study satellite surface composition, Jovian atmospheric composition and temperature
Ultraviolet Spectrometer (UVS)	4	1150-4300 Å	Measure gases and aerosols in Jovian atmosphere
Extreme Ultraviolet Spectrometer (EUV)	13	54 to 128 nm	Investigate So, O ion emissions of the Io torus, and atomic and molecular H auroral and airglow emissions of Jupiter
Photopolarimeter-Radiometer (PPR)	5	Discrete visible and near-infrared bands, radiometry to >42 μm	Determine distribution and character of atmospheric particles; compare flux of thermal radiation to incoming solar levels
Magnetometer (MAG)	7	32-16384 γ	Monitor magnetic field for strength and changes
Energetic Particles Detector (EPD)	10	Ions: 0.020-55 MeV Electrons: 0.015-11 MeV	Measure high-energy electrons, protons, and heavy ions in and around Jovian magnetosphere and study processes affecting these populations
Plasma Detector (PLS)	13	1 eV to 50 keV in 64 bands	Assess composition, energy, and three-dimensional distribution of low-energy electrons and ions

Continued

Plasma Wave (PWS)	7	E: 5 Hz to 5.6 MHz B: 5 Hz to 160 kHz Wideband 1 kHz, 10kHz, 80 kHz	Detect electromagnetic waves and analyse wave-particle interactions
Dust Detector (DDS)	4	10-16 g to 10-6 g, 2-50 km/s	Measure particles' mass, velocity, and charge
Radio Science (RS): Celestial Mechanics	-	S- and X-band signals	Determine mass of Jupiter and its satellites (uses radio system and high-gain antenna)
Radio Science (RS): Propagation	-	S- and X-band signals	Measure atmospheric structure and objects' radii (uses radio system and high-gain antenna)
Heavy Ion Counter (HIC)	8	Ions from carbon to nickel range – 6 to >200 MeV/nucl	Monitor the fluxes and composition of energetic heavy ions in the inner Jovian magnetosphere, and high energy solar particles in the outer magnetosphere, characterise the ionising radiation

B. GALILEO Amalthea Flyby Timeline

Source: [38] Baalke, Ron: *Today on Galileo – November 4-5, 2002*, Galileo-email-news, Jet Propulsion Laboratory, Pasadena, 2002.

Encounter with Amalthea

Early Monday morning begins our sprint into the inner reaches of the Jupiter system to snatch the scientific secrets of that environment out from under the nose of the gas giant, and to skirt by the tiny inner satellite Amalthea. The science instruments that will focus on the inner magnetosphere are the Dust Detector (DDS), the Energetic Particle Detector (EPD), the Heavy Ion Counter (HIC), the Magnetometer (MAG), the Plasma Subsystem (PLS), and the Plasma Wave Subsystem (PWS) instruments. The Galileo spacecraft, however, may be unique among NASA's planetary probes in being the only mission to add a science instrument to its payload after launch!

The Attitude Control Star Scanner, an engineering system normally used to provide information about the orientation of the spacecraft by sensing the locations of stars, can double as a radiation sensor. Several years ago, engineers noticed that the pesky radiation-induced noise that interferes with the normal star sensing of the instrument could be used to provide a measure of the intensity of that radiation. The sensor mechanism is most sensitive to high-energy electrons. Though the instrument was never designed or calibrated to provide an absolute physical measure of the quantity of such electrons, when combined with the measurements taken by the other science instruments, the relative noise level seen by the Star Scanner can provide additional insight into the continuum of particles and other radiation in the environment sensed by Galileo.

At midnight, the spacecraft is 20 Jupiter radii from the center of the giant planet (1.43 million kilometers or 888,000 miles) and the science instruments are studying the magnetospheric plasma sheet, which periodically waves past Galileo as the planet rotates.

By 6:30 a.m., PST, the radiation from Jupiter is becoming strong enough to cause a noticeable effect in the Star Scanner. At this point, the Attitude Control system is told to rely only on a single bright star for knowledge of the orientation of the spacecraft. The static in the sensor caused by the radiation is enough to mask the signals from fainter stars. The single bright star we are using for this encounter is Rigel Kentaurus, more popularly known as Alpha Centauri, the nearest bright star to the Sun.

At 9:45 a.m., the EPD instrument turns its power off and on again, and reloads its memory. During a small number of previous encounters, this instrument has suffered upsets which can only be cleared by this technique. Three times during this flyby the instrument is reset in this fashion, so that if an upset occurs, the instrument will be able to continue to collect science data without waiting for commands from Earth to correct the problem.

At 1:02 p.m., the Radio Science team begins an experiment to measure the gravity field of the small satellite Amalthea. Though we are still 10 hours away from the closest approach, the team uses this distant measurement of the radio signal to establish a baseline against which they can compare the changes seen as Amalthea's gravity tugs on Galileo during the later flyby. By measuring the extent and nature of this tug, the mass of Amalthea can be determined. In addition, the flyby's proximity will also yield knowledge of whether or not Amalthea has a dense central region or core. This information will give additional clues as to the composition of Amalthea and may also help us to understand its origin.

At 2:55 p.m., the spacecraft is again expected to pass through Jupiter's plasma sheet, and detailed Fields and Particles measurements are written to the tape recorder. The recorder is used to collect data faster than the spacecraft can transmit in real time. At this time the spacecraft is only 10 Jupiter radii from the planet (715,000 kilometers or 444,000 miles). After 45 minutes, the instruments revert to collecting data for real-time transmission to Earth.

At 5:49 p.m., the Fields and Particles instruments switch from transmitting all of their data in real-time to begin recording the data for later playback. This allows the instruments to collect more data at a higher time resolution than would be

possible in real time. This recording continues for the next 10.5 hours, through the closest approach to Amalthea and Jupiter.

At 6:07 p.m., the spacecraft changes its telemetry system to put more power into the fundamental carrier frequency that is transmitted. This allows the 70-meter-diameter (230 foot) communications antenna located near Madrid, Spain, to better track the Galileo signal during the upcoming close flyby of Amalthea. It is the change in frequency (Doppler shift) of this transmitted signal that provides the Radio Science and Navigation teams the information about Amalthea's gravity field.

At 7:18 p.m., the Near Infrared Mapping Spectrometer begins a 5-minute period of real-time collection of engineering data. This peek into the signals generated by the instrument as the radiation level rises will help researchers understand detector behavior seen during observations taken on previous orbits. This information can be used to help engineers design instruments that will operate in similar radiation environments for future missions.

At 7:41 p.m., Galileo reaches the closest point to the volcanic satellite Io. At 45,250 kilometers (28,100 miles), this pass is over twice the distance that Voyager 1 flew by in 1979, and is a distant cousin to the 101-kilometer (63-mile) altitude at the previous encounter in January of this year. No observations of Io are planned during this passage. The spacecraft is passing Io's orbit at about 6 Jupiter radii (429,000 kilometers or 267,000 miles) from the planet on its way in to the inner system.

The radiation at this point in the orbit is becoming fierce enough that even Alpha Centauri may no longer be seen by the Star Scanner, and the attitude control software would not be able to determine the orientation of the spacecraft. At 8:12 p.m., the software is told to enter hibernation. In this state it will ignore the signals from the Star Scanner and remember its last calculated orientation and spin rate, relying on the fact that we don't plan to change it. This configuration will last for the next nine hours, while Galileo is within the distance of Io's orbit.

Then, at 11:02:28 p.m., Galileo reaches its closest point to Amalthea. This irregularly-shaped moon measures approximately 270 kilometers (168 miles) across its longest dimension. Galileo will fly by with its closest distance to the surface of the body of 160 kilometers (99 miles). The speed of the spacecraft relative to Amalthea is 18.4 kilometers per second (41,160 miles per hour) so it will take less than 15 seconds to pass by! At this speed, Galileo could circle the Earth (at sea level) in 36 minutes, not counting stops for the speeding tickets.

Ten minutes later, at 11:14 p.m., Galileo enters the shadow cast by Jupiter from the Sun, and eleven minutes after that, at 11:25 p.m., the spacecraft passes behind Jupiter as seen from Earth. The spacecraft will remain out of view of ground controllers for about an hour, reappearing 23 minutes after midnight on Tuesday morning, having cleared Jupiter's shadow 10 minutes earlier.

While the spacecraft is hidden from Earth, at eight minutes after midnight, it will reach this orbit's closest point to Jupiter. This is also the closest Galileo has ever come to the planet. Galileo will pass 71,500 kilometers (44,500 miles) above the visible cloud tops. This is three times closer than the previous Galileo record in 1995, which was set as we first entered Jupiter orbit. Pioneer 11 still holds the ultimate record, however, speeding by in 1973 only 43,000 kilometers (26,725 miles) above the clouds.

For a period of about two hours, starting about the time Galileo passes Amalthea, the spacecraft will be passing through a region occupied by what is known as the Amalthea Gossamer Ring. This very tenuous band of dusty material circles Jupiter between Amalthea's orbit and the start of the more prominent main ring first noticed by the Voyager spacecraft in 1979. This offers a unique opportunity to study a planetary ring system from the inside! The Dust Detector instrument will be the primary student, but the plasma environment is also likely to hold some interesting surprises.

On the outbound stretch of the Jupiter-Earth occultation, the Radio Science team will use the radio transmission from Galileo to probe the layers of the Jupiter atmosphere, studying how the signal changes as it passes through increasingly thinner gases as the spacecraft recedes from its closest point.

At 12:20 a.m., the EPD instrument reloads its memory again, as protection against a possible upset in the high radiation environment. During this single flyby the spacecraft may be subjected to up to 100 times the radiation dose that would be

lethal to a human being. It has already received more than 4 times its planned spacecraft-lifetime dosage, and is still ticking away.

At 12:37 a.m., the Radio Science occultation experiment is over, and science telemetry is restored into the radio signal. For the past few hours, the Fields and Particles science data have been stored on both the tape recorder and in a computer memory buffer while the spacecraft has been out of sight. Now the buffered data can be sent to Earth. The continuous recording period ends at 4:04 a.m. Recorded data from the encounter will be played back starting Thursday evening.

At 4:15 a.m., Galileo again crosses Io's orbit, this time outward bound, and the radiation levels have dropped to the point that the Star Scanner should again be able to recognize Alpha Centauri. At this time the attitude control software is told to come out of hibernation and re-establish its lock on that single bright star. By 6:30 p.m., the radiation has dropped to the level that will allow fainter stars to be seen, and the software is told to look for the normal contingent of three stars.

Finally, (has this really only been two days?) the tape recorder is slewed to a new position and a new series of plasma sheet observation recordings is begun at 11:07 p.m. Tuesday night. The high-intensity pace of the encounter has slowed to a more bearable crawl, the spacecraft has receded again to 20 Jupiter radii from the planet, and the final flyby of the mission is behind us.

==========

Note 1. Pacific Standard Time (PST) is 8 hours behind Greenwich Mean Time (GMT). The time when an event occurs at the spacecraft is known as Spacecraft Event Time (SCET). The time at which radio signals reach Earth indicating that an event has occurred is known as Earth Received Time (ERT). Currently, it takes Galileo's radio signals 44 minutes to travel between the spacecraft and Earth. All times quoted above are in Earth Received Time at JPL in Pasadena.

For more information on the Galileo spacecraft and its mission to Jupiter, please visit the Galileo home page at one of the following URL's:

http://galileo.jpl.nasa.gov

http://www.jpl.nasa.gov/galileo

C. GALILEO DATA AT CLOSEST APPROACH

Source: Anderson, John D., personal communications, December 2002.

Excerpt from the DPODP data file:

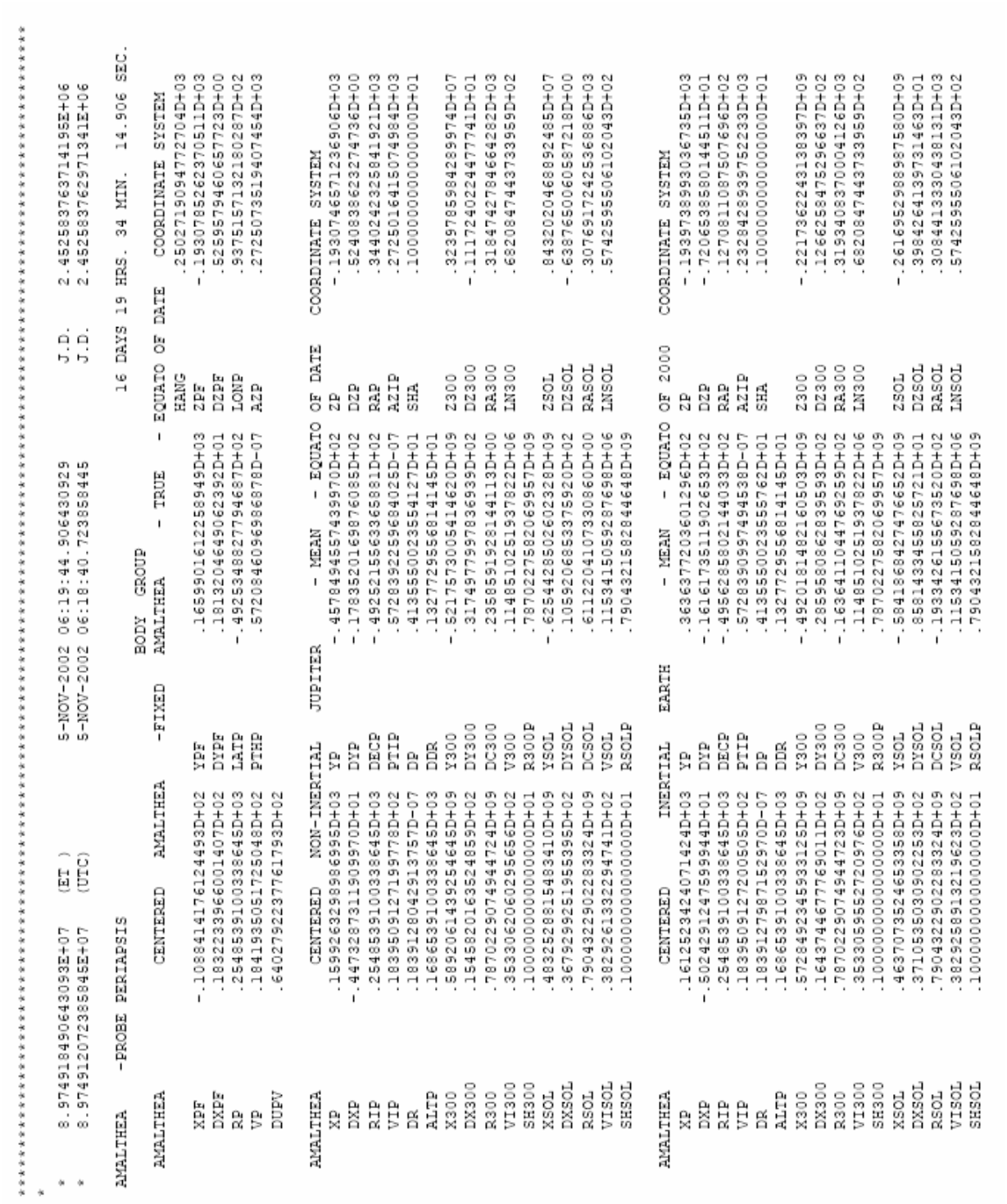

```
Relevant parameters:
XP, YP, ZP … spacecraft coordinates
DXP, DYP, DZP … spacecraft velocity
RIP … radius vector from centre of Amalthea to spacecraft
X300, Y300, Z300 … Earth coordinates
XSOL, YSOL, ZSOL … Sun coordinates
```

D. GALILEO and Planetary Data at Closest Approach

Source: Kazeminejad, Bobby, personal communications, December 2003.

```
KERNELS USED FOR TRANSFORMATION
 LEAP-SECOND FILE: LS_NAIF0007.TXT
 AMALTHEA EPHEMERIS FILE: JUP120_1996-2010.BSP
 PLANETARY CONSTANT FILE: PCK00007.TPC
 JUPITER EPHEMERIS: DE405.BSP

 EPOCH (UTC)= 05-NOV-2002 06:18:40.723858445
 EPOCH (ET)= 2002-11-05T06:18:40.7238

 GALILEO IN AMALTHEA CENTERED J2000 SYSTEM

XP=   0.1612523424071424D+03
YP=   0.3636377203601296D+02
ZP=   -.1939738993036735D+03
DXP=  -.5024291247599944D+01
DYP=  -.1616173511902653D+02
DZP=  -.7206538580144511D+01

 GALILEO IN AMALTHEA CENTERED BODY-FIXED SYSTEM (NAIF ID: IAU_AMALTHEA)

XP=   0.5842412397169222D+02
YP=   0.1548888397618504D+03
ZP=   -.1937694106790782D+03
DXP=  0.1740284072485501D+02
DYP=  -.6018218107416210D+01
DZP=  0.4365544535308397D+00

 JUPITER IN AMALTHEA CENTERED J2000 SYSTEM

XP=   0.1648672290751625D+05
YP=   -.1635217621968356D+06
ZP=   -.7646985597682821D+05
DXP=  0.2636830603418336D+02
DYP=  0.2034953703621695D+01
DZP=  0.1447596489013380D+01

 JUPITER IN AMALTHEA CENTERED BODY-FIXED SYSTEM (NAIF ID: IAU_AMALTHEA)

XP=   0.1811619424805439D+06
YP=   0.6258309743020722D+04
ZP=   0.4210868143069092D+02
DXP=  -.4899970819523858D-01
DYP=  0.2356815116729064D-01
DZP=  -.8786285290998563D-02

 SUN IN AMALTHEA CENTERED J2000 SYSTEM

XP=   0.4637073524653358D+09
YP=   -.5841868427476652D+09
ZP=   -.2616952988987580D+09
DXP=  0.3710535030902253D+02
DYP=  0.8581433455825721D+01
DZP=  0.3984264139731463D+01

 SUN IN AMALTHEA CENTERED BODY-FIXED SYSTEM (NAIF ID: IAU_AMALTHEA)

XP=   0.6652179060843022D+09
YP=   0.4269138460922086D+09
ZP=   0.3593170630710572D+07
DXP=  0.6231168728625942D+05
DYP=  -.9706806168029277D+05
DZP=  -.1103352704021621D+00
```

```
 EARTH IN AMALTHEA CENTERED J2000 SYSTEM

XP=   0.5728492345933125D+09
YP=   -.4920181482160503D+09
ZP=   -.2217362243138397D+09
DXP=  0.1643744677769011D+02
DYP=  0.2859580862839593D+02
DZP=  0.1266258475296637D+02

 EARTH IN AMALTHEA CENTERED BODY-FIXED SYSTEM (NAIF ID: IAU_AMALTHEA)

XP=   0.5711324468303854D+09
YP=   0.5414896729626707D+09
ZP=   -.1311172517135054D+07
DXP=  0.7901402540144350D+05
DYP=  -.8335326987747882D+05
DZP=  0.3573550856521557D-01


Relevant parameters:
XP, YP, ZP … body coordinates
DXP, DYP, DZP … body velocity
```

E. LEGENDRE FUNCTIONS AND NEUMANN COEFFICIENTS

E.1. LEGENDRE FUNCTIONS AND DERIVATES

$t = \cos\vartheta$

$$P_0(t) = 0$$
$$P_1(t) = t$$
$$P_2(t) = \frac{3}{2}t^2 - \frac{1}{2}$$
$$P_3(t) = \frac{5}{2}t^3 - \frac{3}{2}t$$
$$P_4(t) = \frac{35}{8}t^4 - \frac{15}{4}t^2 + \frac{3}{8}$$
$$P_5(t) = \frac{63}{8}t^5 - \frac{35}{4}t^3 + \frac{15}{8}t$$
$$P_6(t) = \frac{231}{16}t^6 - \frac{315}{16}t^4 + \frac{105}{16}t^2 - \frac{5}{16}$$
$$P_7(t) = \frac{429}{16}t^7 - \frac{693}{16}t^5 + \frac{315}{16}t^3 - \frac{35}{16}t$$

$$P_{11}(\cos\vartheta) = \sin\vartheta$$
$$P_{21}(\cos\vartheta) = 3\sin\vartheta\cos\vartheta$$
$$P_{22}(\cos\vartheta) = 3\sin^2\vartheta$$
$$P_{31}(\cos\vartheta) = \sin\vartheta\left(\frac{15}{2}\cos^2\vartheta - \frac{3}{2}\right)$$
$$P_{32}(\cos\vartheta) = 15\sin^2\vartheta\cos\vartheta$$
$$P_{33}(\cos\vartheta) = 15\sin^3\vartheta$$

$$dP_1(\cos\vartheta) = -\sin\vartheta$$
$$dP_2(\cos\vartheta) = -3\cos\vartheta\sin\vartheta$$
$$dP_3(\cos\vartheta) = \frac{3}{2}\sin\vartheta\left(1 - 5\cos^2\vartheta\right)$$
$$dP_4(\cos\vartheta) = \frac{5}{2}\sin\vartheta\cos\vartheta\left(3 - 7\cos^2\vartheta\right)$$
$$dP_5(\cos\vartheta) = \frac{5}{8}\sin\vartheta\left(-63\cos^4\vartheta + 28\cos^2\vartheta - 3\right)$$
$$dP_6(\cos\vartheta) = \frac{3}{8}\cos\vartheta\sin\vartheta\left(-231\cos^4\vartheta + 210\cos^2\vartheta - 70\right)$$

E.2. NEUMANN COEFFICIENTS – THE 2ND METHOD

E.2.1. DEGREE P=4

$$P_5(t) = \frac{63}{8}t^5 - \frac{35}{4}t^3 + \frac{15}{8}t = 0$$

$t_1 = 0.9061798459386641$
$t_2 = 0.538469310105683$
$t_3 = 0$
$t_4 = -t_2$
$t_5 = -t_1$

$a_1 = a_5 = 0.23692688505618892$
$a_2 = a_4 = 0.47862867049936714$
$a_3 = 0.5688888888888878$

E.2.2. DEGREE P=5

$$P_6(t) = \frac{231}{16}t^6 - \frac{315}{16}t^4 + \frac{105}{16}t^2 - \frac{5}{16} = 0$$

$t_1 = 0.9324695142031517$
$t_2 = 0.6612093864662648$
$t_3 = 0.2386191860831969$
$t_4 = -t_3$
$t_5 = -t_2$
$t_6 = -t_1$

$a_1 = a_6 = 0.17132449237917077$
$a_2 = a_5 = 0.3607615730481373$
$a_3 = a_4 = 0.4679139345726918$

E.2.3. DEGREE P=6

$$P_7(t) = \frac{429}{16}t^7 - \frac{693}{16}t^5 + \frac{315}{16}t^3 - \frac{35}{16}t = 0$$

$t_1 = 0.9491079123427585$
$t_2 = 0.7415311855993945$
$t_3 = 0.4058451513773972$
$t_4 = 0$
$t_5 = -t_3$
$t_6 = -t_2$
$t_7 = -t_1$

$a_1 = a_7 = 0.12948496616886995$
$a_2 = a_6 = 0.2797053914892751$
$a_3 = a_5 = 0.38183005050512364$
$a_4 = 0.4179591836734626$

F. GRASP ROUTINES

F.1. VOLUME APPROXIMATIONS

Derivation of the volume of a planetary body by means of scale factors (spheroidal approach, ellipsoidal approach):

beginn | volumen | potkoeffhom

```
procedure volumecalculation;   {spheroid or sphere, based on scale factors}
var e2: real;   {square of linear eccentricity a*e}
    u,du: real;
    h1,h2,h3: extended;   {scale factors}
begin
     VAchsen:=4/3*PI*a*b*c;
     e2:=sqr(a)-sqr(c);
     V:=0;
     du:=c/k;
     u:=du;
     repeat   {u from 0 to c}
        theta:=0;
        repeat   {reduced polar distance theta from 0° to 180°}
           lambda:=0;
           repeat   {lambda from 0° to 360°-dlambda}
              h1:=sqrt((sqr(u)+e2*sqr(cos((theta+dtheta/2)*PI/180)))/(sqr(u)+e2));
              h2:=sqrt(sqr(u)+e2*sqr(cos((theta+dtheta/2)*PI/180)));
              h3:=sqrt((sqr(u)+e2)*sqr(sin((theta+dtheta/2)*PI/180)));
              dV:=h1*h2*h3*du*(dtheta*PI/180)*(dlambda*PI/180);
              V:=V+dV;
              lambda:=lambda+dlambda;
           until lambda>=360;
           theta:=theta+dtheta;
        until theta>=180;
        u:=u+du;
     until u>=c+du;
end;
```

158: 5 | Geändert | Einfügen

beginn | volumen | potkoeffhom

```
procedure volumecalculation3axis;  {scale factores based on elliptic coordinates}
var lam, mue, nue: extended;   {elliptical coordinates}
    dlam, dmue, dnue: extended;   {steps for numerical integration}
    h1, h2, h3: extended;   {scale factors}
    i: integer;
begin
     VAchsen:=4/3*PI*a*b*c;
     V:=0;
     dmue:=(sqr(b)-sqr(c))/k;
     dnue:=(sqr(a)-sqr(b))/k;
     i:=0;
     repeat   {lam from -c² to 0}
        i:=i+1;
        lam:=-sqr(c)+(sqr(i)*sqr(c)/sqr(k))-1;
        dlam:=sqr(c)/sqr(k)*(sqr(i)-sqr(i-1));
        mue:=-sqr(b)+dmue/2;
        repeat   {mue from -b² to -c²}
           nue:=-sqr(a)+dnue/2;
           repeat   {nue from -a² to -b²}
              h1:=1/2*sqrt(((lam-mue)*(lam-nue))/((sqr(a)+lam)*(sqr(b)+lam)*(sqr(c)+lam)));
              h2:=1/2*sqrt(((mue-nue)*(mue-lam))/((sqr(a)+mue)*(sqr(b)+mue)*(sqr(c)+mue)));
              h3:=1/2*sqrt(((nue-lam)*(nue-mue))/((sqr(a)+nue)*(sqr(b)+nue)*(sqr(c)+nue)));
              dV:=h1*h2*h3*dlam*dmue*dnue;
              V:=V+dV*8;
              nue:=nue+dnue;
           until nue>=-sqr(b);
           mue:=mue+dmue;
        until mue>=-sqr(c);
     until i=k;
end;
```

158: 5 | Geändert | Einfügen

F.2. ROTATIONAL MATRIX

Calculation of the rotation angles ex, ey, ez from the inertial coordinate system J2000 into a local body-fixed coordinate system, by means of three identical points – in this case the coordinates of the planets Earth (xE, yE, zE) and Jupiter (xB, yB, zB), and the Sun (xS, yS, zS).

```
beginn | warten | volumen | steps | potkoeffhom | trajectory | FmxUtils
procedure matrix;
var Rotmat: array [1..3,1..3] of extended;   {rotational matrix}
begin
     Rotmat[2,3]:=(xSi*yEi*B_y-xSi*E_y*yBi-xBi*yEi*S_y+xEi*yBi*S_y+xBi*E_y*ySi-xEi*B_y*ySi)/
        (-xSi*yBi*zEi+xBI*ySi*zEi+xSi*yEi*zBi-xEi*ySi*zBi-xBi*yEi*zSi+xEi*yBi*zSi);
     Rotmat[2,2]:=(xBi*E_y-xEi*B_y-Rotmat[2,3]*xBi*zEi+Rotmat[2,3]*xEi*zBi)/(xBi*yEi-xEi*yBi);
     Rotmat[2,1]:=-(-E_y+Rotmat[2,2]*yEi+Rotmat[2,3]*zEi)/xEi;
     Rotmat[3,3]:=(xSi*yBi*E_z-xBi*ySi*E_z-xSi*yEi*B_z+xEi*ySi*B_z+xBi*yEi*S_z-xEi*yBi*S_z)/
        (xSi*yBi*zEi-xBi*ySi*zEi-xSi*yEi*zBi+xEi*ySi*zBi+xBi*yEi*zSi-xEi*yBi*zSi);
     Rotmat[3,2]:=(xBi*E_z-Rotmat[3,3]*xBi*zEi-xEi*B_z+Rotmat[3,3]*xEi*zBi)/(xBi*yEi-xEi*yBi);
     Rotmat[3,1]:=-(Rotmat[3,2]*yEi-E_z+Rotmat[3,3]*zEi)/xEi;
     Rotmat[1,1]:=Rotmat[2,2]*Rotmat[3,3]-Rotmat[2,3]*Rotmat[3,2];
     ex:=arctan(-Rotmat[3,2]/Rotmat[3,3])*180/PI;
     ey:=arcsin(Rotmat[3,1])*180/PI;
     ez:=arctan(-Rotmat[2,1]/Rotmat[1,1])*180/PI;
end;
165: 9  Geändert  Einfügen
```

Transformation between inertial (J2000) and local coordinate system:

```
beginn | warten | volumen | steps | potkoeffhom | trajectory | FmxUtils
procedure transformation(bb: boolean; ss: integer; rx1,ry1,rz1: extended; var rx2,ry2,rz2: extended);
var Rotmat: array [1..3,1..3] of extended;   {rotational matrix}
begin
     if bb=true then   {transformation from inertial(J2000) to body-fixed}
     begin
          Rotmat[1,1]:=cos(ey*PI/180)*cos((ez+wz*ss)*PI/180);
          Rotmat[1,2]:=sin(ex*PI/180)*sin(ey*PI/180)*cos((ez+wz*ss)*PI/180)+cos(ex*PI/180)*sin((ez+wz*ss)*PI/180);
          Rotmat[1,3]:=-cos(ex*PI/180)*sin(ey*PI/180)*cos((ez+wz*ss)*PI/180)+sin(ex*PI/180)*sin((ez+wz*ss)*PI/180);
          Rotmat[2,1]:=-cos(ey*PI/180)*sin((ez+wz*ss)*PI/180);
          Rotmat[2,2]:=-sin(ex*PI/180)*sin(ey*PI/180)*sin((ez+wz*ss)*PI/180)+cos(ex*PI/180)*cos((ez+wz*ss)*PI/180);
          Rotmat[2,3]:=cos(ex*PI/180)*sin(ey*PI/180)*sin((ez+wz*ss)*PI/180)+sin(ex*PI/180)*cos((ez+wz*ss)*PI/180);
          Rotmat[3,1]:=sin(ey*PI/180);
          Rotmat[3,2]:=-sin(ex*PI/180)*cos(ey*PI/180);
          Rotmat[3,3]:=cos(ex*PI/180)*cos(ey*PI/180);
     end
     else begin   {transformation from body-fixed to inertial(J2000)}
          Rotmat[1,1]:=cos(ey*PI/180)*cos((ez+wz*ss)*PI/180);
          Rotmat[1,2]:=-sin(ez*PI/180)*cos(ey*PI/180);
          Rotmat[1,3]:=sin(ey*PI/180);
          Rotmat[2,1]:=sin(ex*PI/180)*sin(ey*PI/180)*cos((ez+wz*ss)*PI/180)+cos(ex*PI/180)*sin((ez+wz*ss)*PI/180);
          Rotmat[2,2]:=-sin(ex*PI/180)*sin(ey*PI/180)*sin((ez+wz*ss)*PI/180)+cos(ex*PI/180)*cos((ez+wz*ss)*PI/180);
          Rotmat[2,3]:=-cos(ey*PI/180)*sin((ex+wz*ss)*PI/180);
          Rotmat[3,1]:=-cos(ex*PI/180)*sin(ey*PI/180)*cos((ez+wz*ss)*PI/180)+sin(ex*PI/180)*sin((ez+wz*ss)*PI/180);
          Rotmat[3,2]:=cos(ex*PI/180)*sin(ey*PI/180)*sin((ez+wz*ss)*PI/180)+sin(ex*PI/180)*cos((ez+wz*ss)*PI/180);
          Rotmat[3,3]:=cos(ex*PI/180)*cos(ey*PI/180);
     end;
     rx2:=Rotmat[1,1]*rx1+Rotmat[1,2]*ry1+Rotmat[1,3]*rz1;
     ry2:=Rotmat[2,1]*rx1+Rotmat[2,2]*ry1+Rotmat[2,3]*rz1;
     rz2:=Rotmat[3,1]*rx1+Rotmat[3,2]*ry1+Rotmat[3,3]*rz1;
end;
165: 9  Geändert  Einfügen
```

F.3. ACCELERATIONS

spacecraft\trajectory.pas

beginn | trajectory

```
procedure acceleration (ll,pp,rr,xx,yy,zz: extended; var acx,acy,acz: extended);
var n,m: integer;
    PL,dPL: feld;   {Legendre Functions and derivatives}
    sumn,summ: extended;
    dtdr,dtdlam,dtdtheta: extended;   {first derivates of disturbed potential/Störpotential}
    dxB,dyB,dzB: extended;   {local (body fixed) disturbances of disturbing body}
    rscB: extended;   {distance s/c to disturbing body}
begin
     legendre(pp,PL,dPL);   {*B.1.3.1*}
     if gf=false then
     begin
          dtdr:=0;
          dtdlam:=0;
          dtdtheta:=0;
     end
     else begin
     sumn:=0;   {calculating dT/dr [m/s²]}
     for n:=2 to p do
     begin
          summ:=0;
          for m:=0 to p do
          begin
               if m<=n then
               summ:=summ+(JKoeff[n,m]*cos(m*ll*PI/180)+KKoeff[n,m]*sin(m*ll*PI/180))*PL[n,m];
          end;
          sumn:=sumn+(-(n+1)*power(a,n)/power(rr,n+2))*summ;
     end;
     dtdr:=sumn*GM;
     sumn:=0;   {calculating dT/dlam [m²/s²]}
     for n:=2 to p do
     begin
          summ:=0;
          for m:=0 to p do
          begin
               if m<=n then
               summ:=summ+(-JKoeff[n,m]*sin(m*ll*PI/180)+KKoeff[n,m]*cos(m*ll*PI/180))*PL[n,m]*m;
          end;
          sumn:=sumn+power(a,n)/power(rr,n+1)*summ;
     end;
     dtdlam:=sumn*GM;
     sumn:=0;   {calculating dT/dtheta [m²/s²]}
     for n:=2 to p do
     begin
          summ:=0;
          for m:=0 to p do
          begin
               if m<=n then
               summ:=summ+(JKoeff[n,m]*cos(m*ll*PI/180)+KKoeff[n,m]*sin(m*ll*PI/180))*dPL[n,m];
          end;
          sumn:=sumn+power(a,n)/power(rr,n+1)*summ;
     end;
     dtdtheta:=sumn*GM;
     end;
     if FormTrajectory.dist_body.ItemIndex=0 then   {additional disturbing body included}
     begin
          rscB:=sqrt(sqr(xx-B_x)+sqr(yy-B_y)+sqr(zz-B_z));
          dxB:=G*mass/power(rscB,3)*(xx-B_x);   {[m/s²]}
          dyB:=G*mass/power(rscB,3)*(yy-B_y);
          dzB:=G*mass/power(rscB,3)*(zz-B_z);
     end
     else begin
          dxB:=0; dyB:=0; dzB:=0;
     end;

     acx:=xx/rr*dtdr+xx*zz/(sqr(rr)*sqrt(sqr(xx)+sqr(yy)))*dtdtheta-yy/(sqr(xx)+sqr(yy))*dtdlam+dxB;
     acy:=yy/rr*dtdr+yy*zz/(sqr(rr)*sqrt(sqr(xx)+sqr(yy)))*dtdtheta+xx/(sqr(xx)+sqr(yy))*dtdlam+dyB;
     acz:=zz/rr*dtdr-sqrt(sqr(xx)+sqr(yy))/sqr(rr)*dtdtheta+dzB;
end;
```

401: 11 | Einfügen

Bisher erschienen:

Heft1: Kolloquium der Assistenten der Studienrichtung Vermessungswesen. 1970 - 1973, Dezember 1973.

Heft 2: EGGER-PERDICH-PLACH-WAGENSOMMERER, Taschenrechner HP 45 und HP 65, Programme und Anwendungen im Vermessungswesen. 1. Auflage, März 1974, Special Edition in English, Juli 1974, 2. verbesserte Auflage, November 1974.

Heft 3: Kolloquium der Assistenten der Studienrichtung Vermessungswesen 1973 - 1974, September 1974.

Heft 4: EGGER-PALFINGER-PERDICH-PLACH-WAGENSOMMERER, Tektronix-Tischrechner TEK 31, Programmbibliothek für den Einsatz im Vermessungswesen, November 1974.

Heft 5: K.LEDERSTEGER, Die horizontale Isostasie und das isostatische Geoid, Februar 1975.

Heft 6: F.REINHART, Katalog von FK4 Horrebow-Paaren für Breiten von +30 bis +60, Oktober 1975.

Heft 7: Arbeiten aus dem Institut für Höhere Geodäsie, Wien, Dezember 1975.

Heft 8: Veröffentlichungen des Instituts für Photogrammetrie zum XIII. Internationalen Kongreß für Photogrammetrie in Helsinki 1976, Wien, Juli 1976.

Heft 9: W.PILLEWIZER, Felsdarstellung aus Orthophotos, Wien, Juni 1976.

Heft 10: PERDICH-PLACH-WAGENSOMMERER, Der Einsatz des programmierbaren Taschenrechners Texas Instruments SR-52 mit Drucker PC100 in ingenieurgeodätischen Rechentechnik, Wien, Mai 1976.

Heft 11: Kolloquium der Assistenten der Studienrichtung Vermessungswesen 1974 - 1976, November 1976.

Heft 12: Kartographische Vorträge der Geodätischen Informationstage 1976, Wien, Mai 1977.

Heft 13: Veröffentlichung des Instituts für Photogrammetrie anläßlich des 80. Geburtstages von Prof.Dr.h.c.K.Neumaier, Wien, Januar 1978.

Heft 14: L.MOLNAR, Self Checking Analytical Relative Orientation and Strip Formation, Wien, Dezember 1978.

Heft 15: Veröffentlichung des Instituts für Landesvermessung anläßlich des 80. Geburtstages von Prof.Dr.Alois Bavir, Wien, Januar 1979.

Heft 16: Kolloquium der Assistenten der Studienrichtung Vermessungswesen 1976 - 1978, Wien, November 1979.

Heft 17: E.VOZIKIS, Die photographische Differentialumbildung gekrümmter Flächen mit Beispielen aus der Architekturbildmessung, Wien, Dezember 1979.

Heft 18: Veröffentlichung des Instituts für Allgemeine Geodäsie anläßlich des 75. Geburtstages von Prof.Dipl.Ing.Dr.F.Hauer, Die Höhe des Großglockners, Wien, 1981.

Heft 19: H.KAGER, Bündeltriangulation mit indirekt beobachteten Kreiszentren, Wien, April 1981.

Heft 20: Kartrographische Vorträge der Geodätischen Informationstage 1980, Wien, Mai 1982.

Heft 21: Veröffentlichung des Instituts für Kartographie anläßlich des 70. Geburtstages von Prof.Dr.Wolfgang Pillewizer: Glaziologie und Kartographie, Wien, Dezember 1982.

Heft 22: K.TEMPFLI, Genauigkeitsschätzung digitaler Höhenmodelle mittels Spektralanalyse, Wien, Mai 1982.

Heft 23: E.CSAPLOVICS, Interpretation von Farbinfrarotbildern, Wien, November 1982.

Heft 24: J.JANSA, Rektifizierung von Multispektral-Scanneraufnahmen - Entwicklung und Erprobung eines EDV-Programms, Wien, Mai 1983.

Heft 25: Zusammenfassung der Diplomarbeiten, Dissertationen und Habilitationen an den geodätischen Instituten der TU Wien, Wien, November 1984.

Heft 26: T.WUNDERLICH, Die voraussetzungsfreie Bestimmung von Refraktionswinkeln, Wien, August 1985.

Heft 27: G.GERSTBACH (Hrsg.), Geowissenschaftliche/geotechnische Daten in Landinformationssystemen - Bedarf und Möglichkeiten in Österreich, Juni 1986.

Heft 28: K.NOVAK, Orientierung von Amateuraufnahmen ohne Paßpunkte, Wien, August 1986.

Heft 29: Veröffentlichung des Instituts für Landesvermessung und Ingenieurgeodäsie, Abt. Ingenieurgeodäsie, anläßlich des 80. Geburtstages von Prof.Dipl.Ing.Dr.F.Hauer, Wien, Oktober 1986.

Heft 30: K.-H.ROCH, Über die Bedeutung dynamisch ermittelter Parameter für die Bestimmung von Gesteins- und Gebirgseigenschaften, Wien, Februar 1987.

Heft 31: G. HE, Bildverbesserung mittels digitaler Filterung, Wien, April 1989.

Heft 32: F.SCHLÖGELHOFER, Qualitäts- und Wirtschaftlichkeitsmodelle für die Ingenieurphotogrammetrie, Wien, April 1989.

Heft 33: G.GERSTBACH (Hrsg.), Geowissenschaftliche/geotechnische Daten in Landinformationssystemen - Datenbestände und Datenaustausch in Österreich, Wien, Juni 1989.

Heft 34: F.HOCHSTÖGER, Ein Beitrag zur Anwendung und Visualisierung digitaler Geländemodelle, Wien, Dezember 1989.

Heft 35: R.WEBER, Lokale Schwerefeldmodellierung unter Berücksichtigung spektraler Methoden zur Geländereduktion, Wien, April 1990.

Heft 36: o.Prof.Dr.Hans Schmid zum 70. Geburtstag. Veröffentlichung der Abteilung für Landesvermessung, Wien, Oktober 1990.

Heft 37: G.GERSTBACH, H.P.HÖLLRIEGL und R.WEBER, Geowissenschaftliche Informationsbörse - Eine Nachlese zu GeoLIS II, Wien, Oktober 1990.

Heft 38: R.ECKER, Rastergraphische Visualisierungen mittels digitaler Geländemodelle, Wien, August 1991.

Heft 39: Kartographische Forschungen und Anwendungsorientierte Entwicklungen, herausgegeben von W.Stams und F.Kelnhofer zum 80. Geburtstag von Prof.Dr.W.Pillewizer, Wien, Juli 1991.

Heft 39a: W.RIEGER, Hydrologische Anwendungen des digitalen Geländemodelles, Wien, Juli 1992.

Heft 40: K.STEINNOCHER, Methodische Erweiterungen der Landnutzungsklassifikation und Implementierung auf einem Transputernetzwerk, Wien, Juli 1994.

Heft 41: G.FORKERT, Die Lösung photogrammetrischer Orientierungs- und Rekonstruktionsaufgaben mittels allgemeiner kurvenförmiger Elemente, Wien, Juli 1994.

Heft 42: M.SCHÖNER, W.SCHÖNER, Photogrammetrische und glaziologische Untersuchungen am Gàsbre (Ergebnisse der Spitzbergenexpedition 1991), Wien, Mai 1996.

Heft 43: M.ROIC. Erfassung von nicht signalisierten 3D-Strukturen mit Videotheodoliten, Wien, April 1996.

Heft 44: G.RETSCHER, 3D-Gleiserfassung mit einem Multisensorsystem und linearen Filterverfahren, Wien, April 1996.

Heft 45: W.DAXINGER, Astrogravimetrische Geoidbestimmung für Ingenieurprojekte, Wien, Juli 1996.

Heft 46: M.PLONER, CCD-Astrometrie von Objekten des geostationären Ringes, Wien, November 1996.

Heft 47: Zum Gedenken an Karl Killian "Ingenieur" und "Geodät" 1903-1991, Veröffentlichung der Fachgruppe Geowissenschaften, Wien, Februar 1997.

Heft 48: A.SINDHUBER, Ergänzung und Fortführung eines digitalen Landschaftsmodelles mit multispektralen und hochauflösenden Fernerkundungsaufnahmen, Wien, Mai 1998.

Heft 49: W.WAGNER, Soil Moisture Retrieval from ERS Scatterometer Data, Wien, Dezember 1998.

Heft 50: R.WEBER, E.FRAGNER (Editoren),Prof.Bretterbauer, Festschrift zum 70.Geburtstag, Wien, Juli 1999.

Heft 51: Ch.ÖHRENEDER, A Similarity Measure for Global Image Matching Based on The Forward Modeling Principle, Wien, April 1999.

Heft 52: M.LECHTHALER, G.GARTNER, Per Aspera ad Astra, Festschrift für Fritz Kelnhofer zum 60. Geburtstag, Wien, Jänner 2000.

Heft 53: F.KELNHOFER, M.LECHTHALER, Interaktive Karten (Atlanten) und Multimedia – Applikationen, Wien, März 2000.

Heft 54: A.MISCHKE, Entwicklung eines Videotheodlit-Meßsystems zur automatischen Richtungsmessung von nicht signalisierten Objektpunkten, Wien, Mai 2000

Heft 55: Veröffentlichung des I.P.F. anlässlich der Emeritierung von Prof.Dr. Peter Waldhäusl, Wien.

Heft 56: F.ROTTENSTEINER, Semi-automatic Extraction of Buildings Based on Hybrid Adjustment Using 3D Surface Models and Management of Building Data in a TIS, Wien, Juni 2001.

Heft 57: D.LEGENSTEIN, Objektrekonstruktion aus perspektiven Bildern unter Einbeziehung von Umrisslinien, Wien, Mai 2001.

Heft 58: F.KELNHOFER, M.LECHTHALER und K.BRUNNER (Hrsg.), Telekartographie und Location Based Services, Wien, Jänner 2002.

Heft 59: K.BRETTERBAUER, Die runde Erde eben dargestellt: Abbildungslehre und sphärische Kartennetzentwürfe, Wien, 2002.

Heft 60: G.GARTNER, Maps and the Internet 2002, Wien 2002.

Heft 61: L.DORFFNER, Erzeugung von qualitativ hochwertigen 3D Photomodellen für Internetbasierte Anwendungen mit besonderem Augenmerk auf Objekte der Nahbereichsphotogrammetrie, Wien, Jänner 2002.

Heft 62: CHMELINA, Wissensbasierte Analyse von Verschiebungsdaten im Tunnelbau Wien 2002

Heft 63: A.NIESSNER, Qualitative Deformationsanalase unter Ausnutzung der Farbinformation, Wien 2002

Heft 64: K.BRETTERBAUER; R.WEBER, A Primer of Geodesy for GIS-Users, Wien im Herbst 2003

Heft 65: N.PFEIFER, 3D Terain Models on the basis of a triangulation, Wien, Jänner 2002.

Heft 66: G.GARTNER (Hrsg), Lacation Based Services & Telecartography, Wien, 2004.

Heft 67: I.KABASHI, Gleichzeitig-gegenseitige Zenitwinkelmessung über größere Entfernungen mit automatischen Zielsystemen, Wien, 2004.

Heft 68: J. BÖHM, Troposphärische Laufzeitverzögerungen in der VLBI, Wien, 2004.

Heft 69: Evolving Space Geodesy Techniques, Proceedings EGS 2002 Geodesy Session 9, Wien, 2004.